Restoration and universal operation of grid-forming inverters

by

Fahmid Sadeque

B.Sc., Bangladesh University of Engineering and Technology, 2014

M.Sc., Bangladesh University of Engineering and Technology, 2017

AN ABSTRACT OF A DISSERTATION

submitted in partial fulfillment of the
requirements for the degree

DOCTOR OF PHILOSOPHY

Mike Weigers Department of Electrical and Computer Engineering
Carl R. Ice College of Engineering

KANSAS STATE UNIVERSITY
Manhattan, Kansas

2022

Abstract

This dissertation presents novel control methods for frequency and voltage restoration, and universal operation of grid-forming (GFM) inverters. The developed controllers solve the technical challenges for a microgrid with multiple GFM inverters in synchronization and power-sharing, phase-angle detection under asymmetrical conditions, capability to operate in the grid-following (GFL) mode, and frequency and voltage restoration. First, two synchronization methods for GFM inverters are presented. In the output-sync method, an incoming GFM inverter synchronizes its output voltage parameters, i.e., amplitude, phase angle, and frequency, at its point of common coupling (PCC) before closing the circuit breaker. The task is uniquely performed by introducing two proportional-integral (PI) controllers that adjust the output voltage and the angular frequency of the inverter. In the controller-sync method, two sets of controller paths are run in parallel and kept synchronized to produce the same PWM reference. But, only one set of the controller is engaged at a time. The uniqueness of this method is that it allows an inverter to stay connected to the microgrid in a standby mode without injecting any power. Then, when enabled, the inverter gradually shifts to decentralized power-sharing mode without switching the controller. Finally, the controller seamlessly switches to GFM mode, where the inverters are completely independent but synchronized. Another noteworthy fact is that, unlike the output-sync method that used two sets of voltage measurements, the controller sync method only uses one set of voltage measurements. A state-space model of the GFM inverter with the controller-sync method is derived to show the stability at every mode. The efficacy of the developed methods is experimentally validated in a microgrid with both droop and virtual inertia for power-sharing. A new phase-angle detection method, called signal reformation-based direct phase-angle detection (DPD-SR), is developed that provides an enhanced phase-angle detection capability for the GFM inverter under asymmetrical conditions of the system. The developed DPD-SR can directly estimate

the phase-angle by using a mathematical function. The unique signal-reformation technique used in this method can process the asymmetrical voltage measurements into a symmetrical form and extract the phase-angle of the system without using any complicated closed-loop control. The DPD-SR method is verified through hardware experiments and compared with state-of-the-art method. Eventually, a universal controller is developed that combines the feature of the controller-sync and the DPD-SR methods. Furthermore, the developed universal controller enables an inverter to operate in GFL and GFM mode is developed. With the universal controller, the inverter can inject desired active and reactive power to the grid or microgrid in GFL mode and seamlessly transit to GFM mode if islanding is detected. The universal controller has two sets of parallel paths, where one path provide GFM control and the other path provides the GFL control and synchronization. A frequency-based islanding detection is added to the developed controller. The uniqueness of the universal controller is, the two paths are always synchronized and can provide seamless GFL to GFM transition when a fault occurs. The controller's stability is analyzed through a state-space model, and the performance of the developed controller is verified in a microgrid for grid-connected and islanded operation in this dissertation. Finally, a frequency and voltage restoration controller is developed to overcome the frequency and voltage deviation problem with the droop controller for power-sharing. In droop-controlled power-sharing, the frequency and voltage are required to deviate from their nominal values. On the contrary, the frequency and voltage of the system are expected to be regulated by the GFM inverters. This dissertation develops a threshold-based frequency and voltage restoration method for the GFM inverters without compromising the effectiveness of the decentralized power-sharing methods. The novelty of this method is that the restoration control paths are only enabled when a load change or plug-in of an inverter is identified and disabled when the frequency and voltage parameters are restored. A state-space model is developed to perform stability analysis. The developed method is compared with a timer-based method to demonstrate its superiority. The efficacy of the restoration method is verified through experiments.

Restoration and universal operation of grid-forming inverters

by

Fahmid Sadeque

B.Sc., Bangladesh University of Engineering and Technology, 2014

M.Sc., Bangladesh University of Engineering and Technology, 2017

A DISSERTATION

submitted in partial fulfillment of the
requirements for the degree

DOCTOR OF PHILOSOPHY

Mike Weigers Department of Electrical and Computer Engineering
Carl R. Ice College of Engineering

KANSAS STATE UNIVERSITY
Manhattan, Kansas

2022

Approved by:

Major Professor
Professor Behrooz Mirafzal

Copyright

Abstract

This dissertation presents novel control methods for frequency and voltage restoration, and universal operation of grid-forming (GFM) inverters. The developed controllers solve the technical challenges for a microgrid with multiple GFM inverters in synchronization and power-sharing, phase-angle detection under asymmetrical conditions, capability to operate in the grid-following (GFL) mode, and frequency and voltage restoration. First, two synchronization methods for GFM inverters are presented. In the output-sync method, an incoming GFM inverter synchronizes its output voltage parameters, i.e., amplitude, phase angle, and frequency, at its point of common coupling (PCC) before closing the circuit breaker. The task is uniquely performed by introducing two proportional-integral (PI) controllers that adjust the output voltage and the angular frequency of the inverter. In the controller-sync method, two sets of controller paths are run in parallel and kept synchronized to produce the same PWM reference. But, only one set of the controller is engaged at a time. The uniqueness of this method is that it allows an inverter to stay connected to the microgrid in a standby mode without injecting any power. Then, when enabled, the inverter gradually shifts to decentralized power-sharing mode without switching the controller. Finally, the controller seamlessly switches to GFM mode, where the inverters are completely independent but synchronized. Another noteworthy fact is that, unlike the output-sync method that used two sets of voltage measurements, the controller sync method only uses one set of voltage measurements. A state-space model of the GFM inverter with the controller-sync method is derived to show the stability at every mode. The efficacy of the developed methods is experimentally validated in a microgrid with both droop and virtual inertia for power-sharing. A new phase-angle detection method, called signal reformation-based direct phase-angle detection (DPD-SR), is developed that provides an enhanced phase-angle detection capability for the GFM inverter under asymmetrical conditions of the system. The developed DPD-SR can directly estimate

the phase-angle by using a mathematical function. The unique signal-reformation technique used in this method can process the asymmetrical voltage measurements into a symmetrical form and extract the phase-angle of the system without using any complicated closed-loop control. The DPD-SR method is verified through hardware experiments and compared with state-of-the-art method. Eventually, a universal controller is developed that combines the feature of the controller-sync and the DPD-SR methods. Furthermore, the developed universal controller enables an inverter to operate in GFL and GFM mode is developed. With the universal controller, the inverter can inject desired active and reactive power to the grid or microgrid in GFL mode and seamlessly transit to GFM mode if islanding is detected. The universal controller has two sets of parallel paths, where one path provide GFM control and the other path provides the GFL control and synchronization. A frequency-based islanding detection is added to the developed controller. The uniqueness of the universal controller is, the two paths are always synchronized and can provide seamless GFL to GFM transition when a fault occurs. The controller's stability is analyzed through a state-space model, and the performance of the developed controller is verified in a microgrid for grid-connected and islanded operation in this dissertation. Finally, a frequency and voltage restoration controller is developed to overcome the frequency and voltage deviation problem with the droop controller for power-sharing. In droop-controlled power-sharing, the frequency and voltage are required to deviate from their nominal values. On the contrary, the frequency and voltage of the system are expected to be regulated by the GFM inverters. This dissertation develops a threshold-based frequency and voltage restoration method for the GFM inverters without compromising the effectiveness of the decentralized power-sharing methods. The novelty of this method is that the restoration control paths are only enabled when a load change or plug-in of an inverter is identified and disabled when the frequency and voltage parameters are restored. A state-space model is developed to perform stability analysis. The developed method is compared with a timer-based method to demonstrate its superiority. The efficacy of the restoration method is verified through experiments.

Table of Contents

List of Figures

List of Tables

Acknowledgments

This dissertation is a compilation of my four years of challenging endeavor. The accomplishment of this tremendous task would not have been possible without the support of my near and dear ones. First, I want to express my gratitude towards the Almighty Creator, without whose divine guidance I would not have been able to succeed. I am thankful to my dear wife, parents, and sister, who have unconditionally supported me and prayed for my well-being.

I sincerely thank my advisor Prof. Behrooz Mirafzal for his valuable guidance and technical advice throughout this dissertation's progress. I firmly believe his rich knowledge and proper guidance have shaped me into a better researcher and an engineer.

I am grateful to my Ph.D. supervisory committee members Dr. Fariba Fateh, Dr. Anil Pahwa, Dr. Hongyu Wu, and Dr. Arslan Munir, for their insightful suggestions during my preliminary examination, which have helped me a lot in developing this dissertation.

I thank my highly knowledgeable ex-lab mates of the Smart Power Electronics and Control Systems (SPECS) Research Group, Dr. Aswad Adib, Dr. Joseph Benzaquen, and Dr. Mohsen Pilehvar, who have helped me in every aspect of my research and course work, and shared their knowledge and handful experiences with the laboratory work. I am thankful to Dr. Dushyant Sharma, who guided me throughout the controller and hardware development for the microgrid testbed. My heartfelt thanks to my current lab mates, Mr. Tareq Hossen and Mr. Mehmetcan Gursoy. Their support and positive attitude have made this research lab an enjoyable place.

Dedication

To my family.

Chapter 1

Introduction

The primary objective of this dissertation is to solve the technical challenges for the GFM inverters in a multi-inverter system for restoration and universal operation by developing new control methods. The motivation and objectives of this dissertation are outlined in Section 1.1. The state-of-the-art GFM controls for decentralized power-sharing and synchronization, inverter control under asymmetrical conditions, and voltage and frequency restoration methods are discussed, and the possible scopes for improvements are identified in Section 1.2. The contribution of this dissertation in developing new control methods to address the shortcomings of the state-of-the-art methods discussed in Section 1.2 are presented in Section 1.3. Finally, the organization of this dissertation is outlined in Section 1.4.

1.1 Motivation and Objectives

The future power grid is expected to be penetrated by many inverters, as the existing electric power generation technology needs to gradually shift from the traditional fossil fuel-based resources to environment-friendly renewable energy-based resources, e.g., solar, wind, and hydro energy. Nowadays, renewable energy is harnessed in the form of distributed generation (DG), where the inverters are used as the interface between the intermittent energy sources and the power grid [1–6]. The inverters in a power grid, also known as grid-interactive

inverters, can either be operated as grid-following (GFL) inverters, where the inverters only inject the active and reactive power commanded by the utility operator [7, 8], or operate as grid-forming (GFM) inverters, where the inverters control the output voltage and the frequency [9–11].

The GFL inverters are dependent on the system voltage and frequency and hence, cannot operate alone. Typically, the GFL inverters are combined with the maximum power-tracking control in DG to inject as much active power into the grid as available in grid-feeding mode [1]. Besides, the GFL inverter can also provide different ancillary services, e.g., voltage and frequency fluctuation mitigation [12], maximum DC-bus utilization [13–15], stability enhancement [16–18] etc., by injecting some reactive power in grid-supporting mode. Typically, 30% of the available active power is curtailed from the generation and reserved for the ancillary services [19]. On the other hand, the inverters in GFM mode are independent and can provide their voltage amplitude and frequency references. However, GFM inverters do not have any control over active and reactive power injection. It is expected that the GFM inverters will be extensively used in future power grids [20]. A microgrid can reinstate its operation using the black-start capability of the grid-forming inverter and perhaps will even be able to contribute to the restoration of the utility grid [21]. Also, in the future, the GFM inverters may have to undertake some roles of the present GFL inverters, e.g., providing ancillary services. Therefore, the capacity of the GFM inverters needs to be sufficiently large to be the primary source of power for a microgrid, as they must mitigate the total power demands [22]. This can be feasible in GFM plants with large capacities, e.g., PV plants with MW range of generation capacity and sufficient battery energy storage systems.

Despite having so many advantages of including the GFM inverters in the power grid, there are pressing concerns yet to be resolved. Firstly, to prevent overloading of the GFM inverters, proportional power sharing based on the inverters' capacity is needed [23]. Decentralized power-sharing methods are perhaps the best approach, as centralized methods have the risk of cyberattacks and communication delays, and the cost for a secured central control will be expensive [24]. On the other hand, decentralized power-sharing requires the frequency and voltage to deviate from their nominal values, which may result in tripping

the inverters if the frequency or the voltage fall below the permissible limit [25]. Therefore, the GFM inverters must be able to restore the voltage and frequency under any loading condition [26]. Also, as multiple GFM inverters will be operated independently and each inverter will provide its voltage and frequency references, the output voltages of the inverters may fall out of synchronization and trip. Therefore, a proper synchronization method is required to maintain the coherency between the inverters [27], particularly when an inverter (re)connects to a power grid. Also, asymmetries in microgrids may happen because of the unbalanced loads in the three phases and random penetration of distributed generation (DG) units. Phase-angle detection for synchronization of inverters can be erroneous under the unbalanced microgrid conditions [28]. Also, should a fault occur in the power grid, the inverters should be able to seamlessly switch from GFL mode to GFM mode [29]. Under these circumstances, an inverter controller that universally works in GFL and GFM mode will be beneficial. This dissertation focuses on the technical challenges in synchronization, power-sharing, phase-angle detection under asymmetrical conditions, and voltage and frequency restorations for restoration, and the universal operation of GFM inverters. It discusses the state-of-the-art solutions and their drawbacks and develops and validates the efficacy of the new control methods.

The following subsections briefly describe the most basic control methods for the inverters in GFL and GFM modes.

1.1.1 Control Methods for GFL Inverters

In this subsection, some important control methods for the GFL inverters are briefly presented for the continuation of the discussion on the role of inverters in power-grid. At present, the majority of the inverters operate in GFL mode, where the amplitude, frequency and phase-angle of the output voltage of the inverters are synchronized with the power grid's voltage at the at the point of common coupling (PCC). The GFL controller uses a phase-locked loop is used to estimate the phase-angle of the voltages at the PCC for the synchronization [30].

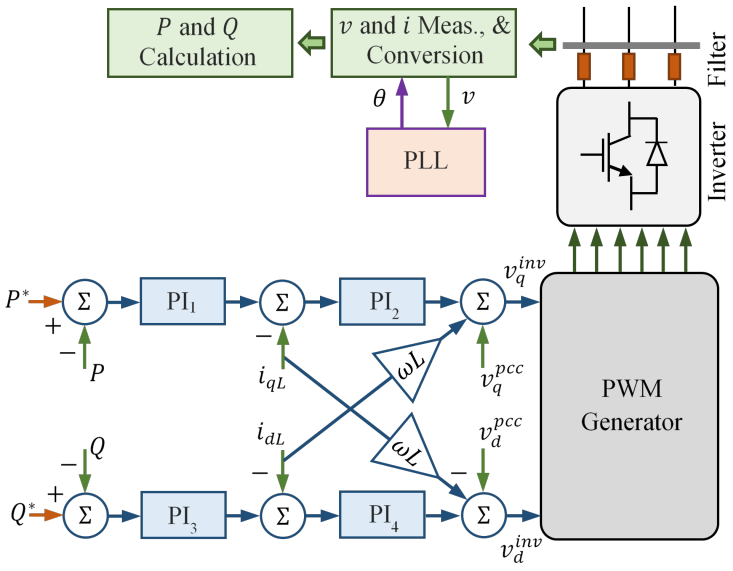

Figure 1.1: *A typical inverter controller for GFL mode.*

Fig. 1.1 shows a typical GFL inverter controller [31]. The controller is operated in a synchronously rotating dq frame of reference. By separating the control into dq frame of reference, the active and the reactive power control are made independent. Notice that each control path comprises of two cascaded loops. The active power P, and the reactive power Q is controlled to their corresponding desired active P^*, and reactive power Q^* with the power control loops, i.e. the outer loops and the current control loops, i.e. the inner loops. The line-line voltages at the PCC of the inverter and the line currents are measured and decomposed into dq frame of reference. This cascaded loop structure provides improved dynamic control in comparison to the single loop structures [27]. Notice that each loop consists of one proportional-integral controller whole proportional and integral gain parameters are tuned. The final output of the control paths, v_q^{inv} and v_d^{inv} are then converted from the dq to the abc frame of references for the PWM generator of the GFL inverter.

The basic GFL controller can be configured to provide different ancillary services. An atypical PWM control is presented in [13] where the GFL is able to compensate for the fluctuation in the DC-bus. The GFL controller in [32] and in [33] are presented to provide reactive power support to mitigate the symmetrical and asymmetrical voltage sags. Active power curtailment is needed for these methods. In [34], and [35], two negative-sequence

compensation methods are proposed for providing the ancillary services during anomalies in the grid. A fast voltage disturbance mitigation technique is presented in [36]. An adaptive piece-wise droop is proposed in [37] to mitigate the fluctuations in the frequency. The authors in [31] and [38] introduced the virtual inductance to enhance the stability in the weak grid conditions.

1.1.2 Control Methods for GFM Inverters

In this subsection, two basic GFM inverter controllers are briefly presented for the continuity of the discussion [1, 39]. Unlike the GFL mode, where the inverter behaves like a current source, the inverter in GFM mode behaves like a voltage source whose voltage amplitude and frequency can be controlled. Hence, although current regulating paths are typically used for advanced GFM controls, the basic GFM controller can only be developed with voltage control loops [40–42].

Fig. 1.2 shows the structure of two GFM controllers, developed based on the discussion in the previous paragraph. A phase-angle reference, θ, is given to the PWM generator block. A nominal frequency reference, ω_n is provided, which is integrated to obtain the phase-angle reference. The controllers in Fig. 1.2 also have droop controls to facilitate decentralized power sharing. Therefore, the actual frequency reference becomes, $\omega^* = \omega_n - \Delta\omega$. Here, $\Delta\omega$ is obtained from the droop as shown in Fig. 1.2, or can be obtained from any other decentralized power-sharing controls, e.g., virtual inertia. For single GFM operation, $\Delta\omega$ can be 0. The PWM generator also required a controlled voltage reference. To do so, a nominal voltage reference is provided and compared with the output voltage of the inverter. The voltage reference for the PWM generator can be provided in two ways as shown in Figs. 1.2(a) and 1.2(b). In the method shown in Fig. 1.2(a), the amplitude of the output voltage V is controlled to a desired value, $V^* = V_n - \Delta V$. Here, V_n is the given nominal voltage amplitude and ΔV is the change in voltage due to droop. The proportional-integral block PI_V minimizes the error between the amplitude of the inverter output voltage V_{pcc} and the reference voltage V^*. In the method in Fig. 1.2(b), the dq-components of the voltage

are provided to the PWM generator block. Typically, the q-axis component is controlled to the desired voltage reference, $v_q^* = V_n - \Delta V$ and the d-axis component is controlled to 0. Two proportional-integral blocks, PI_{Vq} and PI_{Vd} separately performs the control. The PWM block converts the dq components to the abc components. Also, abc to dq conversion is required for the voltage measurements. It is also possible to develop a controller similar to the

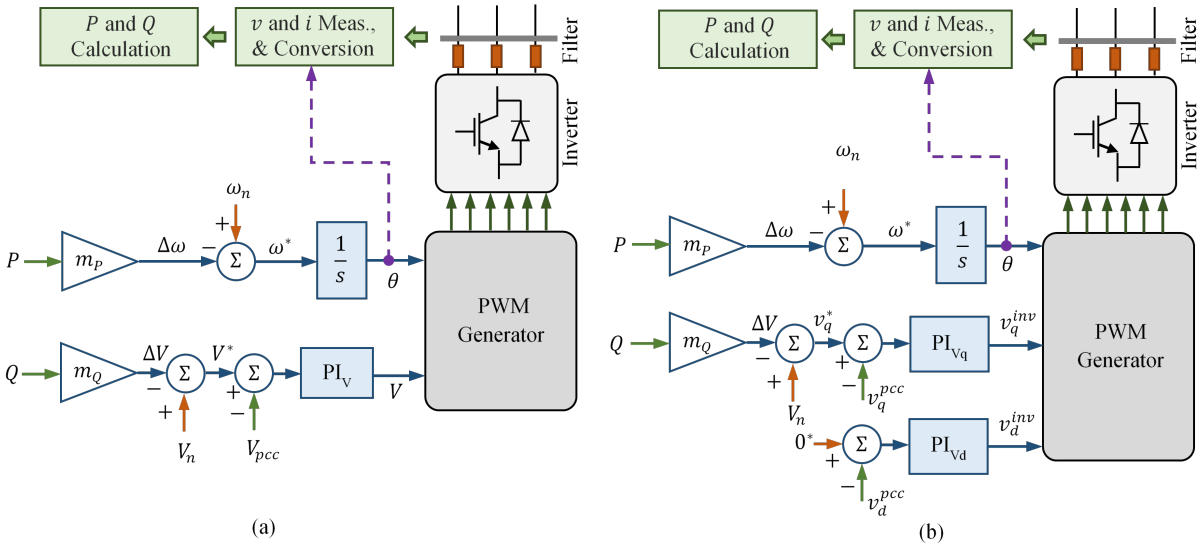

Figure 1.2: *Two most common GFM inverter controllers with droop. (a) Voltage control in abc frame of reference, and (b) voltage control in dq frame of reference.*

one in Fig. 1.2(b), where the q-axis component is regulated to 0 and the d-axis component is regulated to the desired value [19, 43]. Notice that the control method presented in Fig. 1.2(a) provides a simpler control approach with just one PI block, whereas, the method in Fig. 1.2(b) provides decoupled control over the dq axis component with two PI blocks and abc to dq and vice-versa transformation. Nevertheless, both the controllers can produce the exact same output voltage from an inverter. The controllers shown in Figs. 1.2(a) and 1.2(b) can be modified by replacing the droop with the virtual inertia [1]. Fig. 1.3 shows a GFM controller with virtual inertia that replaces the droop in Figs. 1.2(a). Notice that in virtual inertia, the active power-frequency relationship is defined by the swing equation $J\omega_m(d\omega^*/dt) + (DS_b/\omega_n)(\omega^* - \omega_n) + P = 0$, where J, D, and S_b are the virtual inertia, damping factor, and the power rating of the inverter, respectively. A brief discussion on

the virtual inertia is provided in the subsection 1.2.2 of Section 1.2. An advanced GFM controller may also have current control loops to protect the inverter from being overloaded and a PLL for phase-angle estimation for power measurements and synchronization purposes [44]. All GFM controllers developed in this dissertation are built upon the basic structure of the controller in Fig. 1.2(a). A few experiments are also conducted on the developed controller by replacing the droop controller with the virtual inertia shown in Fig. 1.3.

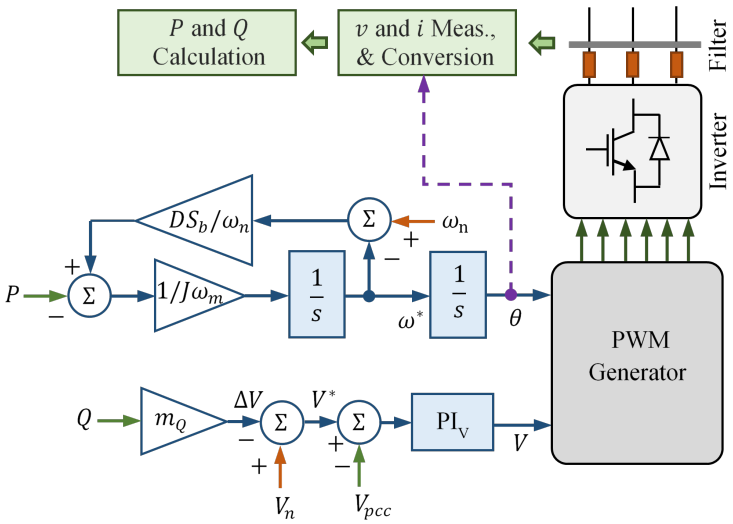

Figure 1.3: *GFM controller using virtual inertia instead of droop.*

1.2 Literature Review

In this section, the state-of-the-art techniques for power-sharing and synchronization, phase-angle detection under asymmetrical conditions, and voltage and frequency restoration are discussed.

1.2.1 State-of-the-art in Synchronization in GFM Mode

An inverter needs to synchronize with the power grid before it is connected to the system. Specifically, proper synchronization is crucial in a multi-GFM inverter system, since each GFM inverter produces independent voltage and frequency references. Several supervisory

control-based synchronization methods are available for the GFM inverters [45–47], where the inverters receive synchronization signals through communication network. A low-bandwidth ethernet communication channel isolated from the supervisory control is suggested in [48], where only the phase-angle references are sent to the inverters. A radio communication-based method is suggested in [49], where FM modulated signals are used to adjust the phase-angle between the inverters for synchronization. However, all these methods have the risk of communication disruptions. On the contrary, very few works are available on decentralized, i.e., communication-less, synchronization of inverters in GFM mode. In decentralized control, the system frequency and voltage are allowed to deviate from their nominal values to accommodate power-sharing, whereas the parameters remain unknown to an incoming GFM inverter. Therefore, most often the inverter is connected to the power grid in GFL mode, where the phase-locked loop (PLL) performs the phase-angle estimation for the synchronization [50]. In [51], a PLL-less self-synchronized synchronverters is proposed, where the inverter is able to adjust its phase-angle prior to synchronization and gradually matches the frequency with the system like a synchronous machine. There are several synchronization methods, where the inverter changes its mode from GFL to GFM after the synchronization [29, 52–61]. However, most of these techniques consider that the inverters operating in parallel are connected to a common bus. Therefore, the tie line impedance between the inverters is zero.

Seamless transition between GFL to GFM mode is also a prerequisite for GFM inverter synchronization methods. In [52] and [53], techniques combining the current controller and the voltage controller are proposed, where only one controller is activated at a time. To provide seamless switching between the controllers, [29] proposed an intermediate mode, named coast mode, between the GFL and GFM modes. In [55] and [58], two unified control methods for GFL and GFM modes are discussed, where the current control and the voltage control are combined as a single control path to provide a PWM reference signal. The authors proposed some mathematical model-based unified controllers in [59] and [60]. A model predictive-based inverter controller is discussed in [59], where an inverter can perform autotuning to adjust the weight factors for the controllers of the two modes of operation. The model-predictive methods require a reference model, which might be challenging to

derive for microgrids operating in GFL and GFM modes. A hierarchical control structure-based generalized control algorithm is proposed in [60], where the unified controller has been developed by designing a multiloop controller. Nevertheless, the controllers suffer from slow transient performance due to their nested loop strategies.

A common GFL and GFM controller with the synchronization capability, that allows an inverter to seamlessly connect to the power grid or microgrid, irrespective of its mode of operation, is not present in the literature.

1.2.2 State-of-the-art in Decentralized Power-Sharing

The GFM inverters in a microgrid must share the total load in proportion to their capacities to prevent overloading of the inverters. Power-sharing can be governed through supervisory control where the inverters receive the command from a central unit through communication channels. However, the supervisory control method is less reliable as it may suffer from malicious cyberattacks and communication delays [40, 62–66]. Therefore, decentralized power-sharing methods receive more attention. State-of-the-art decentralized power-sharing methods can be grouped into three major categories, i.e., droop control, virtual inertia, and virtual oscillator [67–70]. The following paragraphs will briefly present some latest works in each category.

Droop control is a very well known communication-less power-sharing method [71–73]. Instead of using communication signals, this method uses voltage and frequency measurements to determine the system's active and reactive power injection requirement. Specifically, the system's frequency is considered a global parameter for active or reactive power sharing in droop control methods. Droop control in GFM inverter originated from the droop used in conventional power generators. Traditionally, frequency-active power droop, $(P-f)$, is used for GFM inverters, where frequency and the active power are linearly related. Similarly, the inverter output voltage and the reactive power injected by the inverter can be linearly related by the voltage-reactive power droop, $(Q-V)$. However, the conventional $(P-f)$ and $(Q-V)$ droops are originally developed for inductive networks, where the R/X ratio of the system

has comparatively lower values. The authors in [74] and [75] proposed voltage-active power, $(P-V)$, and frequency-reactive power, $(Q-f)$, droops for high R/X ratio, i.e., for resistive networks. To effectively use the $(P-f)$ and $(Q-V)$ droops in resistive networks, R/X ratio can be reduced by virtually increasing the effective inductance of the system [76, 77]. An angle-active power droop, $(P-\theta)$, is presented in [78] and [79], to provide more transient stability for the GFM inverters under voltage dips. In this type of droop, the active power is controlled by adjusting the phase-angle of the inverters. The angle reference required by the inverter is obtained from a global positioning system.

Virtual inertia-based power-sharing methods are developed by mimicking the inertia of a synchronous machine into the characteristics of the inertia-less inverter [68, 80]. Notably, the virtual inertia can be viewed as droop control with a low pass filter [81]. Adding inertia to the GFM inverters provides more dynamic stability during transients. Particularly, during the rapid load changes and disturbances, droop-based control may cause the over and under-frequency relays to trip. Virtual inertia not only slows down the transients but also provides damping to the frequency oscillations during such incidents. To be able to provide virtual inertia by the GFM inverters, a well-managed battery energy storage system is required [82, 83]. The authors in [42] present an analysis of the dynamic characteristics of the virtual inertia, where the closed-loop control for the GFMs is modeled for small-signal and electromagnetic transient analysis. The study shows that when a step response is provided, the rate of change of frequency is lower in the droop control methods. However, virtual inertia-based control requires tuning between the inertia constant and the damping coefficient to ensure the desired response. The authors in [84] and [85] propose two rule-based methods, where the coefficients are selected based on some preset conditions. An adaptive virtual inertia control is proposed in [86] where a controller for tuning the inertia constant ensures enhanced stability of the system after a fault. The adaptive self-tuning methods in [87] and [88] can simultaneously tune both the coefficients while minimizing the frequency deviation through online optimization algorithms.

The virtual oscillator control is developed to mimic the dynamics of a weakly nonlinear oscillator [69, 89]. In the virtual oscillator-based control methods, multiple GFM invert-

ers can operate synchronously without using any PLL or communication signals [90]. In this method, the nonlinear oscillator is modeled in combinations of the virtual resistors, inductors, capacitors, and a voltage-controlled current source. The controller includes scaled representations of the inverter current and the filter capacitor used for the oscillator's control parameters. Nevertheless, the design of the virtual oscillator controller is an iterative process in which multiple open-circuit and full load tests are performed until the sufficient condition for synchronization is met. A systematic design process is presented in [91] that eliminates the iterative process. The oscillator's parameters are tuned with the performance requirements in this method. The authors in [92] proposed a hierarchical control structure for virtual oscillator-based inverter operation and seamless transition between GFM and GFL modes. The controller proposed in [93] can provide universal control for both modes of operation.

1.2.3 Advancements in Phase-Angle Detection

An inverter may have to operate in asymmetrical conditions, e.g., unequal amplitude and phase-angle differences between the three phases. However, the conventional PLL used for phase-angle detection for synchronization and power measurement cannot perform accurately under asymmetrical conditions [94–101]. This is because most conventional PLLs, e.g., synchronous reference frame (SRF) PLL, are originally developed for the stiff grid, which is assumed to be balanced systems with an almost constant frequency. In contrast, the microgrids can often become asymmetrical due to unbalanced loading [99]. Therefore, accurate phase-angle detection under asymmetrical voltage and phase-angle conditions becomes a crucial factor in assuring stability and power quality [77]. Digital filters can be added to the conventional PLLs [57, 102–104] for enhanced operation under noises and disturbances. Delayed signal cancellation (DSC) PLLs are developed to compensate for the negative sequence components of an asymmetrical grid, and harmonics [30, 105]. Though, careful tuning of the filter is needed for these methods so that the filters do not add excessive delays in the controller. Enhance three-phase PLLs (EPLL) are developed to provide

adaptive filtering [16]. However, EPLLs need to be tuned for the operating frequency and therefore, if the frequency varies, e.g., during decentralized power-sharing, the performance of the EPLL may deteriorate [106]. Three separate single-phase PLLs, e.g., second-order generalized integrator-based (SOGI) PLL, can be used for distorted grids [107]. Notice that the three PLLs need to be synchronized through external communication. In [108], and [109], two advanced SRF-PLLs, called double-SRF (DSRF) and decoupled double-SRF (DDSRF) PLLs are proposed, where one positive sequence and one negative sequence SRF blocks are combined for enhanced performance under asymmetrical conditions. Furthermore, the output signals of the SRF blocks are well filtered to eliminate the effects of harmonics. Unlike the closed-loop PLLs, the authors in [29], and [110] developed some open-loop phase-angle detection methods, known as the instantaneous phase detector, which are mathematical models and can operate under any frequencies without requiring any tuning, but only under balanced grid conditions.

To this extent, it is evident that an enhanced but simple phase-angle detection method to operate under asymmetrical conditions will be helpful for the GFM inverters.

1.2.4 State-of-the-art Techniques for Restoration

The microgrid frequency and voltages at the PCCs of the GFM inverters may deviate from their nominal values to allow decentralized power-sharing control [111]. However, allowing the voltage and frequency parameter to vary with load may result in tripping the inverters [25].

Advanced decentralized controls with voltage and frequency restoration techniques are available to overcome the situation. Different forward and feedback control paths are utilized to restore the parameters [44, 112–117]. Notice that the restoration control paths must not be enabled all the time with the decentralized power-sharing controller to ensure proper power-sharing. This is because if the restoration paths are always enabled, then a new inverter will not be able to plug-in into the system in GFM mode and contribute to power-sharing, as the inverter will see no change in the frequency and the voltage. Therefore,

the restoration paths need to be disabled and enabled based on the requirement, i.e., load changes and plug-in of new inverters. In [113], the enable and disable operation is controlled through a low-bandwidth communication, where the GFM inverters receive a one-way signal from the supervisory control when the restoration is needed. In [44], and [114], two methods are proposed to minimize the number of communication channels and the measurement sensors using state estimation-based supervisory control. Nevertheless, this approach is susceptible to delays and cyber-attacks [114]. Also, GFM inverters with decentralized control methods with minimum communication requirement is a cost-effective and more attractive solution for a system with limited communication infrastructure. The restoration paths can be enabled and disabled using timer/counter-based methods, where a timer is set to activate the restoration operation when a load change is identified [115]. However, the timer-based method may become erroneous if the preset restoration time is not sufficient or the load is rapidly changed, e.g., pulse-load. Washout filter-based restoration methods are proposed in [116] and [117], where a low-pass filter structure is adjusted adaptively in response to the load variation. However, these washout filter-based methods will not be able to establish power-sharing when a new inverter synchronizes in GFM mode while the frequency and the voltage are already restored to their nominal values.

Notice that the restoration methods discussed so far do not allow an inverter to plug-in GFM mode and share power. Therefore, a new control approach is needed for the GFM inverters.

1.3 Contribution of the Dissertation

In this section, the contributions of this dissertation in developing the restoration and universal operation for the GFM inverters in a multi-inverter system are outlined.

To enable a GFM inverter to operate in a multi-inverter system two GFM inverter synchronization methods, named output-sync and controller-sync, are presented in this dissertation. The concept of the inverter synchronization has primarily been utilized in synchronization of GFL inverters to the stiff grid [50, 68]. However, synchronization methods for the

GFM inverters are very limited and have scoped for development. The developed output-sync method utilizes two sets of sensor to first match the output voltage amplitude and phase-angle of the incoming inverter with that of the power grid, and then closes the circuit breaker while the phase-angle difference between voltages at the both ends of the circuit breaker are minimum. Power-sharing is established when the circuits breaker is closed. In the controller-sync method, only one set of sensor is needed at the grid-side of the circuit breaker. This method has two sets of controllers paths, whose phase-angle and the voltage amplitude are synchronized, while only one set of path is engaged at a time. The controller ensures that no power is injected from the inverter when the circuit breaker is closed. Power-sharing is gradually established and then the control paths seamlessly switches from one state to another. Both methods can provide seamless transition for the incoming inverter and ensure decentralized power-sharing in proportion to the inverters' capacities. Therefore, undesirable transients and communication related anomalies, e.g., delay, cyberattack, etc., are avoided. The developed synchronization method can be combined with GFMs any decentralized power-sharing method, e.g., droop, virtual-inertia etc. To analyze the stability boundary of the developed controller, a closed-loop state-space model of a GFM inverter is derived and tested under different scenarios. The controller-sync method is further improved to develop a universal control method for that has both the GFL and GFM inverter capability. Although, inverters are being operated in GFL and GFM mode with two different control paths [29, 52, 53], seamless transition between this two modes is a technical challenge. The developed universal controller also has two pairs of parallel control paths. One pair provides the voltage amplitude and phase-angle references for the GFM operation, and the other is for the GFL operation. However, the novelty of the developed controller is that the two pairs are always kept synchronized so that the grid-interactive inverter can seamlessly switch between the GFL and GFM modes.

A direct phase-angle detection technique for the inverter is developed to provide a more enhanced phase-angle detection capability to the inverter under asymmetrical grid conditions and used in all the inverter controllers in this dissertation. Phase-angle of a three-phase system can be obtained directly by using the basic trigonometric formula [29, 110] instead

of the complicated PLL structure. However, state-of-the-art phase-angle detection methods and conventional PLLs cannot perform accurate phase-angle estimation under unbalanced voltage and unequal phase-angle conditions. The direct method developed in this dissertation is based on a novel signal reformation algorithm that can perform accurate phase-angle detection under asymmetrical conditions. The uniqueness of this method is that a three-phase asymmetrical signal can be reformed as a three-phase symmetrical signal without losing the actual phase-angle information. Furthermore, the developed method does not require a closed-loop PI controller and can perform equally at any frequency while reducing the computational burden and delay associated with the complex structures of advanced state-of-the-art methods [108, 109].

The controller-sync method is further improved to develop a universal control method with both GFL and GFM inverter capability. Although inverters are being operated in GFL and GFM mode with two different control paths [29, 52, 53], seamless transition between these two modes is a technical challenge. The developed universal controller also has two pairs of parallel control paths. One pair provides the voltage amplitude and phase-angle references for the GFM operation, and the other is for the GFL operation. However, the novelty of the developed controller is that the two pairs are always kept synchronized so that the grid-interactive inverter can seamlessly switch between the GFL and GFM modes.

Finally, to compensate for the frequency and voltage deviation inherited by decentralized power-sharing methods of the GFM inverters, a restoration technique is developed in this dissertation. Unlike the state-of-the-art methods [44, 112–117], the developed method enables the voltage and frequency restoration control at both pulse-load change and inverter plug-in events. A threshold-based method is used to identify the events for activation. Furthermore, the restoration is disabled by using a measurement-based threshold method to allow decentralized power-sharing and inverter synchronization. The controller stability is analyzed through a developed state-space model of the closed-loop GFM inverter for different parameter variations.

The contributions of the dissertation can be summarized as follows:

- The state-space model of the synchronization method, known as the controller-sync method, is developed for the GFM inverters. The effect of different parameters on the stability of the GFM inverter with the developed controller is presented. This shows that the inverter is stable at GFM mode after synchronization.

- A direct phase-angle detection method is developed to enhance the performance of the inverter controllers developed in this dissertation that can estimate phase-angle accurately without using any complicated closed-loop structure. The unique signal reformation technique of the developed method enhances the accuracy of phase-angle estimation under asymmetrical conditions of the voltage.

- A universal controller for both GFL and GFM modes of operation is developed by further modifying the controller-sync method. The universal controller expands the inverters' capability to operate in both grid-connected and islanded modes and can perform the seamless transition between the two modes.

- A communication-less voltage and frequency restoration controller is developed. The controller enables the inverter to operate at the nominal values while also enabling decentralized power-sharing capabilities. The effects of different parameters on the stability of the GFM inverter before and after the restoration are presented.

1.4 Organization of the Dissertation

The rest of this dissertation is organized as follows:

Chapter 2 presents the details of the two developed synchronization methods, i.e., output-sync and controller-sync, for the GFM inverter. The developed methods for synchronization are verified through hardware experiments in a microgrid setup of two GFM inverters. A state-space model of a GFM inverter with the controller-sync method is derived to further study the stability of the system through root-locus of the eigenvalues under different parameter variations. Chapter 2 also presents a comparative discussion between the two developed methods.

The signal reformation-based direct phase-angle detection (DPD-SR) method for asymmetrical grid conditions is presented in Chapter 3. In this chapter, the phase-angle detection method and the signal reformation techniques are derived mathematically. The efficacy and the superiority of the developed method over the conventional SRF-PLL and the state-of-the-art DDSRF-PLL are validated through both simulation and hardware experiments. The DPD-SR is used in all the developed inverter controllers in this dissertation for enhanced operation.

Chapter 4 presents a universal controller for inverters. The efficacy of the grid-interactive inverter is validated through hardware experiments for both GFL and GFM modes of operation in a grid-connected microgrid with two inverters. Chapter 4 also presents stability analysis through a state-space model of the developed controller.

Chapter 5 presents the voltage and frequency restoration method for the GFM inverters in a microgrid. State-space models with the developed controller during enabled and disabled periods are presented, and simulation results for eigenvalues for different parameter variations are presented. The performance of the developed restoration controller with the timer-based method and the threshold-based method are presented through hardware experiment scenarios in single and multi-GFM inverter scenarios are also presented in Chapter 5.

Finally, the research contribution of the developed controllers in this dissertation toward the development of the GFM inverter is summarized in Chapter 6. Chapter 6 also provides some suggestions for future works on the development of synchronization, power-sharing, phase-angle detection, and voltage and frequency restorations.

Chapter 2

Inverter Synchronization in GFM Mode

This chapter focuses on the analysis, and validation of the synchronization, i.e., inverter connection and reconnection, techniques for the inverters in GFM mode in a microgrid, where the GFM inverters are connected to different buses of the system and controlled by decentralized power-sharing methods. The contents of this chapter are organized into five sections.

Section 2.1 provides the details of the microgrid system. The first synchronization method, named the output-sync method is presented in Section 2.2. Section 2.3 discusses on the second synchronization method, named controller-sync method. The controller-sync method is utilized in this work to develop the universal controller for grid-interactive inverters, as discussed in Chapter 4. State-space model of a droop-controlled GFM inverter with the developed controller-sync method is derived for stability analysis in Section 2.4. Section 2.5 demonstrates the experimental validation of the developed synchronization methods in a microgrid testbed with two GFM inverters. Concluding remarks are given in Section 2.6.

2.1 System Configuration

In this section, the laboratory-scale microgrid which is used in this chapter is presented. The microgrid consists of two grid-interactive inverters that can be programmed for both GFL and GFM modes. The single-line block diagram of the microgrid is shown in Fig. 2.1, where the grid-interactive inverters are denoted as inverter-1 ($Inv1$) and inverter-2 ($Inv2$).

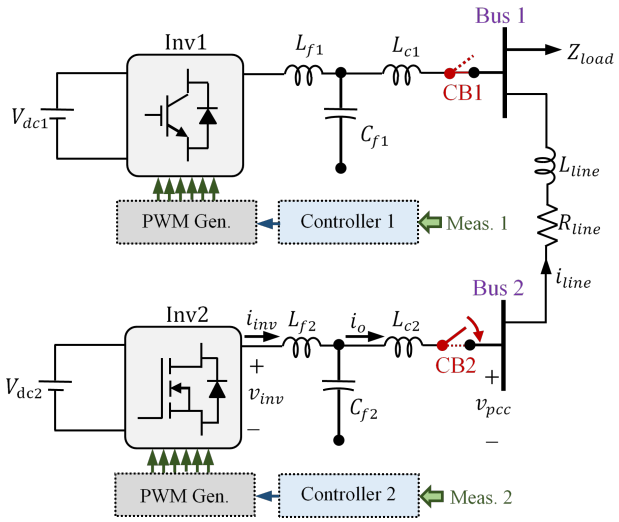

Figure 2.1: *Single-line block diagram of the microgrid under study in Chapter 2.*

$Inv1$ is connected to $Bus-1$ through a set of LCL filters and a circuit breaker, *CB1*. Similarly, $Inv2$ is connected to $Bus-2$ through another set of LCL filters and a circuit breaker, *CB2*. Each inverter is fed from a separate DC source. Each inverter is equipped with voltage measurement sensors to measure the three-phase line-line voltage at the output of the LCL filter, v_{pcc}, and current sensors to measure the output line-currents, i_o. A three-phase switched load and a continuously variable machine load are connected at the PCC of Inv1, i.e., at $Bus-1$ to add resistive and inductive loading to the microgrid. A tie-line, emulated by a series of resistors, R_{line}, and inductors, L_{line}, connects $Bus-1$ with $Bus-2$. The two inverters are run by two separate controllers, $Controller-1$ and $Controller-2$. Each converter receives the voltage and current measurements and processes the acquired measurement signals through an analog to digital conversion. A phase-angle detector is needed to obtain the voltage phase-angle, and the system frequency [19]. The controllers

provide the desired voltage amplitude and the phase-angle to the PWM signal generator blocks, which generate the necessary PWM signals. Each inverter in the microgrid can be controlled equivalently with droop or virtual-inertia; see Fig. 1.2 and Fig. 1.3. As shown in Fig. 2.1, $Inv1$ is considered as an operating inverter, forming the microgrid and supplying power to the load, and $Inv2$ is considered as an incoming inverter, intending to plug into the microgrid. The controllers developed in this chapter are applicable to any number of inverters in a microgrid, i.e., the operation of the controllers is not affected by the number of inverters.

2.2 Control Scheme for the Output-Sync Method

In this section, the output-sync method is presented in detail. Fig. 2.2 shows a GFM controller with the output-sync method. In the output-sync method, $Inv2$, the incoming inverter, connects to the microgrid in GFM mode. Prior to closing the circuit breaker, *CB2*, the amplitude and phase-angles of $Inv2$'s output voltage is synchronized with the amplitude and phase-angle of the PCC voltage at $Bus-2$. Notice that the synchronization concept of the output-sync method is inspired by state-of-the-art synchronization methods, where the inverters switch to the GFL mode from GFM mode [118] after the synchronization. The uniqueness of the output-sync method compared to the state-of-the-art technologies is, $Inv2$ can retain to operate in the GFM mode even after *CB2* is closed.

As shown in Fig. 2.2, frequency-active power, $(P-f)$, and voltage-reactive power, $(Q-V)$, droop-controls are used to adjust the frequency and the voltage reference of $Inv2$. Therefore, the active, P, and reactive power, Q, need to be estimated. In this dissertation, the instantaneous active and reactive power are calculated from the dq components of the three-phase line-line voltage and line currents using a well-known technique [31]. where abc to $dq0$ conversion is needed on the measured signals [119, 120]. The instantaneous active power, $p(t)$, and reactive power, $q(t)$, can be obtained from the following equations.

$$p(t) = \frac{3}{2}\left(v_q i_q + v_d i_d\right), \tag{2.1}$$

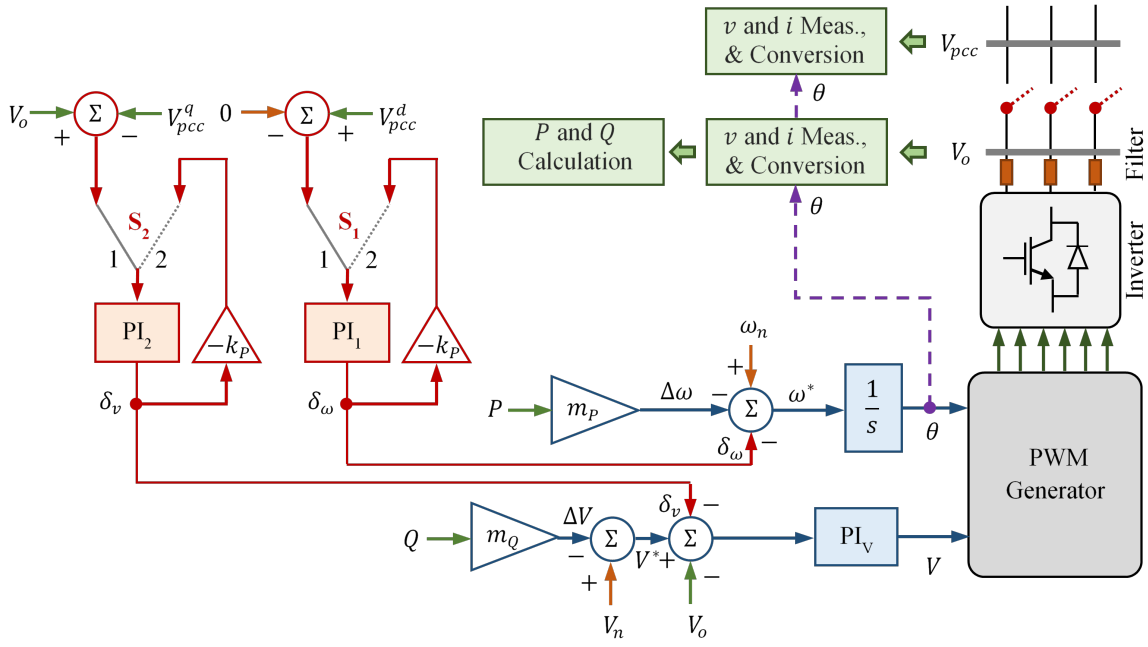

Figure 2.2: *Block diagram for the output-sync method for synchronisation.*

$$q(t) = \frac{3}{2}\left(v_q i_d - v_d i_q\right). \tag{2.2}$$

Here, v_q, v_d, and i_q, i_d are the voltage and current components after abc to $dq0$ transformation. The average active and reactive power, P and Q, are obtained from filtering the instantaneous power.

The PI controller, PI_1, is used to adjust the phase-angle reference, θ, such that the d-axis PCC voltage measurement, V_{pcc}^d becomes zero. This adjustment makes the phase-angle and the frequency of the inverter output voltage match the phase-angle and PCC voltage frequency. Similarly, PI_2 is used to adjust the voltage amplitude reference, V^* to match with the q-axis PCC voltage measurement, V_{pcc}^q. This adjustment matches the amplitude of the inverter output voltage with the PCC voltage. Therefore, the modified frequency-active power droop and voltage reactive power droop relationships become the following.

$$\omega^* = \omega_n - m_P P - \delta_\omega, \tag{2.3}$$

$$V^* = V_n - m_Q Q - \delta_v. \tag{2.4}$$

Here, ω_n, m_P, and δ_ω are the nominal angular frequency, active power droop coefficient, and angular frequency adjustment term, respectively. Similarly, V_n, m_Q, and δ_v are the nominal voltage, reactive power droop coefficient, and amplitude adjustment. The adjustment in the droop controller is also shown in Fig. 2.2. The circuit breaker, $CB2$, can be closed after the adjustment. Nevertheless, power flow from $Inv2$ is not possible if the inverter output voltage completely matches the PCC voltage. Therefore, the adjustment terms, δ_ω and δ_v, are gradually reduced to zero after the circuit breaker is closed. This task is performed by using two feedback loops, which are only activated after the closing of $CB2$. As shown in Fig. 2.2, two switches, S_1 and S_2 at the input of the two PI controllers, PI_1 and PI_2. Synchronization is made when the state switches are at Position 1. Resetting of the adjustment terms is done when the switches are at Position 2. Thus, the incoming inverter can contribute to power-sharing and continue operation in GFM mode. An inrush current control can be added at the output of PI_V. It must be mentioned that the adjustment parameters, δ_ω, and δ_v are reset gradually to zero instead of directly switching to avoid any unexpected power surge due to sudden change in phase-angle and voltage. This can result in instability and damage to the device. The developed controller can also be implemented for the stand-alone operation of GFM inverters. $Inv1$ can be controlled in GFM mode with the output-sync controller by keeping the switches at Position 2 from the beginning. Also, the frequency-active power droop control in Fig. 2.2 can be replaced by the virtual inertia-based control shown in Fig. 1.3.

2.3 Control Scheme for the Controller-Sync Method

This section presents the controller-sync method developed for GFM inverter synchronization. In the output-sync method discussed in section 2.2, voltage measurements from both sides of the circuit breaker are required before the CB is closed. On the contrary, in the controller-sync method, the incoming inverter performs synchronization by using only the microgrid-side voltage measurements. However, the incoming inverter, $Inv2$, cannot operate in GFM mode if the circuit breaker connecting the inverter with the microgrid is open.

Therefore, the circuit breaker must be closed all the time while ensuring no power is injected from the incoming inverter in GFL mode. The controller-sync method developed in this dissertation can connect the incoming inverter in GFL mode with zero power injection and then switch to the GFM mode.

Fig. 2.3 depicts the control block diagram of the controller-sync method. Here, the voltage and phase-angle reference input to the PWM generator can be provided from two different sets of control paths, represented by state switch Positions 1 for GFL control and Position 2 for GFM control. In the controller-sync method, $Inv2$ starts operating with the state switches, S_1 and S_2, at Position 1. Using the phase-angle measurement, θ_{PLL}, and the voltage measurements, V_{pcc}, the phase-angle and amplitude of the inverter output voltage are synchronized with the voltages at the PCC. Notice that a proportional-integral block, PI_V, is required to establish the voltage control. While synchronized, $Inv2$ regulates the active power, P, using PI_4, and the reactive power, Q, using PI_2 to zero. Thus, the inverter is connected to the system but does not contribute to any power injection, i.e., $Inv2$ is in standby mode. The PI controllers, PI_3 and PI_1, are activated when power injection from the incoming inverter is needed. Here, PI_3 controls the active power injection based on the difference between the reference angular frequency, ω^* and ω_{PLL}. The droop parameter, m_P, of $Inv2$ establishes the active power-sharing with other inverters in the system. Similarly, PI_1 controls the reactive power injection based on the difference between the reference voltage amplitude, V^* and V_{pcc}. Reactive power-sharing is established by the droop parameter, m_Q. Notice that in the controller-sync method, the output of the GFM control paths at Position 2 is adjusted to synchronize with the output of the GFL control path while the incoming inverter operates in GFL mode. Therefore, the developed method is called the controller-sync method. In the active power control path, PI_5 ensures the phase-angle of the GFM and the GFL control paths match. Instantaneous variations in the angle are avoided by using a zero-order hold (ZOH) that samples data once every cycle. Similarly, the two outputs of the voltage control paths are synchronized by PI_V. When the outputs of the controller are synchronized, i.e., $\theta_2 = \theta_1$ and $V_2 = V_1$, the switches S_1 and S_2 move to Position 2 and the inverter shifts to GFM mode. By matching the phase-angles and the voltage amplitudes,

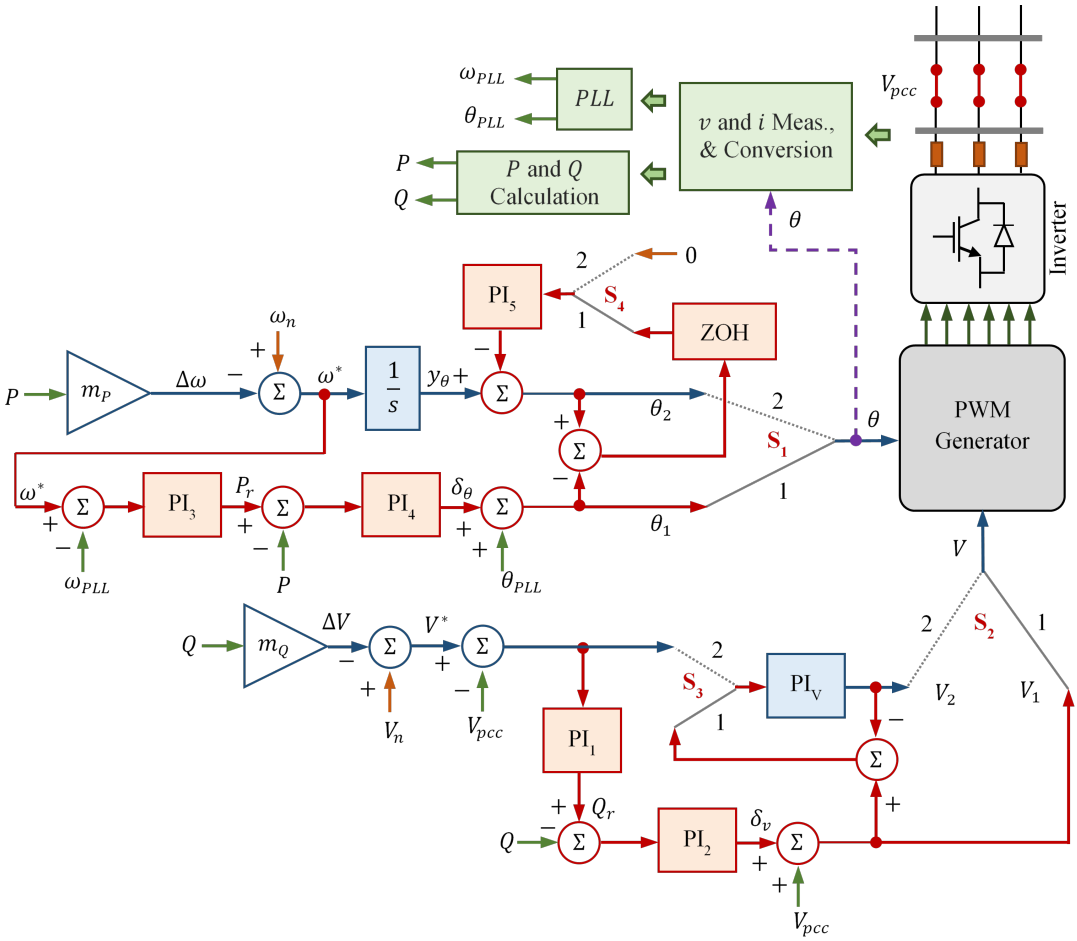

Figure 2.3: *Block diagram for the controller-sync method.*

the developed controller-sync method can establish seamless transition from GFL to GFM mode of operation.

A unique feature of the controller-sync method is that this method can allow an inverter to stay connected to the system without injecting any power, which is very useful in a microgrid system, where some inverters need to stay on standby to be used immediately, i.e., when the microgrid is disconnected from the main grid, and the load is more than the capacity of the already operating inverters. Another unique feature is that this method does not require two sets of measurements for synchronization, making the system reliable and more economical. Finally, unlike any other state-of-the-art methods and the developed output-sync method, power-sharing can be achieved even without switching to the GFM mode of operation. Similar to the output-sync method, the droop controller in the controller-sync

method can also be replaced by the virtual inertia-based control in Fig. 1.3.

2.4 State-Space Modeling of Controller-Sync Method

In this section, a state-space model of the controller-sync method in Section 2.3 is derived for stability analysis. Referring to Fig. 2.3 it is observed that two state-space models exist for the two positions of the switches associated with the two control paths.

When the switch is at Position 1, the equation for the engaged phase-angle reference can be obtained from

$$\theta_1 = \theta_{PLL} + k_{P4}(P_r - P) + y_4, \tag{2.5}$$

where, θ_1 is the input phase-angle reference to the PWM block, θ_PLL is the phase-angle measurement at the PCC, k_{P4} is the proportional gain parameter of PI_4, and $y4$ is the output of the integrator of PI_4. The output of PI_3, P_r is expressed as

$$P_r = k_{P3}\left(\omega^* - \omega_{PLL}\right) + y_3. \tag{2.6}$$

Here, y_3 is the outputs of the integrator blocks in PI_3. The angular frequency reference, ω^* is obtained from the frequency-active power droop relationship, and can be calculated as,

$$\omega^* = \omega_n - m_P P. \tag{2.7}$$

Combining (2.5), (2.6), and (2.7), equation for the phase-angle reference can be developed as,

$$\theta_1 = \theta_{PLL} + k_{P4}(k_{P3}\left(\omega_n - m_P P - \omega_{PLL}\right) + y_3 - P) + y_4 \tag{2.8}$$

Linearizing (2.8) around an operating point yields

$$\delta\theta_1 = \delta y_4 + k_{P4}\delta y_3 - k_{P4}(m_P k_{P3} + 1)\delta P + \delta\theta_{PLL} - k_{P4}k_{P3}\delta\omega_{PLL} \tag{2.9}$$

The input of the integrator block of PI_3, $\dot{y}_3$, and the input to the integrator block of PI_4, $\dot{y}_4$ are expressed as

$$\dot{y}_3 = k_{I3}\left(\omega_n - m_P P - \omega_{PLL}\right) \tag{2.10}$$

and

$$\dot{y}_4 = k_{I4}(k_{P3}\left(\omega_n - m_P P - \omega_{PLL}\right) + y_3 - P) \tag{2.11}$$

Linearizing (2.10) and (2.11) gives

$$\dot{\delta y}_3 = -k_{I3} m_P \delta P - k_{I3} k_{p3} \delta\omega_{PLL}, \tag{2.12}$$

and

$$\dot{\delta y}_4 = k_{I4}\delta y_3 - k_{I4}\left(k_{P3} m_P + 1\right)\delta P. \tag{2.13}$$

Notice that the derivative of ω_n in (2.9), (2.12), and (2.13) is zero as ω_n is a constant number, typically 314.16 rad/s or 376.99 rad/s.

Similarly, equation for the engaged voltage amplitude reference can be obtained from

$$V_1 = V_{pcc} + k_{P2}(Q_r - Q) + y_2, \tag{2.14}$$

where, V_1 is the input voltage amplitude reference to the PWM block, V_PCC is voltage amplitude at the PCC, k_{P2} is the proportional gain parameter of PI_2, and $y2$ is the output of the integrator of PI_2. Notice that the inrush-current regulation path is omitted from the equation considering normal operating conditions. The output of PI_1, Q_r can be expressed as

$$Q_r = k_{P1}\left(V^* - V_{pcc}\right) + y_1. \tag{2.15}$$

Here, y_1 is the outputs of the integrator blocks in PI_1. The voltage amplitude reference, V^* is obtained from the voltage-reactive power droop relationship, and is calculated as,

$$V^* = V_n - m_Q Q, \tag{2.16}$$

where, y_1 and y_2 are the outputs of the integrator blocks in PI_1 and PI_2, respectively. Expression of the voltage amplitude reference can be finalized by combining (2.14), (2.15), and (2.16) as follows

$$V_1 = V_{pcc} + k_{P2}(k_{P1}\left(V_n - m_Q q - V_{pcc}\right) + y_1 - Q) + y_2 \tag{2.17}$$

Linearizing (2.17) yields

$$\delta V_1 = \delta y_2 + k_{P2}\delta y_1 - k_{P2}(m_Q k_{P1} + 1)\delta Q + \left(1 - k_{P2}k_{P1}\right)\delta V_{pcc}. \tag{2.18}$$

The inputs of the integrator blocks in PI_1 and PI_2, $\dot{y}_1$ and $\dot{y}_2$, is expressed as

$$\dot{y}_1 = k_{I1}\left(V_n - m_Q Q - V_{pcc}\right), \tag{2.19}$$

and

$$\dot{y}_2 = k_{I2}(k_{P1}\left(V_n - m_Q Q - V_{pcc}\right) + y_1 - Q). \tag{2.20}$$

Linearizing (2.19) and (2.20) will produce

$$\dot{\delta y}_1 = -k_{I1}m_Q\delta Q - k_{I1}\delta V_{pcc}, \tag{2.21}$$

and

$$\dot{\delta y}_2 = k_{I2}\delta y_1 - k_{I2}\left(k_{P1}m_Q + 1\right)\delta.Q - k_{I2}k_{P1}\delta V_{pcc} \tag{2.22}$$

Here, V_n is a constant, typically 208 $V(rms)$ and the derivative, δV_n is zero.

The active and reactive power injection for switch position 1 can be calculated from (2.1) and (2.2). Linearizing these equations around the operating point yields

$$\delta P = (3/2)\, V_{qpcc0}\delta i_q + (3/2)\, I_{q0}\delta v_{qpcc}, \tag{2.23}$$

and

$$\delta Q = (3/2)\, V_{qpcc0}\delta i_d + (3/2)\, I_{d0}\delta v_{qpcc}. \tag{2.24}$$

Here, i_q and i_d represent the components of the inverter current, i_{inv}, after abc to dq transformation. Neglecting the capacitor in Fig. 2.1, the inverter current can be approximately be equal to the output current, i.e., $i_{inv} \approx i_o$. The voltages, v_{qpcc} and v_{dpcc} represent the dq-axis components of v_{pcc}. The d-axis component, $v_{dpcc} = 0$, when the PCC voltage is considered as the reference for phase-angle estimation. Therefore, δV_{pcc} can be written as δv_{qpcc}.

A simplified current flow equations from the inverter to the output circuit can be derived from Fig. 2.1 as

$$\frac{di}{dt} = -\frac{R}{L}i + \frac{1}{L}v - \frac{1}{L}v_{pcc}, \tag{2.25}$$

where, the capacitor current is neglected and the two inductors of the LCL filter are lumped as $L = L_f + L_c$. Also, R is the inherent resistance of the inductors. The current flow equation in (2.25) can be represented in dq-axis as,

$$\frac{di_q}{dt} = -\frac{R}{L}i_q + \frac{1}{L}v_q - \frac{1}{L}v_{qpcc} - \omega i_d, \tag{2.26}$$

and

$$\frac{di_d}{dt} = -\frac{R}{L}i_d + \frac{1}{L}v_d + \omega i_q, \tag{2.27}$$

Linearizing (2.26) and (2.27) around an operating point yields,

$$\frac{d\delta i_q}{dt} = -\frac{R}{L}\delta i_q + \frac{1}{L}\ \delta v_q - \frac{1}{L}\delta v_{qpcc} - \omega\delta i_d, \tag{2.28}$$

and

$$\frac{d\delta i_d}{dt} = -\frac{R}{L}\delta i_d + \frac{1}{L}\ \delta v_d + \omega\delta i_q. \tag{2.29}$$

Notice that, v_q and v_d represent the components of the inverter voltage, v_{inv}, in dq reference frame. Assuming the inverter phase voltage, v_{inv}, expressed as $v_{inv}(t) = V_1 cos\,(\theta_1)$, where the reference voltage amplitude, V_1, and the reference phase-angle, θ_1, are provided by the

controller at position 1. Therefore, the dq-axis components of the inverter voltage can be expressed as

$$v_q = V_1 \, cos\left(\theta_1\right), \tag{2.30}$$

and

$$v_d = -V_1 \, sin\left(\theta_1\right), \tag{2.31}$$

which can be linearized as,

$$\delta v_q = cos\left(\theta_{10}\right) \delta V_1 - V_{10} sin\left(\theta_{10}\right) \delta\theta_1, \tag{2.32}$$

and

$$\delta v_d = -sin\left(\theta_{10}\right) \delta V_1 - V_{10} cos\left(\theta_{10}\right) \delta\theta_1. \tag{2.33}$$

Substituting $\delta\theta_1$ from (2.9), and δV_1 from (2.18) in (2.32) and (2.33) yields

$$\begin{aligned} \delta v_q = {} & cos\left(\theta_{10}\right) \left(\delta y_2 + k_{P2}\delta y_1 - k_{P2}(m_Q k_{P1} + 1)\delta Q + \left(1 - k_{P2}k_{P1}\right) \delta V_{pcc}\right) \\ & -V_{10} sin\left(\theta_{10}\right) \left(\delta y_4 + k_{P4}\delta y_3 - k_{P4}(m_P k_{P3} + 1)\delta P + \delta\theta_{PLL} - k_{P4}k_{P3}\delta\omega_{PLL}\right), \end{aligned} \tag{2.34}$$

and

$$\begin{aligned} \delta v_d = {} & -sin\left(\theta_{10}\right) \left(\delta y_2 + k_{P2}\delta y_1 - k_{P2}(m_Q k_{P1} + 1)\delta Q + \left(1 - k_{P2}k_{P1}\right) \delta V_{pcc}\right) \\ & -V_{10} cos\left(\theta_{10}\right) \left(\delta y_4 + k_{P4}\delta y_3 - k_{P4}(m_P k_{P3} + 1)\delta P + \delta\theta_{PLL} - k_{P4}k_{P3}\delta\omega_{PLL}\right). \end{aligned} \tag{2.35}$$

Substituting (2.23) and (2.24) in (2.9)−(2.13), (2.18), (2.21), and (2.22) and combining

with (2.28) and (2.29), the state-space model of the closed-loop inverter can be formed as

$$\frac{d}{dt}\begin{bmatrix}\delta i_q\\ \delta i_d\\ \delta y_1\\ \delta y_2\\ \delta y_3\\ \delta y_4\end{bmatrix} = \begin{bmatrix}a_{11} & a_{12} & a_{13} & a_{14} & a_{15} & a_{16}\\ a_{21} & a_{22} & a_{23} & a_{24} & a_{25} & a_{26}\\ a_{31} & a_{32} & a_{33} & a_{34} & a_{35} & a_{36}\\ a_{41} & a_{42} & a_{43} & a_{44} & a_{45} & a_{46}\\ a_{51} & a_{52} & a_{53} & a_{54} & a_{55} & a_{56}\\ a_{61} & a_{62} & a_{63} & a_{64} & a_{65} & a_{66}\end{bmatrix}\begin{bmatrix}\delta i_q\\ \delta i_d\\ \delta y_1\\ \delta y_2\\ \delta y_3\\ \delta y_4\end{bmatrix} + \begin{bmatrix}b_{v1} & b_{\theta 1} & b_{\omega 1}\\ b_{v2} & b_{\theta 2} & b_{\omega 2}\\ b_{v3} & b_{\theta 3} & b_{\omega 3}\\ b_{v4} & b_{\theta 4} & b_{\omega 4}\\ b_{v5} & b_{\theta 5} & b_{\omega 5}\\ b_{v6} & b_{\theta 6} & b_{\omega 6}\end{bmatrix}\begin{bmatrix}\delta v_{qpcc}\\ \delta\theta_{PLL}\\ \delta\omega_{PLL}\end{bmatrix} \tag{2.36}$$

The matrix elements in (2.36) are provided in Appendix A.1.

The state-space model for Position 2 can be obtained in similar approach. The phase-angle at position 2 can be directly obtained from Fig. 2.3 as,

$$\theta_2 = y_\theta, \tag{2.37}$$

and the voltage amplitude can be obtained as

$$V_2 = k_{PV}\left(V_n - m_Q Q - V_{pcc}\right) + y_V. \tag{2.38}$$

The input to the integrator block for phase-angle control, $\dot{y}_\theta$, is expressed as,

$$\dot{y}_\theta = \omega_n - m_P P. \tag{2.39}$$

Also the inputs to the integrator blocks in PI_V, $\dot{y}_V$, is expressed as,

$$\dot{y}_V = k_{IV}\left(V_n - m_Q Q - V_{pcc}\right). \tag{2.40}$$

Linearizing (2.37) and (2.38) yields,

$$\delta\theta_2 = \delta y_\theta, \tag{2.41}$$

and

$$\delta V_2 = -k_{PV} m_Q \delta Q + \delta y_V - k_{PV} \delta V_{pcc}. \tag{2.42}$$

Also, linearizing (2.39) and (2.40) yields,

$$\dot{\delta y}_\theta = -m_P \delta P, \tag{2.43}$$

and

$$\dot{\delta y}_V = -k_{IV} m_Q \delta Q - \ k_{IV} \delta V_{pcc}. \tag{2.44}$$

At position 2, the inverter phase voltage, v_{inv}, is expressed as $v_{inv}(t) = V_2 cos\left(\theta_2\right)$, where the reference voltage amplitude, V_2, and the reference phase-angle, θ_2, are provided by the controller. Therefore, the dq-axis components of the inverter voltage can be expressed as

$$v_q = V_2 \, cos\left(\theta_2\right), \tag{2.45}$$

and

$$v_d = -V_2 \, sin\left(\theta_2\right), \tag{2.46}$$

which can be linearized as,

$$\delta v_q = cos\left(\theta_{20}\right) \delta V_2 - V_{20} sin\left(\theta_{20}\right) \delta\theta_2, \tag{2.47}$$

and

$$\delta v_d = -sin\left(\theta_{20}\right) \delta V_2 - V_{20} cos\left(\theta_{20}\right) \delta\theta_2. \tag{2.48}$$

Substituting (2.41) and (2.42) in (2.47) and (2.48) results in

$$\delta v_q = cos\left(\theta_{20}\right) \left(-k_{PV} m_Q \delta Q + \delta y_V - k_{PV} \delta V_{pcc}\right) - V_{20} sin\left(\theta_{20}\right) \delta y_\theta, \tag{2.49}$$

and

$$\delta v_d = -sin\left(\theta_{20}\right) \left(-k_{PV} m_Q \delta Q + \delta y_V - k_{PV} \delta V_{pcc}\right) - V_{20} cos\left(\theta_{20}\right) \delta y_\theta. \tag{2.50}$$

The state-space model can be developed by combining (2.23)−(2.29), (2.39), (2.40), (2.39), and (2.40) as follows.

$$\frac{d}{dt}\begin{bmatrix}\delta i_q\\ \delta i_d\\ \delta y_\theta\\ \delta y_V\end{bmatrix} = \begin{bmatrix}\alpha_{11} & \alpha_{12} & \alpha_{13} & \alpha_{14}\\ \alpha_{21} & \alpha_{22} & \alpha_{23} & \alpha_{24}\\ \alpha_{31} & \alpha_{32} & \alpha_{33} & \alpha_{34}\\ \alpha_{41} & \alpha_{42} & \alpha_{43} & \alpha_{44}\end{bmatrix}\begin{bmatrix}\delta i_q\\ \delta i_d\\ \delta y_\theta\\ \delta y_V\end{bmatrix} + \begin{bmatrix}\beta_1\\ \beta_2\\ \beta_3\\ \beta_4\end{bmatrix}\delta v_{qpcc}. \tag{2.51}$$

The matrix elements in (2.51) are available in Appendix A.1.

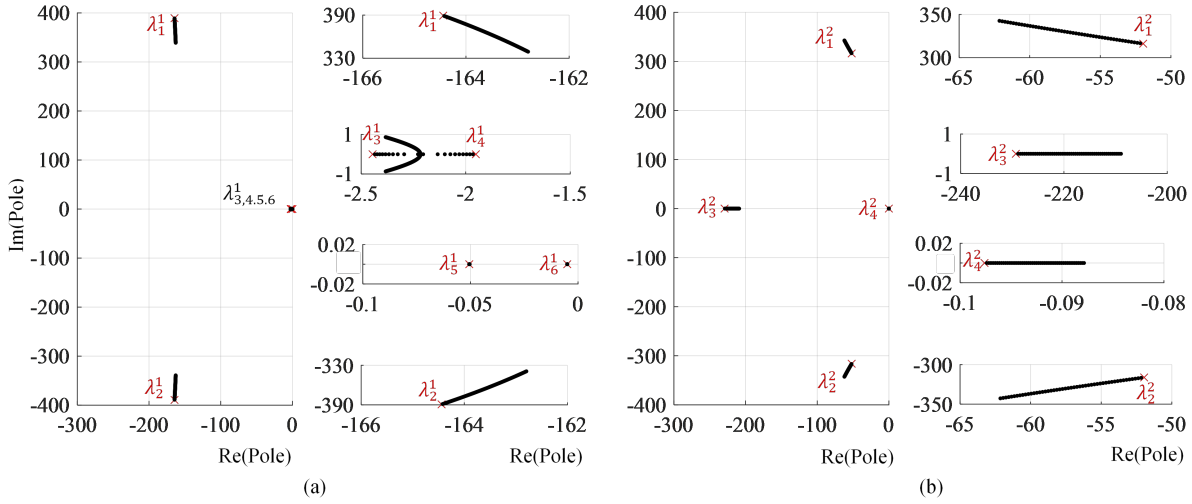

Figure 2.4: *Eigenvalues of Inv2 with closed-loop control by the proposed controller-sync method. Root-locus when the controller switch is at Position 1 with Inv2's active power-injection increasing from* 0 *to* 10 *kW and then the controller switch is at Position 2 with Inv2's active power decreasing from* 10 *kW to* 5 *kW.*

Root locus of the eigenvalues at different active power levels for Position 1 and Position 2 of the switch are plotted in Fig. 2.4 and Fig. 2.5. Fig. 2.4(a)-left shows the eigenvalues when the incoming inverter is connected to the system and gradually increases active power injection from 0 *kW* to 10 *kW*. The red crosses on the plot show the eigenvalues at the initial state. The expanded plot for the six eigenvalues, λ^1_{1-6}, are shown in Fig. 2.4(a)-right. Notice that the system is stable for the tested power levels, indicated by the position of all the eigenvalues on the left-half plane. Then the controller switches to Position 2,

and the incoming inverter reduces its active power injection from 10 kW to 5 kW. The eigenvalues for Position 2 are shown in Fig. 2.4(b)-left. This state has four eigenvalues, i.e., λ^2_{1-4}. Fig. 2.4(b)-right shows the expanded plots of the eigenvalues. Here also, the eigenvalues stay in the left-half plane. Therefore, the system remains stable under both switch positions. Fig. 2.5 shows a similar scenario, where the incoming inverter gradually increases active power from 0 kW to 10 kW, and then switches to Position 2, and increases active power injection from 10 kW to 20 kW. All eigenvalues for the two switch positions stay on the left-half plane for this scenario too. Notice that for the second scenario, the expanded plot in Fig. 2.5(b)-right shows that the eigenvalues, λ^2_{1-2}, at position move toward the imaginary axis if excessive power is injected after switching to Position 2.

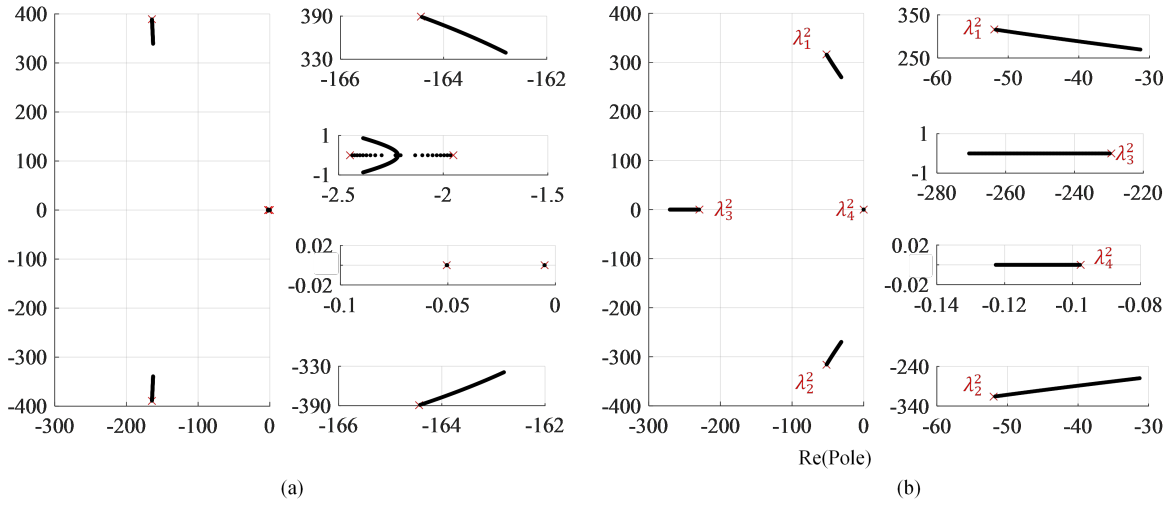

Figure 2.5: *Eigenvalues of Inv2 with closed-loop control by the proposed controller-sync method. Root-locus when the controller switch is at position 1 with Inv2's active power-injection increasing from* 0 *to* 10 *kW and then the controller switch is at position 2 with Inv2's active power increases from* 10 *kW to* 20 *kW.*

2.5 Experimental Verification

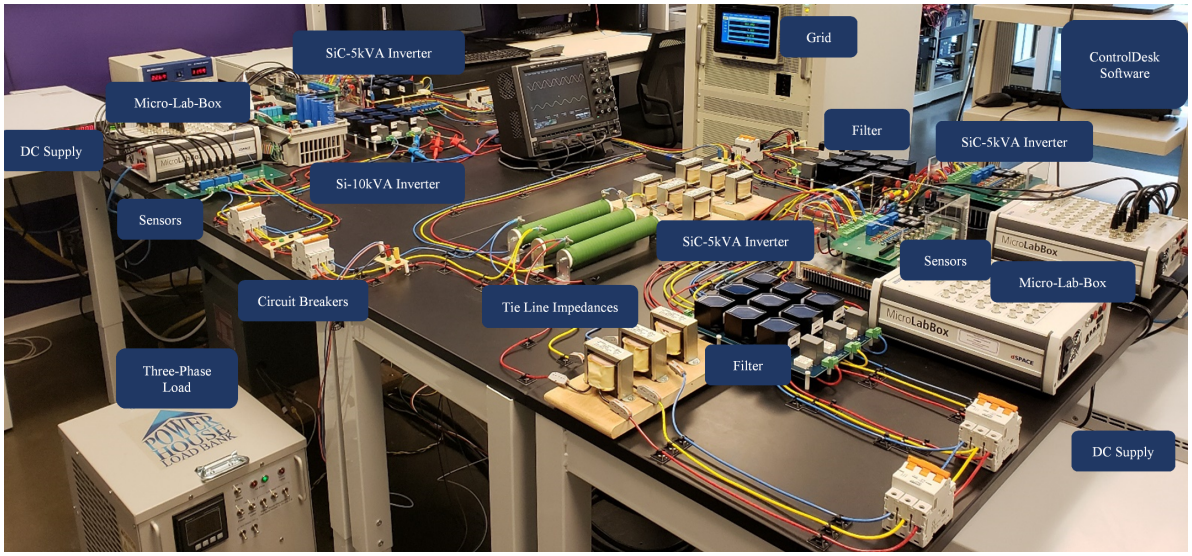

Figure 2.6: *Experimental setup of the laboratory-scaled microgrid of four inverters.*

In this section, the output-sync method and the controller-sync method are experimentally verified two a set of laboratory experiments. Fig. 2.6 shows the microgrid test-bed in which the test is performed. The microgrid consists of three 5 kVA laboratory assembled inverters built with SiC 1200 V, 20 A six-pack modules and a commercial Allen-Bradley Powerflex 755, 10 kVA Si inverter. The inverters are powered by four separate $6kW$ programmable DC-power sources. The PWM signals are provided using four dSPACE 1202 MicroLabBox controllers, where the closed-loop controls are implemented. Each inverter setup is equipped with LCL filters, voltage and current measurement sensors, and circuit breakers. Two three-phase 5 kW variable resistive loads are connected at two different nodes of the microgrid. All data are acquired by the ControlDesk of dSPACE and then plotted by MATLAB. All inverters can be programmed for both GFL and GFM modes. The microgrid is also connected to a 30 kVA NHR-9410 grid-emulator through a circuit breaker for grid-connected operations. The experiments presented in this section only consider two inverters in GFM modes. The system parameters used for the experiment performed for this section are presented in Table 2.1, and the control parameters are in Table 2.2. Both methods are verified for droop-based and virtual inertia-based power-sharing control. For droop-based

control, the droop gain parameters, m_P and m_Q, are set to 0.005 and 0.001, respectively. For virtual inertia-based sharing, the inertia constant, J, and the damping coefficient, D, are set to 0.04 and 100, respectively.

Table 2.1: *System Parameters for Inverters in Chapter 2*

Parameter	Value
Nominal line-line voltage, V_n	208 V
DC bus voltage, V_{dc}	350 V
Nominal frequency, ω_n	$2\pi(60)$ rad/s
PWM switching frequency, f_{PWM}	5 kHz
Filter inductance, L_f	1 mH
Coupling inductance, L_c	0.5 mH
Filter capacitance, C_f	5 μF (Δ)
Filter damping resistance, R_{cf}	1.65 Ω (Δ)
Tie-line inductance, L_{line}	5 mH
Tie-line resistance, R_{line}	1 Ω

Table 2.2: *Controller Parameters for Inverters in Chapter 2*

Method	Controller	k_P	k_I
Both	PI_V	0.0005	0.25
Methods	X_{vir}	5.5	–
Output-Sync	PI_1	0.02	0.25
	PI_2	0.02	0.25
	Reset control	0.8	–
Controller-Sync	PI_1	0.05	5
	PI_2	0.0001	0.005
	PI_3	0.5	10
	PI_4	0	0.0001
	PI_5	0.1	1

2.5.1 Inverter Connection without Synchronization

In this test, the need of proper synchronization of the GFM inverters in an islanded microgrid is demonstrated. In this study the incoming inverter, $Inv2$, directly connected to a system

where $Inv1$ is supplying 475 W of active power to the load. The synchronization control is disabled.

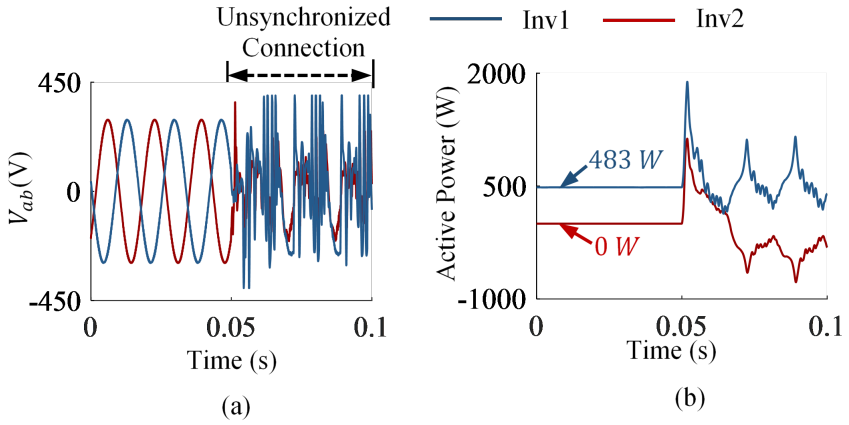

Figure 2.7: *Experimental demonstration of a microgrid in case of improperly synchronized switching; (a) line-to-line voltage, and (b) active power obtained experimentally.*

Fig. 2.7 shows that the voltage and the active power of of both the inverters are distorted after the connection. This is due to the difference in frequencies and voltage magnitudes on both sides of the circuit breaker. Hence, any incoming inverter must be synchronized prior to contributing to the power-sharing in an islanded microgrid. It is important to note that, such connection may lead to damages of the devices in the microgrid as voltage swell can occur at the DC-bus.

2.5.2 Inverter Synchronization with Output-Sync Method

The efficacy of the developed output-sync method in synchronization and power-sharing is demonstrated here. In the first scenario, $Inv1$ is an operating inverter in the microgrid, supplying active power to a load. $Inv2$ is an incoming inverter that first synchronizes with the microgrid, gets connected to the system, and contributes to power-sharing through droop control. The circuit breaker, $CB2$ remains disconnected prior to synchronization. $Inv2$ starts at no load and begin synchronization when the switches $S_{1,2}$ are at position 1. Fig. 2.8 shows the line-line voltage, V_ab, of $Inv1$ and $Inv2$, before, during and after the synchronization. As seen through Figs. 2.8(a)-(c), the synchronization control of $Inv2$ gradually matches it's

voltage amplitude and frequency with the parameters of $Inv1$ with PI_1 and PI_2. Fig. 2.9

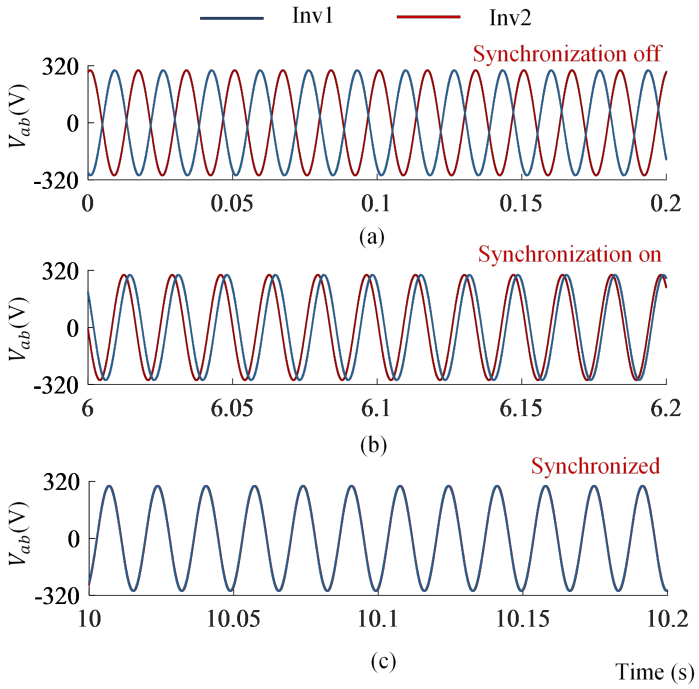

Figure 2.8: *Line-to-line voltage, V_{ab}, of $Inv1$ and $Inv2$; (a) when the synchronization process is off, (b) during the synchronization process, and (c) after the synchronization.*

shows the frequency, active and reactive power sharing scenarios of the two inverter. As seen in Fig. 2.9(a), the frequency of the system is at 374.6 rad/s. This is because $Inv1$ is supplying 483 W of active power, Fig. 2.9(b), and the droop controller reduces the frequency from 377 rad/s. The synchronization begins at $t = t_1$. Fig. 2.9 shows that $Inv2$'s frequency is being adjusted during the synchronization. At $t = t_2$, $CB2$ is connected and the switches are immediately switched to position 2. Then, as δ_ω and δ_v gradually approach zero, $Inv2$ contributes to power-sharing. Notice that eventually both inverters are sharing 239 W of active power and the frequency of the system reaches to 378.8 rad/s. After this, for any load change, e.g., an additional 1 kW at $t = t_3$, the the system frequency changes while the two GFM inverters are in sync, and the power-sharing is established, see Fig. 2.9(b). Fig. 2.9(c) shows the reactive power injection by the two inverters where one inverter is injecting power while the other absorbs. Nevertheless, reactive power-sharing is not possible as it is impractical to control all the four parameters, i.e., voltage, frequency, active power and

reactive power, simultaneously. This test proves that the output-sync method can perform synchronization and power-sharing operation for an incoming inverter.

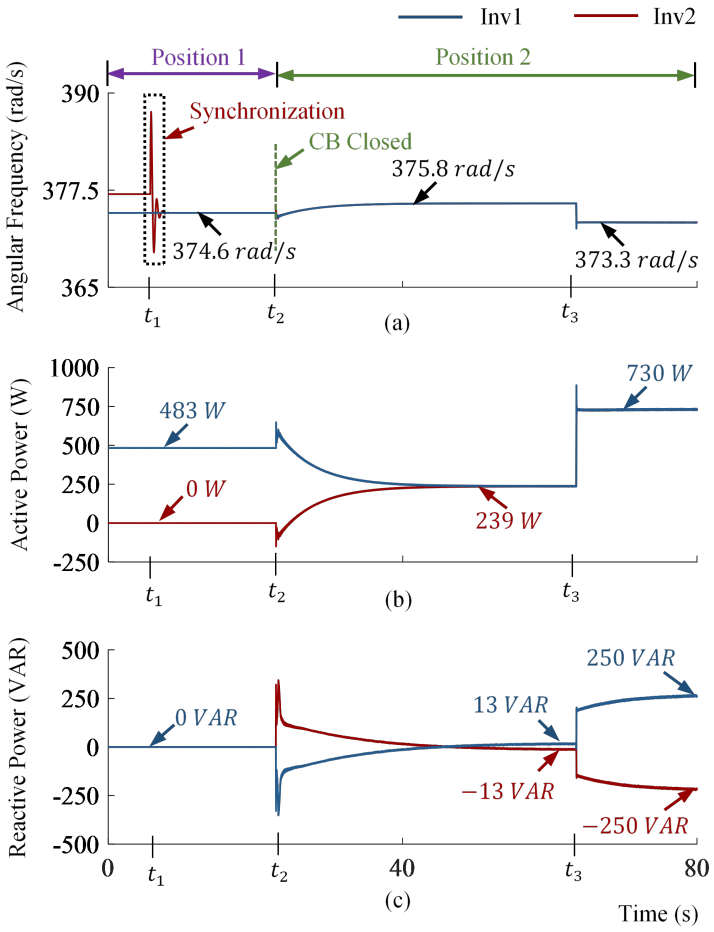

Figure 2.9: *Experimental verification of the output-sync method with droop control for power-sharing; (a) angular frequency of the system and Inv2, (b) active power, and (c) reactive power contribution by Inv1 and Inv2.*

In the second scenario, $Inv2$ first synchronizes with the microgrid, gets connected to the system, and contributes to power-sharing through virtual inertia control. Notice that only the droop control of Fig. 2.2 is replaced by the virtual inertia control of Fig. 1.3, while the synchronization process remains the same. Similar to the previous scenario, $Inv1$ is operating with a load of 483 W while $Inv2$ connects to the microgrid. As shown in Fig. 2.10(a), the synchronization process begins at $t = t_1$ and the switch position shifts to position 2 at $t = t_2$. Power-sharing is gradually achieved between the two inverters. Fig. 2.10(b) shows that the

two inverters are able to accurately share the active power in GFM mode as an additional 1 kW load is switched on and off at $t = t_3$ and $t = t_d$, respectively. Nevertheless, the reactive power is not share, but only exchanged between the inverters, see Fig. 2.10(c). Fig. 2.10(a) also demonstrates the advantage of virtual inertia over droop as seen in Fig. 2.9(a). Notice that the frequency deviation is very low in virtual inertia compared to the droop. This test verifies that the developed output-sync method is also applicable with virtual-inertia based power-sharing.

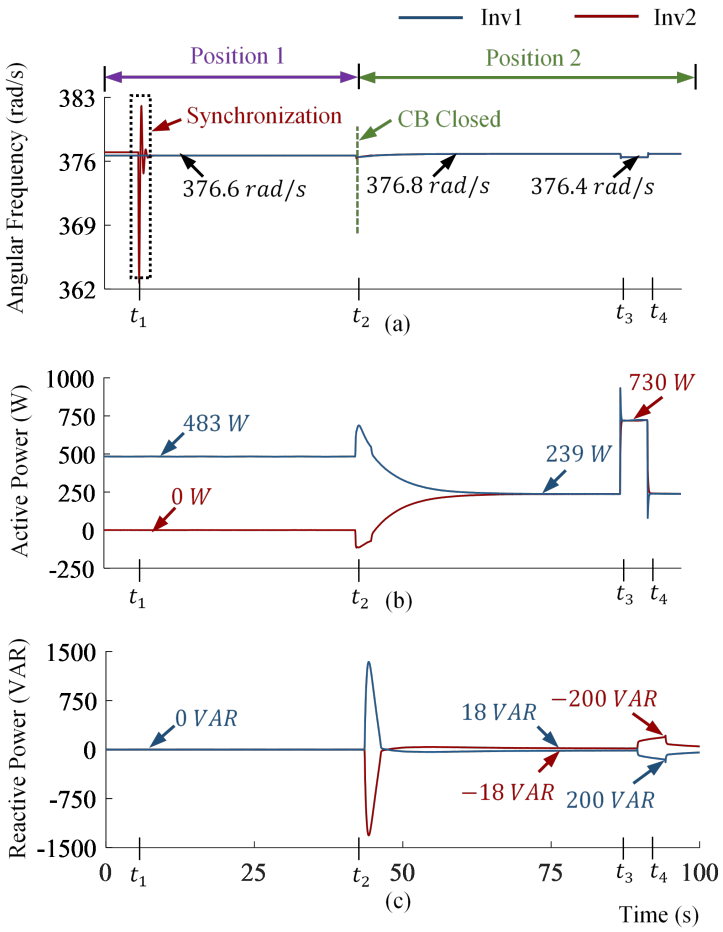

Figure 2.10: *Experimental verification of the output-sync method with virtual inertia for power-sharing; (a) angular frequency of the system and Inv2, (b) active power, and (c) reactive power contribution by Inv1 and Inv2.*

Fig. 2.11 shows a picture during the data acquisition of Fig.2.9 for experimental verification of the output-sync method.

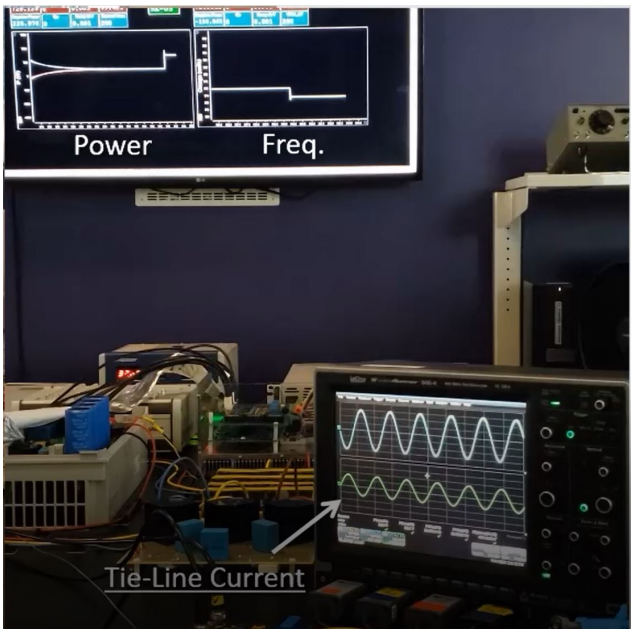

Figure 2.11: *Experimental verification of the output-sync method.*

2.5.3 Inverter Synchronization with Controller-Sync Method

The developed controller-sync method is experimentally verified for synchronization and power-sharing in this section. The controller is tested with both droop control and virtual inertia control for power-sharing. For both cases, the circuit breaker remains connected before $Inv2$ starts injecting power into the system.

In the first scenario, $Inv1$ is an operating inverter in the microgrid, supplying active power to a load. $Inv2$, the incoming inverter, first synchronizes gets connected to the system in GFL mode, without injecting any power, synchronizes the control paths for GFM operation, and then switches to GFM mode to contribute to power-sharing through droop control. Fig. 2.12 shows the phase-angle of the GFM control path of $Inv2$ in comparison with the phase-angle of $Inv1$ at the PCC of $Inv2$ before, during and after the synchronization.

Fig. 2.13 shows the system frequency, the active power-injection, the PCC voltage amplitudes, and the reactive power injection by the two inverters. Notice that $Inv1$ is injecting 483 W of active power while the active power injection by $Inv2$ is 0. For demonstration purposes, in this test, PI_1 and PI_3 are disabled for $t < t_1$ to reset P_r and Q_r to zero. The goal is to make the outputs of the parallel control paths for both V and θ equal, i.e., $V_1 = V_2$

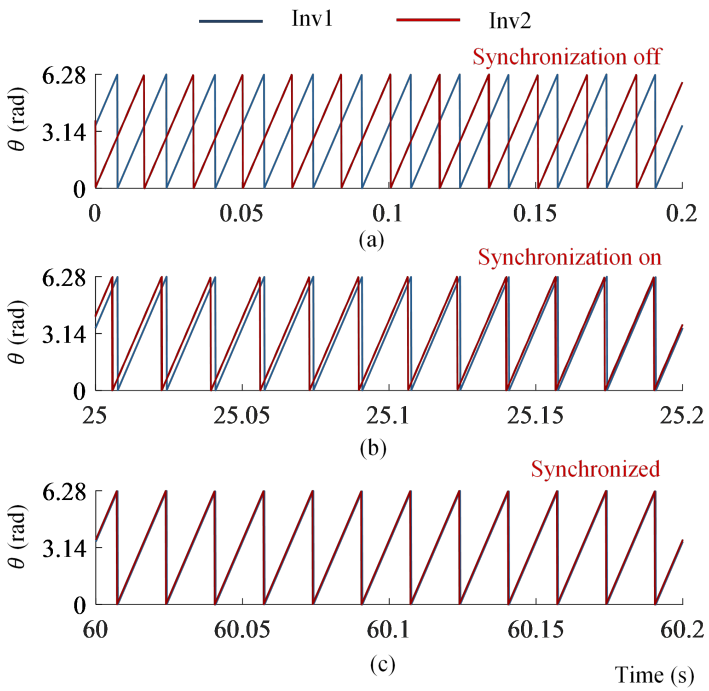

Figure 2.12: *Phase-angles of $Inv1$ and of the GFM control path of $Inv2$; (a) before, (b) during, and (c) after synchronization.*

and $\theta_1 = \theta_2$. At $t = t_1$, the GFL control path starts contributing power by activating PI_1 and PI_3. The GFM control path is also being synchronized simultaneously. Fig. 2.13(a) shows that the frequency of the GFM control path is gradually synchronized with the system frequency, i.e., $Inv1$'s frequency. Thus, with droop control, the active power is also being shared, see Fig. 2.13(b). At the same time, the voltage amplitudes are also being synchronized. Notice that $Inv2$ remains at GFL mode, i.e., switches are at position 1. Then, $Inv2$ switches to GFM mode as the switches shift to position 2. Very small transients in the active and reactive power-sharing are observed as the two control paths are synchronized. Once the switches are at position 1, the two inverters operate in GFM mode autonomously and contribute to power-sharing as the load changes occur at $t = t_3$ and $t = t_4$. Fig. 2.12(b) shows the amplitudes of the PCC voltages of $Inv1$ and $Inv2$ are being controlled around 208 $V(rms)$. Since it is a two inverter system, the reactive power generated by one inverter is being absorbed by the other one, see Fig. 2.12(d). Nonetheless, simultaneous reactive power sharing is not possible when frequency, voltage and active power-sharing is being controlled.

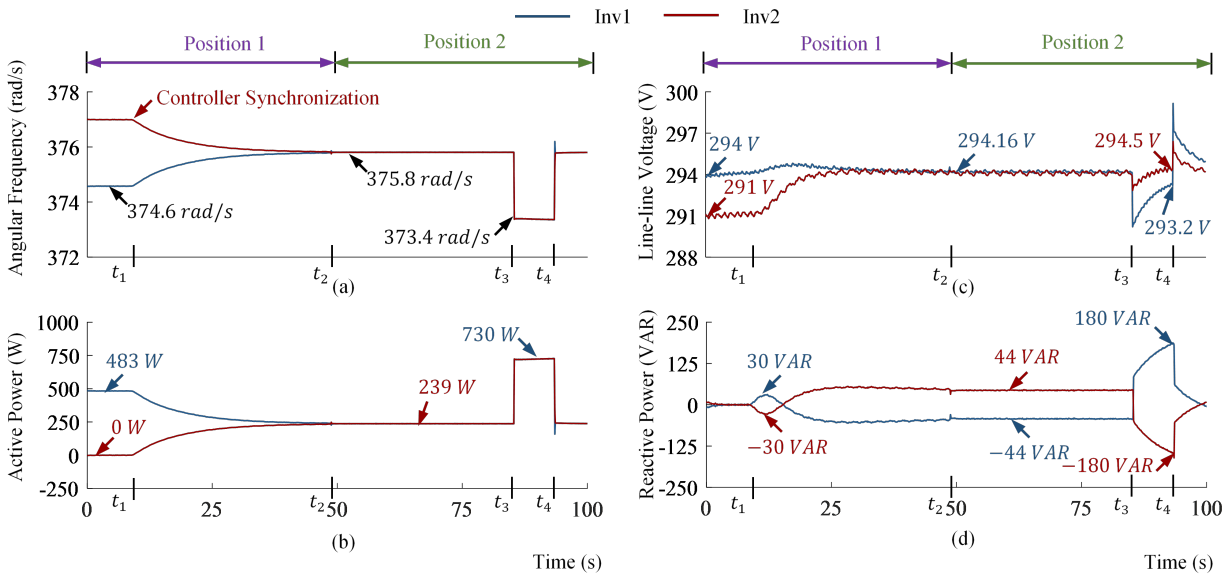

Figure 2.13: *Experimental verification of the controller-sync method with droop control for power-sharing; (a) angular frequency of the system and of the GFM control path of Inv2, (b) active power injected by the two inverters, (c) line-line voltage amplitudes at the PCC, and (d) reactive power contribution by Inv1 and Inv2.*

This test proves that the controller-sync method can establish seamless synchronization and power-sharing of GFM inverters.

Fig. 2.14 shows the performance of the controller-sync method in synchronization and power-sharing using virtual inertia-based control. The initial and the additional load are exactly same as in the droop-based controller, see Fig. 2.13(b). The frequency plot in Fig. 2.14(a) shows less deviation from the nominal values than the deviation from the droop controller. However, depending on the damping coefficient, the controller synchronization time is comparatively longer. There may exist visible transients in active and reactive power injections if the synchronization is not completed in time and the switches are moved to position 2, see Fig. 2.14(b) and Fig. 2.14(d).On the contrary, reducing the damping coefficient may reduce the time for synchronization, but increase the oscillation in the system. The PCC voltage amplitudes is regulated around the nominal voltage in both switch positions, as shown in Fig. 2.14(c). This test proves that the developed controller-sync method is also applicable with the virtual inertia based power-sharing.

Fig. 2.15 shows a picture during the data acquisition of Fig.2.12 for experimental verifi-

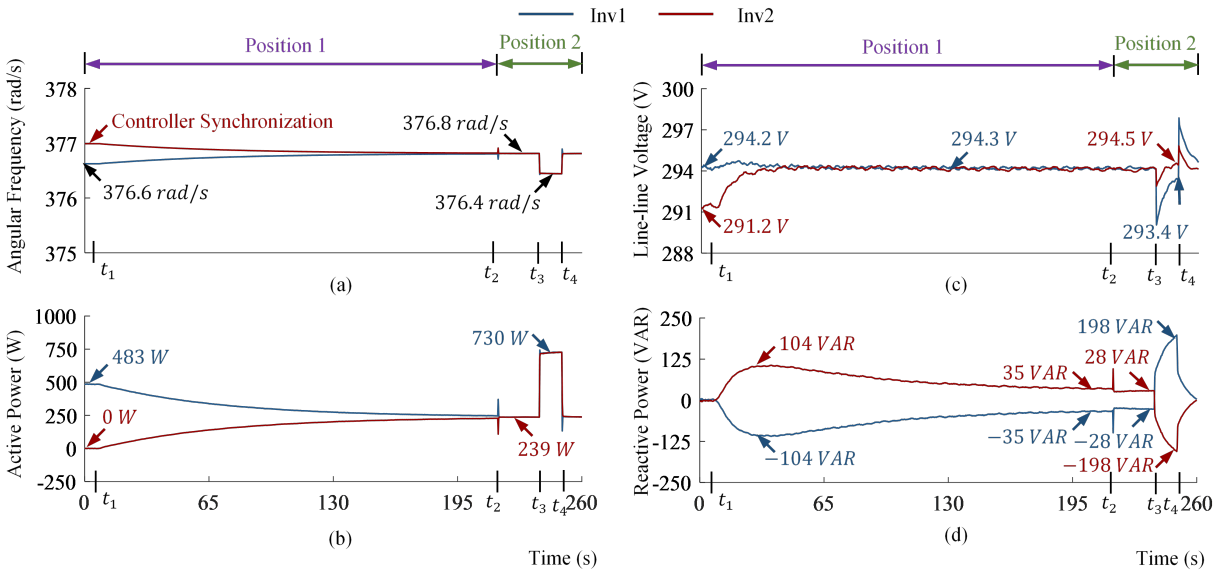

Figure 2.14: *Experimental verification of the controller-sync method with virtual inertia-based power-sharing; (a) angular frequency of the system and of the GFM control path of Inv*2*, (b) active power injected by the two inverters, (c) line-line voltage amplitudes at the PCC, and (d) reactive power contribution by Inv*1 *and Inv*2*.*

cation of the controller-sync method.

2.5.4 Comparison between the Two Methods

Experimental results in Subsection 2.5.3 prove that both methods, i.e., output-sync and controller-sync method, can perform seamless synchronization for the GFM inverters. In addition, the efficacy of the two methods are verified with droop-based and virtual inertia-based power-sharing controls. While both methods are effective, the two methods have some differences, which will be discussed in this subsection.

- **Number of sensors:** The output-sync method requires two sets of voltage sensors at the two sided of the circuit breaker for voltage and frequency synchronization. Whereas, the controller-sync method needs only one set of voltage sensors as the circuit breaker remains connected.

- **Standby mode:** The inverter can remain connected to the system without injecting any active or reactive power with the controller-sync method. This keeps the inverter

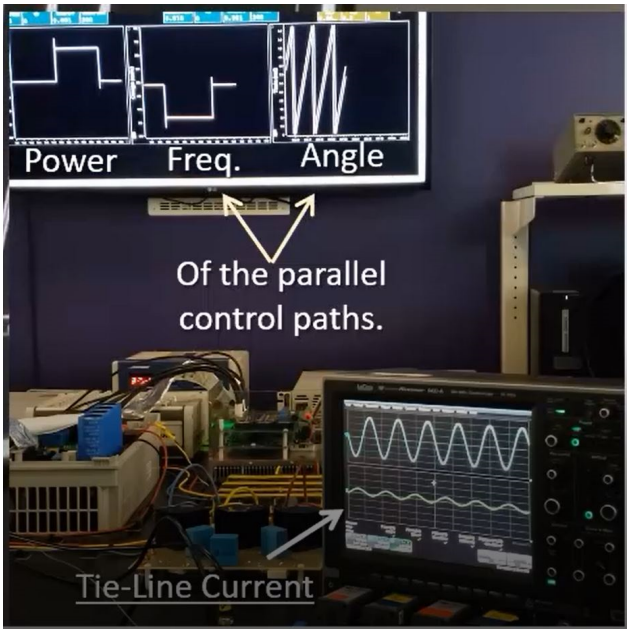

Figure 2.15: *Experimental verification of the controller-sync method.*

in stand-by position. Output-sync method does not provide this capability.

- **Number of PI controllers:** The output-sync method has only three PI controllers, whereas, the controller-sync method has six PI controllers. Therefore, parameter tuning in controller-sync method requires more computation.

- **Power-sharing:** In output-sync method, power-sharing is performed after the switch positions are set for GFM mode, i.e., position 2. On the contrary, the controller-sync method can perform power-sharing in both position 1 and 2.

- **Black-start ability:** The controller-sync method requires the microgrid frequency to perform black-start. Whereas, with the output-sync method, the inverters can independently black-start.

- **Grid-connected and islanded operation:** The controller-sync method can be used to operate an inverter in both GFM and GFL mode. The output-sync method can only be operated in GFM mode.

2.6 Conclusion

In this chapter, two methods for inverter synchronization in GFM mode, named output-sync and controller-sync method, have been analyzed and experimentally verified. In addition, state-space modeling for the controller-sync has been derived and stability of the controller under different parameter load has been investigated. The summary of the findings is as follows.

- Both synchronization method have been able to seamlessly synchronize with the microgrid. The inverters do not need to transit to GFL mode after synchronization.
- The output-sync method has used two PI blocks, whereas, the controller-sync method has used six PI blocks. Furthermore, the controller-sync method has required less number of sensors.
- The controller-sync method has been able to stat connected to a system without injecting any power, which is a unique characteristics.
- State-space analysis under different loads has shown the the controller-sync method stays in the stable region.
- Both synchronization methods have shown power-sharing capability with droop and virtual inertia.

Chapter 3

Phase-Angle Detection for Inverters in Asymmetrical Grid

In this chapter, a signal reformation-based direct phase-angle detection (DPD-SR) technique is developed for the inverters to provide an enhanced operation capability under asymmetrical conditions. Unbalanced load in the grid may cause voltage amplitude and phase-angle asymmetries at the terminals of the inverters, resulting in erroneous phase-angle detection. The developed DPD-SR technique can rapidly and accurately detect the phase-angles under asymmetrical conditions by utilizing a novel signal reformation technique. Some unique features of the developed DPD-SR technique are, it requires only two line-line voltages, it can perform equally under symmetrical and asymmetrical conditions, and it does not require any closed-loop controller like PLLs. The DPD-SR method developed in this chapter is used in all the inverter controllers presented in this dissertation.

Discussions on the direct phase-angle detection (DPD) technique [121], the conventional SRF-PLL [122], and the advanced DDSRF-PLL [108] is presented and their performances are compared under symmetrical and asymmetrical conditions in Section 3.1. Section 3.2 presents the detailed mathematical formulation and algorithm of the developed signal reformation based direct phase-angle detection (DPD-SR) technique. The experimental results comparing the performance of the developed DPD-SR technique with the conventional SRF-

PLL and DDSRF-PLL are presented in Section 3.3. Section 3.4 presents the conclusions of this chapter.

3.1 The DPD Technique, SRF-PLL and DDSRF-PLL for Phase-Angle Estimation

In this section, performance of the DPD technique, the SRF-PLL and the DDSRF-PLL is compared under both symmetrical and asymmetrical conditions of the grid. The DPD technique [121], on which the DPD-SR is developed, is described in details through mathematical formulation and phasor diagram in Subsection 3.1.1. Subsection 3.1.2 highlights the structure of the conventional SRF-PLL and the DDSRF-PLL. Finally, the performance of the DPD technique, SRF-PLL and DDSRF-PLL under symmetrical and asymmetrical grid conditions are investigated in Subsection 3.1.3.

3.1.1 Formulation of the DPD Technique

The DPD technique uses trigonometric function to directly calculate the phase-angle of a three-phase system from two of the three line-line voltages. To formulate the controller, the two line-line voltage signals from a three-phase balance sinusoidal signal are considered as,

$$v_{ab}^{m} = V_{LL}cos(\theta_{ab}), \tag{3.1}$$

and

$$v_{bc}^{m} = V_{LL}cos\left(\theta_{ab} - \frac{2\pi}{3}\right). \tag{3.2}$$

Here, v_{ab}^{m} and v_{bc}^{m} are two line-line voltages, V_{LL} is the amplitude of the voltages and θ_{ab} is the phase-angle of v_{ab}^{m}. Notice that, the phase-angle, θ_{ab}, is the unknown parameter which needs to be detected. Now, expanding (3.2) gives

$$v_{bc}^{m} = -\frac{1}{2}V_{LL}cos(\theta_{ab}) + \frac{\sqrt{3}}{2}V_{LL}sin(\theta_{ab}). \tag{3.3}$$

Dividing (3.3) by (3.1) yields,

$$\frac{v_{bc}^m}{v_{ab}^m} = -\frac{1}{2} + \frac{\sqrt{3}}{2} tan(\theta_{ab}), \tag{3.4}$$

which can be rearranged as,

$$\theta_{ab} = tan^{-1}\left(\frac{v_{ab}^m + 2v_{bc}^m}{\sqrt{3}v_{ab}^m}\right). \tag{3.5}$$

Thus, θ_{ab} can be calculated using (3.5) if the line-line voltages, v_{ab}^m and v_{bc}^m, are measured. Notice that, θ_{ab}, from (3.5) is calculated using the four-quadrant inverse tangent method to determine the ranges within $-\pi/2$ to $-\pi/2$, which is commonly used in computer programming. The phase-angle is adjusted within the range from 0 to 2π by adding an angle of 2π if (3.5) is negative.

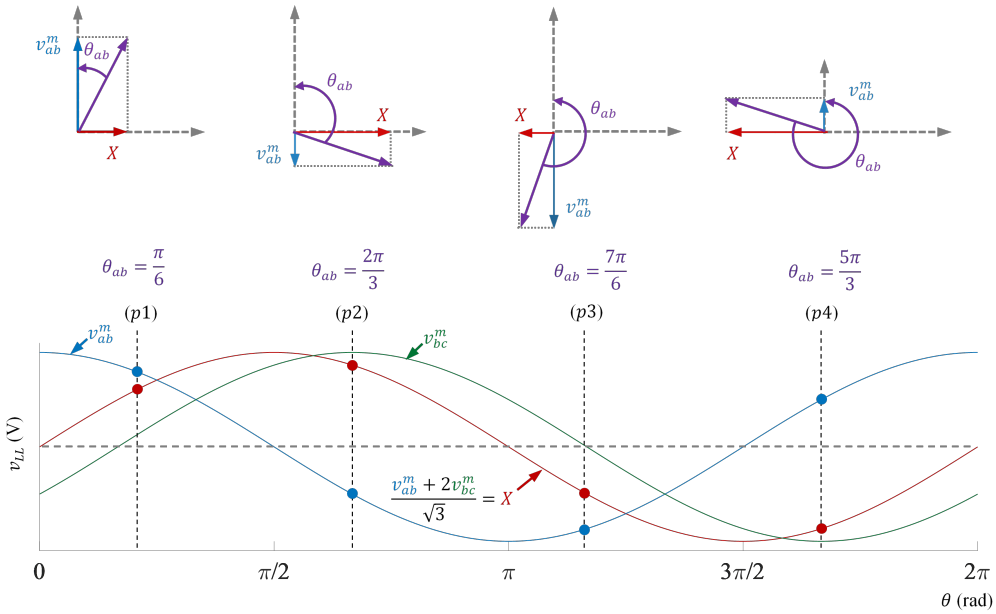

Figure 3.1: *Visual representation of the four-quadrant inverse tangent formula where the phase-angle, θ_{ab}, ranges from (p1) $0 \leq \theta_{ab} < \pi/2$, (p2) $\pi/2 \leq \theta_{ab} < \pi$, (p3) $\pi \leq \theta_{ab} < 3\pi/2$, and (p4) $3\pi/2 \leq \theta_{ab} < 2\pi$.*

A graphical visualization of calculating the phase-angle, θ_{ab}, for DPD technique is shown in Fig. 3.1, where the numerator and the denominator values at the four points on the

Table 3.1: *Sample Calculation for Four-Quadrant Inverse Tangent Formula*

Position	v_{ab}^m	$-\sqrt{3}v_c^m$	$tan^{-1}\left(\frac{X}{v_{ab}^m}\right)$	Adjustment	θ_{ab}
(p1)	0.87	0.5	$\pi/6$	0	$\pi/6$
(p2)	-0.5	0.87	$2\pi/3$	0	$2\pi/3$
(p3)	-0.87	-0.5	$-5\pi/6$	2π	$7\pi/6$
(p4)	0.5	-0.87	$-\pi/3$	2π	$5\pi/6$

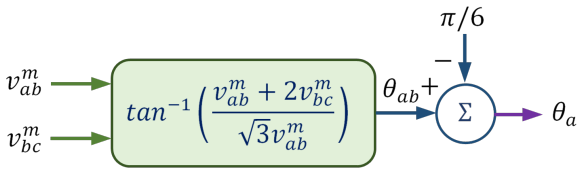

Figure 3.2: *Block diagram of the direct phase-angle detection (DPD) technique.*

sinusoidal signal, $p(1)-p(4)$, are represented by the vectors on the four quadrants. Table 3.1 shows the phase-angle estimation for the four points, i.e., $(p1)-(p4)$, with (3.5). Notice that, in DPD technique, only two instantaneous voltage measurements are needed and the estimation is simple and straightforward. The frequency of the voltage can be obtained by differentiating the phase-angle with respect to time. Fig. 3.2 shows the block diagram of the DPD technique. Notice that the phase-angle of the phase voltage can simply be obtained by subtracting $\pi/6$ from θ_{ab}, i.e., $\theta_a = \theta_{ab} - \pi/6$.

3.1.2 SRF-PLL and DDSRF-PLL

SRF-PLL utilizes three-phase phase voltages to measure the phase-angle. The task is performed by transforming the three-phase voltages to qd-frame of reference, and forcing the d-axis voltage component to converge to zero with a PI controller. Fig. 3.3 shows a block diagram of the SRF-PLL. Notice that the PI of the SRF-PLL generates a frequency reference, which is integrated to obtain the phase-angle, θ_a of the first phase, i.e., v_a. An initial value, ω_n, is added to the output of the PI for faster response. In this method, the obtained θ_a is fed back to the abc to qd [119] block and eventually forces v_d to be zero. Therefore, phase-A of the three-phase voltage can be considered locked with the q-axis. Since SRF-PLL uses

closed-loop with a PI for regulation, the dynamic response of the PLL is sensitive to the controller gain parameters, i.e., control parameters tuned for one frequency may not provide same performance under a different frequency. Hence, oscillations in the SRF-PLL response can happen after any change in the three-phase voltages [50].

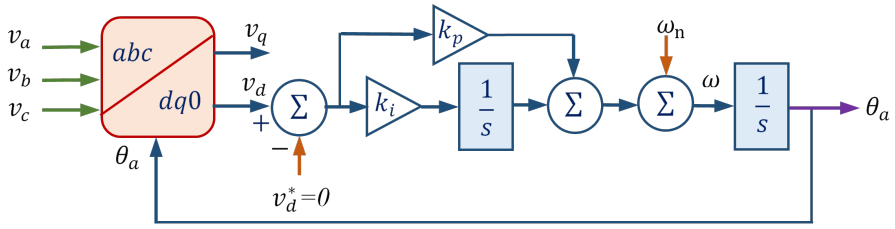

Figure 3.3: *Block diagram of the conventional SRF-PLL.*

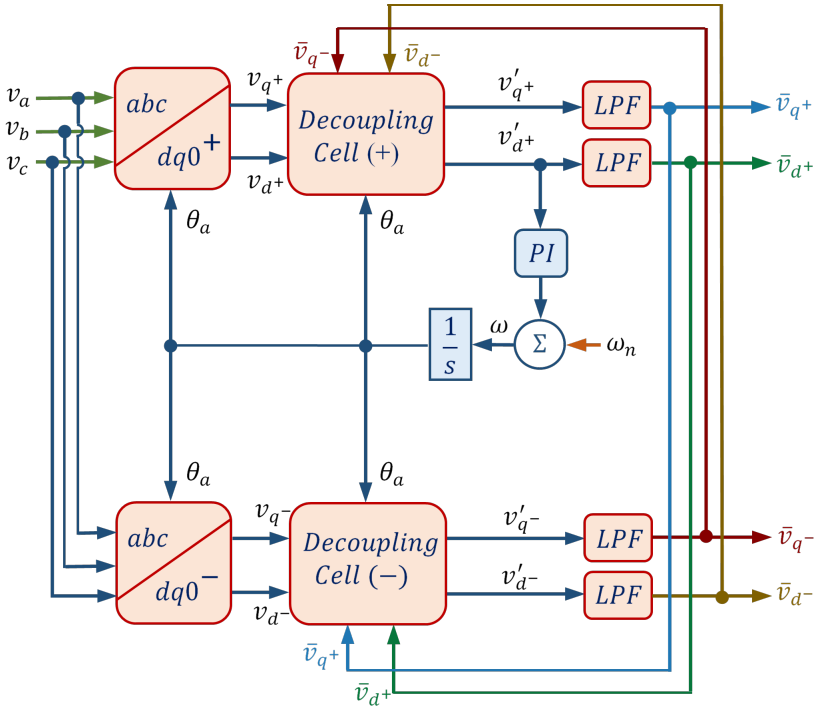

Figure 3.4: *Block diagram of the DDSRF-PLL.*

The DDSRF-PLL method significantly improves the performance of the classical SRF-PLL technique [108]. The decoupled double SRF (DDSRF)-PLL generates the *dq*-axis components for the positive and the negative sequence with two separate *abc* to *dq* transformation blocks. Then, the *dq*-axis components are decoupled through two decoupling cells and the

outputs are filtered. A closed-loop PI controller is used to regulate the d-axis components to zero and calculate the frequency and the phase-angle. Fig. 3.4 shows the block diagram of the DDSRF-PLL. Here, the decoupling cells are used to nullify the oscillations in v_{q^+}, v_{d^+}, v_{q^-}, and v_{d^-}, which is caused by asymmetrical voltages in the grid. Therefore, DDSRF-PLL is able to estimate the phase-angle of a distorted asymmetrical three-phase system and overcome the drawbacks of the classical PLLs. On the contrary, the frequency measurement by the DDSRF-PLL can be significantly oscillatory under asymmetrical phase-angle conditions [123]. Furthermore, with two SRF blocks, two decoupling cells, four high order filters, and onc PI loop, the PLL structure becomes complex, adding excessive computational burden.

3.1.3 Performances under Asymmetrical Conditions

The DPD technique presented in Subsection 3.1.1, and the SRF and DDSRF-PLL presented in Subsection 3.1.2 can correctly estimate the phase-angle of a three-phase system when the system is symmetrical. On the contrary, when the three-phase system is asymmetrical, i.e., unequal amplitudes of the phases or uneven phase-angle differences between the phases, the phase-angle estimations by the DPD technique and the SRF-PLL become inaccurate. Only an advanced PLL, e.g., the DDSRF-PLL can operate accurately under such circumstances. Fig. 3.5 shows the simulation results for the DPD technique, SRF-PLL and DDSRF-PLL, where the line-line voltages, the estimated phase-angle, and the frequency determined by the three methods are presented in Figs. 3.5(a)-(c). The three-phase 120 V, 60 Hz system is symmetrical from 0 to 0.05 *seconds*. Then the system is made asymmetrical by changing the amplitudes of v_{ab}, v_{bc}, and v_{ca} to 80%, 120%, and 50%, respectively of their actual values. Assuming θ_{ab} as the base of angle calculation, i.e., $\theta_{ab} = 0$, θ_{bc} and θ_{ca} become 140° and 90°, respectively. As observed in Fig. 3.5, the phase-angle and frequency measurements from the DPD and SRF-PLL are completely erroneous. Even though, with a very complicated structure and precise tuning of parameters, the estimation of the DDSRF-PLL is seemingly accurate, the estimation is delayed due to higher order filters in the controller, introducing an unknown amount of phase-shift. Furthermore, a 37% of frequency undershoot is noticed when

the system becomes asymmetrical. Therefore, a simple but accurate phase-angle estimation method, named signal reformation-based direct phase-angle detection (DPD-SR) method is developed in this dissertation. The developed technique utilizes a novel signal reformation method and combine it with the DPD technique presented in Subsection 3.1.2 to provide a simple and fast phase-angle detection approach.

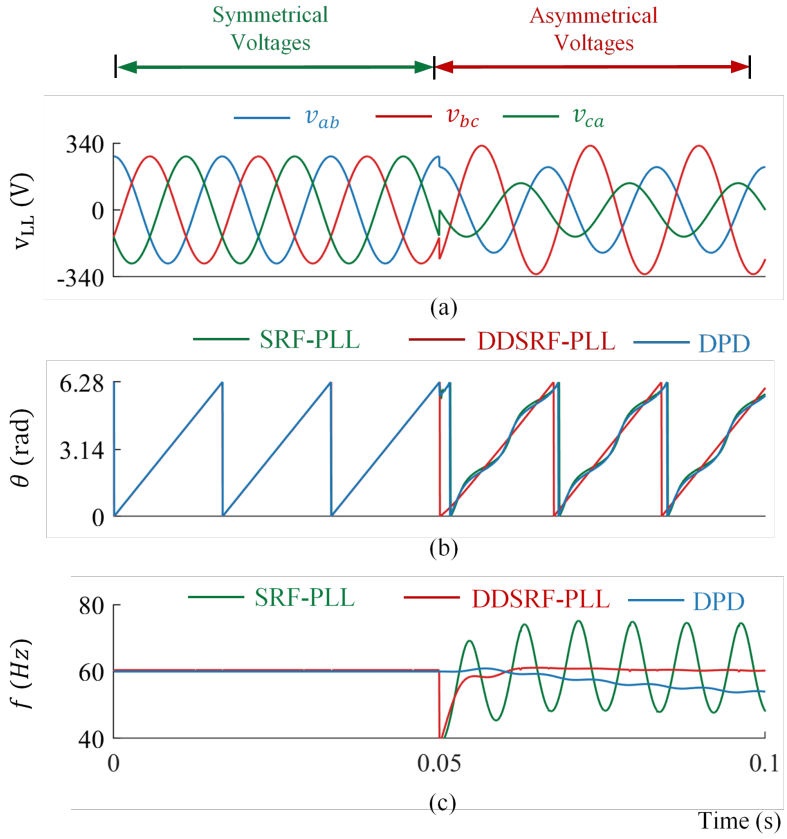

Figure 3.5: *Performance of SRF-PLL, DDSRF-PLL, and DPD technique under symmetrical and asymmetrical grid conditions; (a) measured three-phase voltage, (b) phase-angle and, (c) frequency measurements by the methods.*

3.2 Formulation of the DPD-SR Technique

The DPD-SR technique developed in this dissertation enables an inverter to operate under asymmetrical grid-conditions by providing accurate phase-angle measurements. The task is accomplished by combining the DPD technique presented in Subsection 3.1.2 with a novel sig-

nal reformation technique. The signal reformation technique measures the line-line voltages, and convert them to a three-phase symmetrical voltage using the developed mathematical formula when the voltages are asymmetrical. Then the reformed symmetrical voltages are fed to the DPD technique for phase-angle estimation. Therefore, the complete phase-angle estimation process is named as the DPD-SR technique in this dissertation. Notice that, the signal reformation technique accomplishes the same objective as the *dq* positive and negative sequence decoupling cells in DDSRF-PLL presented in Subsection 3.1.1. Interestingly, DPD-SR does not require any *abc* to *dq* transformation block or low-pass filters. Fig. 3.6 shows the block diagram of the developed DPD-SR technique, where the signal reformation block and the direct phase-angle detection block are cascaded, showing v_{ab} and v_{bc} as the input line-line voltages, and v_{ab}^{m} and v_{bc}^{m} as the reformed line-line voltages.

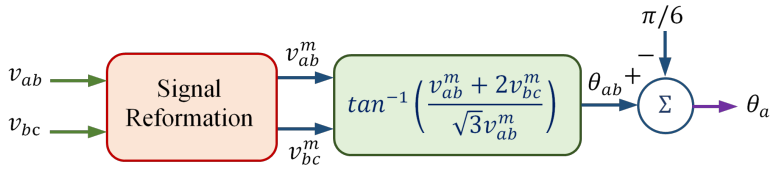

Figure 3.6: *Simplified block diagram of the DPD-SR technique.*

The operation of the signal reformation technique can be divided into two stages. In the first stage, two line-line voltages, v_{ab} and v_{bc}, are measured. Considering v_{ab}, the voltage between Phase-A and Phase-B as reference, the line-line voltages of a three-phase asymmetrical system can be expressed as

$$\begin{cases} v_{ab} = V_{LL}cos\left(\theta_{ab}\right), \\ v_{bc} = k_1 V_{LL}cos\left(\theta_{ab} - (2\pi/3 + \Delta\theta_1)\right), \\ v_{ca} = k_2 V_{LL}cos\left(\theta_{ab} + (2\pi/3 + \Delta\theta_2)\right), \end{cases} \tag{3.6}$$

where, V_{ab}, V_{bc}, and V_{ca} are the three line-line voltages with nominal amplitude, V_{LL}. The amplitude deviations of V_{ab} and V_{bc} are denoted by the two positive multiplier parameters, k_1 and k_2, respectively. Similarly, $\Delta\theta_1$ and $\Delta\theta_2$ are the phase-angle deviations from symmetrical

three-phase voltages. The objective of the signal reformation technique is to convert (3.6) to

$$\begin{cases} v_{ab}^{m} = V_{LL} cos\left(\theta_{ab}\right), \\ v_{bc}^{m} = V_{LL} cos\left(\theta_{ab} - 2\pi/3\right), \\ v_{ca}^{m} = V_{LL} cos\left(\theta_{ab} + 2\pi/3\right). \end{cases} \tag{3.7}$$

where, v_{ab}^{m}, v_{bc}^{m}, and v_{ca}^{m} are the reformed normalized voltages. Notice that $V_L L$, k_1, k_2, $\Delta\theta_1$, and $\Delta\theta_2$ in (3.6) are the unknown parameters.

The signal reformation technique only measures V_{ab} and V_{bc}. The $V_L L$ is measured and periodically updated by monitoring the amplitude of V_{ab} at every half-cycle, i.e., $V_{LL} = |v_{ab}|$. Similarly, the amplitude of V_{ab} is measured and updated at every half-cycle. Then, k_1 can be obtained from,

$$k_1 = \frac{|v_{bc}|}{V_{LL}}. \tag{3.8}$$

The expression of v_{bc} in (3.6) can be rearranged as,

$$\theta_{ab} - \frac{2\pi}{3} - \Delta\theta_1 = -cos^{-1}\left(\frac{v_{bc}}{k_1 V_{LL}}\right) \tag{3.9}$$

Notice that, the phase-angle of v_{bc} resides in the second quadrant. Therefore, a negative term is applied for the inverse of the cosine term in (3.9). The developed method identifies the positive-to-negative zero crossing of v_{ab}, where $\theta_{ab} = \pi/2$ and the phase-angle deviation, $\Delta\theta_1$, can be obtained from,

$$\Delta\theta_1 = -\frac{\pi}{6} + cos^{-1}\left(\frac{v_{bc}}{k_1 V_{LL}}\right). \tag{3.10}$$

The phase-angle deviation calculated from (3.10) may contain error due to discrete sampling. The error can be adjusted from, V_{ab0}, the amplitude of V_{ab} immediately after the zero crossing. Then, the error in phase-angle deviation calculation is $sin^{-1}\left(v_{ab0}\right)$, and the error adjusted

phase-angle deviation is calculated from

$$\Delta\theta_1 = -\frac{\pi}{6} + cos^{-1}\left(\frac{v_{bc}}{k_1 V_{LL}}\right) - sin^{-1}\left(v_{ab0}\right). \tag{3.11}$$

Fig. 3.7 shows a graphical demonstration for $\Delta\theta_1$ estimation.

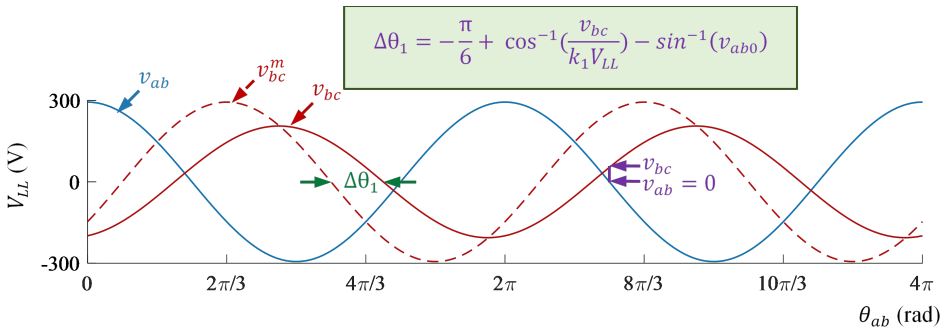

Figure 3.7: $\Delta\theta_1$ *estimation from the voltage waveforms*

In the second stage of the developed method, a reformed signal is produced utilizing voltage measurements and the phase-angle deviation estimated in the first stage, i.e., v_{bc}^m is developed from the expression of v_{bc}, utilizing $\Delta\theta_1$. From (3.6), v_{bc} can be expressed as,

$$v_{bc} = k_1 V_{LL} cos\left(\theta_{ab} - \frac{2\pi}{3}\right) cos(\Delta\theta_1) + k_1 V_{LL} sin\left(\theta_{ab} - \frac{2\pi}{3}\right) sin(\Delta\theta_1). \tag{3.12}$$

Substituting, $cos\left(\theta_{ab} - \frac{2\pi}{3}\right)$ by v_{bc}^m and $sin\left(\theta_{ab} - \frac{2\pi}{3}\right)$ by $\sqrt{1 - (v_{bc}^m)^2}$ in (3.12) yield

$$v_{bc} = k_1 V_{LL} v_{bc}^m cos\left(\Delta\theta_1\right) + k_1 V_{LL}\sqrt{1 - (v_{bc}^m)^2} sin\left(\Delta\theta_1\right), \tag{3.13}$$

which can be rearranged in a form of quadratic equation of v_{bc}^m as follows,

$$(v_{bc}^m)^2 - \frac{2v_{bc}}{k_1 V_{LL}}\left(v_{bc}^m\right) cos\left(\Delta\theta_1\right) = sin^2\left(\Delta\theta_1\right) - \left(\frac{v_{bc}}{k_1 V_{LL}}\right)^2. \tag{3.14}$$

Solving (3.14) for v_{ab}^m yields

$$v_{bc}^m = \frac{v_{bc}}{k_1 V_{LL}} cos\,(\Delta\theta_1) \pm sin\,(\Delta\theta_1)\sqrt{1-\left(\frac{v_{bc}}{k_1 V_{LL}}\right)^2}. \tag{3.15}$$

Notice that (3.15) has two solutions, whereas only one of the solutions is valid at an instance. Fig. 3.8 shows the plots of the two solutions, along with the appropriate solution when $\Delta\theta_1 = 30°$. It is observed from Fig. 3.8 that the solution periodically swings from one solution to another. Therefore, an algorithm to select the appropriate solution for all instances is developed.

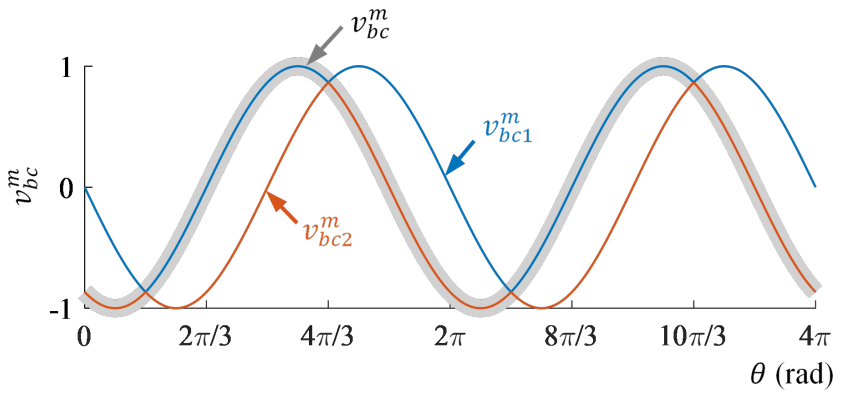

Figure 3.8: *All solutions of* (3.15) *for* $\Delta\theta_1 = 30°$, v_{bc1}^m *and* v_{bc2}^m, *and the desired solution,* v_{bc}^m.

In order to identify the proper solution at any instance, a flag is defined as follows.

$$v_{bc}^m = \begin{cases} v_{bc1}^m & if\ Flag = 0 \\ v_{bc2}^m & if\ Flag = 1 \end{cases} \tag{3.16}$$

The algorithm to change the flag values between 0 and 1 is presented as the flow chart in Fig 3.9. Notice in Fig. 3.8 that, at the intersecting points of the two solutions, the acceptable solution switch from one to another. In the developed algorithm, the flag value is updated only when the conditions, $|v_{bc1}^m - v_{bc2}^m| < \varepsilon$, where ε is a small predefined threshold, and $v_{bc1}^m v_{bc2}^m > 0$, are simultaneously satisfied. When the two conditions are met, flag is set to 1 if

$v_{bc1}^m > 0$, and to 0 otherwise. Thus, v_{bc}^m is obtained. Simultaneously, v_{ab}^m is directly calculated by dividing the reference voltage, v_{ab} by the measured line-line voltage amplitude, V_{LL}, i.e., $v_{ab}^m = v_{ab}/V_{LL}$. It is better to mention that, the developed algorithm does not depend on the sign and value of $\Delta\theta_1$. Nevertheless, high-frequency harmonics and noises may introduce error and must be filtered out during the measurement stage.

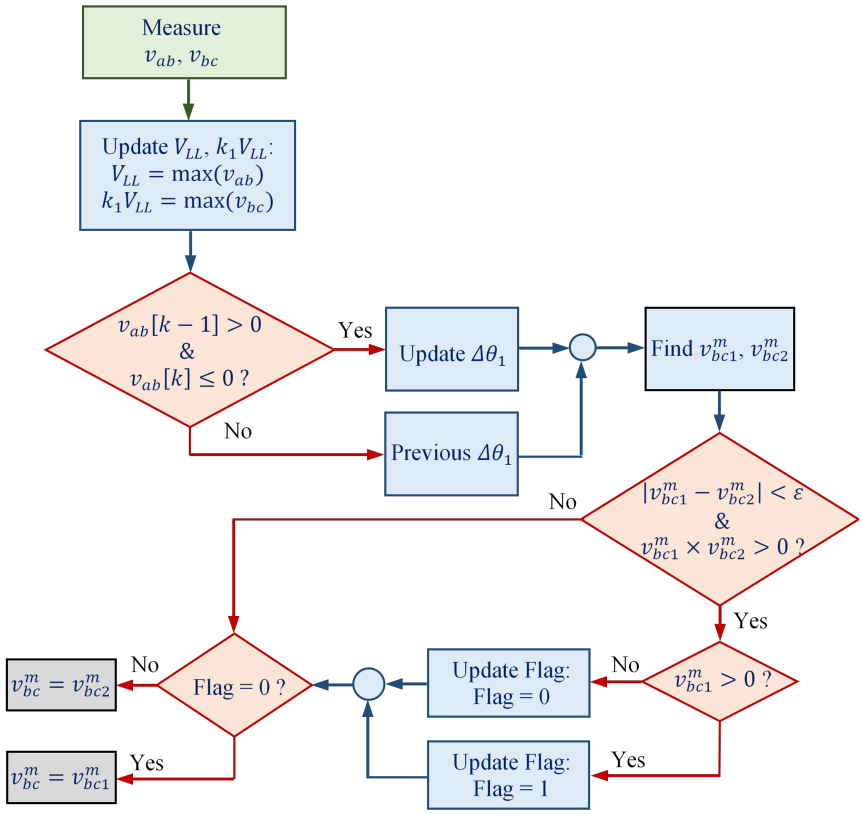

Figure 3.9: *Flow chart showing the algorithm for v_{bc}^m calculation.*

Unlike the PLL methods, DPD-SR technique directly produce the phase-angle instead of integrating the frequency. To obtain the frequency from the developed DPD-SR technique, an additional estimation block consists of a derivative, a filter and a rate-limiter can be used. Fig. 3.10 shows the block diagram for frequency estimation. Differentiating θ_{ab} with respect to time would have resulted in spikes in the estimated frequency due to the discontinuous nature of the phase-angle. Therefore, the filter and the rate limiter block is designed to suppress the spikes in the frequency. Slew rate for rise and fall of signal can be set to the

highest rad/s^2 rate expected in the system. In addition, the $\frac{s}{(\tau s+1)}$ block combines the time derivative operator with a first-order low-pass filter, whose cut-off frequency is defined by $\omega_c = \frac{1}{\tau}$, where ω_c can be set to twice the systems frequency, i.e., 240π for $60Hz$ signal in this dissertation. It it mention worthy that the frequency estimation range of the developed DPD-SR technique is only limited by the parameters related to the hardware, i.e., processing speed, sensor bandwidths.

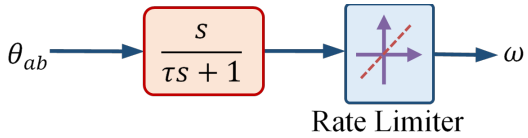

Figure 3.10: *Block diagram for frequency measurement from DPD-SR technique.*

3.3 Experimental Results

In this section, the performance of the developed DPD-SR technique is verified through hardware experiments. The performance of the conventional SRF-PLL and the advanced DDSRF-PLL is also tested for comparison. An asymmetrical power grid is created using the grid emulator. The dSPACE acquires the measurement signals, converts data to digital, and digitally filters the measurement noises and distortions. The developed controller is implemented into the controller to control a three-phase inverter in grid-connected mode under the asymmetrical conditions. All experiments are conducted by changing the amplitude of one phase voltage which simultaneously create amplitude phase-angle asymmetry. All data is captured through ControlDesk software and plotted using MATLAB. The following tests are investigated. All parameters used the developed DPD-SR technique, the SRF and the DDSRF-PLL are provided in Table 3.2. Parameters used for the GFL operation of the inverter are provided in Table 3.3. These parameters are included herein for the continuity and reproducibility of the work presented in this chapter.

Table 3.2: *Control Parameters for DPD-SR, SRF and DDSRF-PLL*

Parameters for DPD-SR	
Tolerance, ϵ	0.05
Slew rate of rate limiter	4000 $Hz/second$
Natural frequency of 1st order filter, f_c	120 Hz
Parameters for SRF and DDSRF-PLL.	
Closed loop proportional gain, k_p	2.22
Closed loop integral gain, k_i	246.7
Filter gain parameters, $k_D DSRF$	0.707

Table 3.3: *Circuit Parameters for Experiment with Inverter.*

Fundamental frequency, f	60 Hz
PWM switching frequency, f_{sw}	5 kHz
Line-line voltage, V_{LL}	208 V
DC bus voltage, V_{DC}	340 V
Filter inductance (Inverter side), L_1	1.0 mH
Filter inductance (Grid side), L_2	0.5 mH
Coupling capacitance (in Δ), C_f	30 μF

3.3.1 Phase-Angle Detection in Asymmetrical Grid

In this test scenario the developed DPS-SR technique for phase-angle estimation is compared with the SRF and DDSRF-PLL under asymmetrical grid conditions. For all three phase-angle estimation process, the amplitude of phase-C is reduced by 49.3%. This resulted in a 23.3% reduction in the amplitude for the line-line voltage between phase-B and phase-C, v_{bc}. Also, the phase-angle difference between v_{ab} and v_{bc} is increased to 130.7°, see Fig. 3.11(a) and Fig. 3.12(a). Fig. 3.11(b) shows the phase-angles estimated by the SRF-PLL and the DPD-SR under the asymmetrical conditions. Notice that the phase-angle estimation by the classical SRF-PLL is showing error with oscillation due to the asymmetrical grid. Fig. 3.12(b) shows that the DDSRF-PLL suppresses the oscillation, but adds delay in the estimation. On the other hand, the performance of the DPD-SR technique is superior under asymmetrical grid as it is accurate and does not introduce any delay.

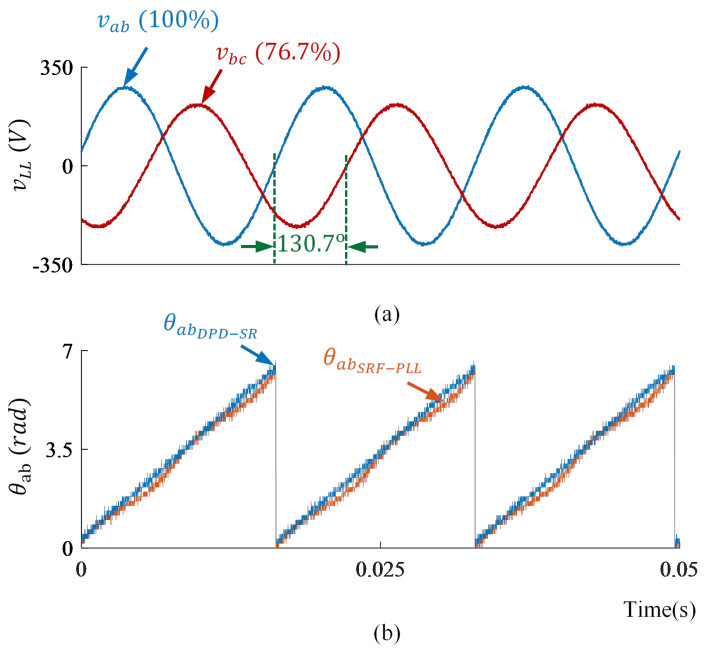

Figure 3.11: *Performance of the DPD-SR technique and the conventional SRF-PLL for phase-angle detection under asymmetrical grid; (a) Line-line voltages, (b) estimated phase-angles.*

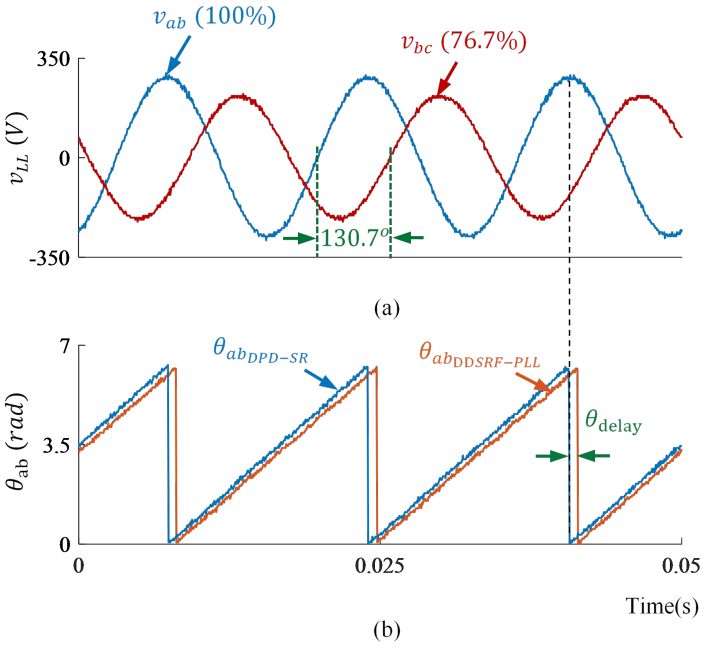

Figure 3.12: *Performance comparison of the DPD-SR technique and the DDSRF-PLL for phase-angle detection under asymmetrical grid; (a) Line-line voltages, (b) estimated phase-angles.*

3.3.2 Performance on Three-Phase Inverter Control under Asymmetrical Condition

In this set of experiments a grid-interactive inverter is controlled in GFL mode to inject 600 W of active power at unity power factor. The phase-angle reference provided to the PWM generator of the inverter is separately generated through the conventional SRF-PLL, the DDSRF-PLL, and the developed DPD-SR technique to operate the inverter in synchronization with the grid. The circuit and the operating parameters of the inverter is available in Table 3.3. For each test, the amplitude of the line-neutral voltage of phase-C is decreased by 15%. This reduced the amplitude of the line-line voltage between phase-A and phase-B, v_{bc} by 9.1% while v_{ab} remains unaffected. At the same time, the phase-angle difference between v_{ab} and v_{bc} is increased to 130°.

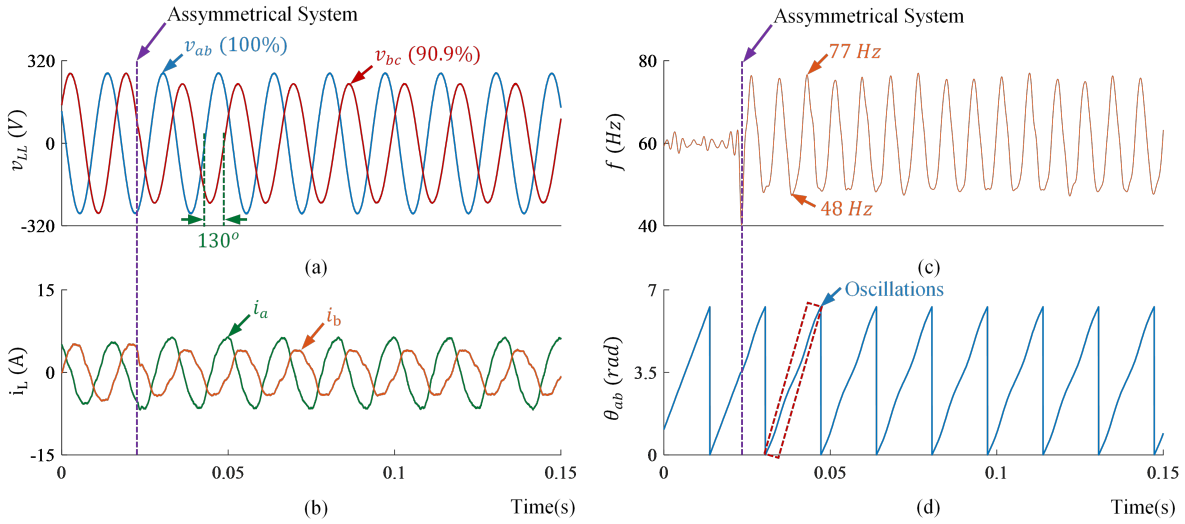

Figure 3.13: *Experiment result for inverter control by SRF-PLL in asymmetrical grid; (a) Line-line voltages, (b) line current, (c) frequency, and (b) phase-angle.*

Fig. 3.13 shows the line-line voltage, line-current, system frequency and the phase-angle reference generated by the SRF-PLL for the inverter. It is observed from Fig. 3.13(c) that, as the system becomes asymmetric, the frequency measurements by the SRF-PLL becomes significantly oscillatory under asymmetric grid. The phase-angle estimation is also showing oscillation, see Fig. 3.13(d). The same experiment is repeated with the DDSRF-PLL and the

results are shown in Fig. 3.14, and with the developed DPD-SR and the results are shown in Fig. 3.15. Both DDSRF-PLL and DPD-SR shows supreme performance and produce accurate phase-angle and frequency estimations. However, the DDSRF-PLL is highly complex compared to the simple structure of the developed DPD-SR technique.

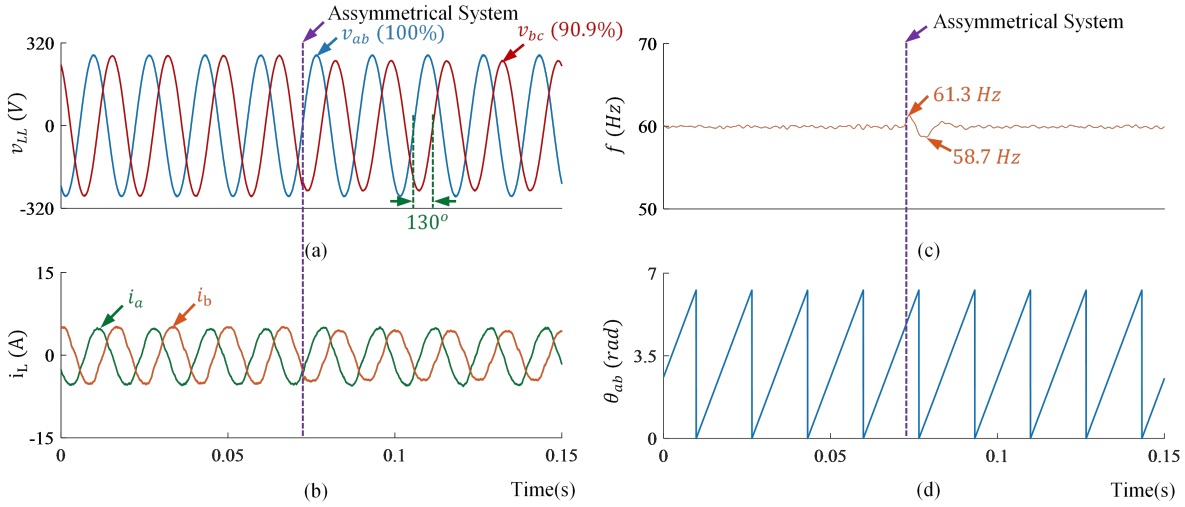

Figure 3.14: *Experiment result for inverter control by DDSRF-PLL in asymmetrical grid; (a) Line-line voltages, (b) line current, (c) frequency, and (b) phase-angle.*

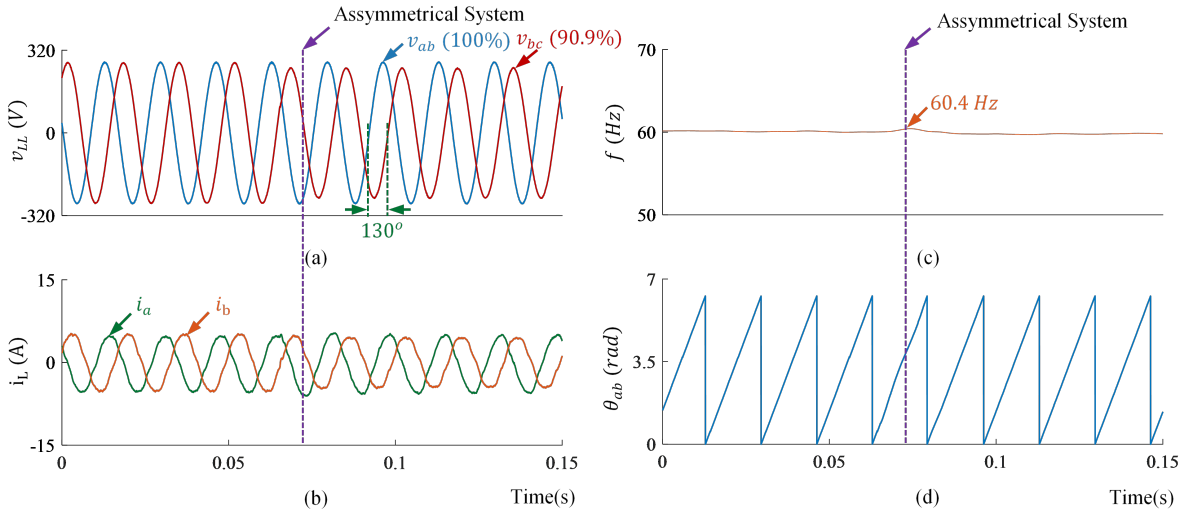

Figure 3.15: *Experiment result for inverter control by DPD-SR in asymmetrical grid; (a) Line-line voltages, (b) line current, (c) frequency, and (b) phase-angle.*

3.3.3 Impact of Harmonics on Phase-Angle Detection

In this test, the performance of the developed technique is compared with the DDSRF-PLL for a three-phase grid, of which all line-neutral voltages are polluted with 5% of the 5^{th} harmonic component. Furthermore, the voltage amplitude of phase-C, v_c is also reduced by 25% from its nominal value. A Y-connected three-phase load, of which each phase has a 70Ω resistor and a 2.5 mH inductor, is feed by the inverter and the grid. At first, the setup is tested for the symmetrical conditions and without any harmonics with the DPD-SR and DDSRF-PLL. Fig. 3.16 shows the estimated phase-angle and the frequency by the two methods. Notice that in Fig. 3.16(b), the phase-angle estimation by the developed DPD-SR and the DDSRF-PLL completely match with each other under symmetrical conditions. Also, both methods are able to properly track the system frequency, i.e., 60 Hz, see Fig. 3.16(c). Fig. 3.17 shows the estimated phase-angle and the frequency under asymmetry

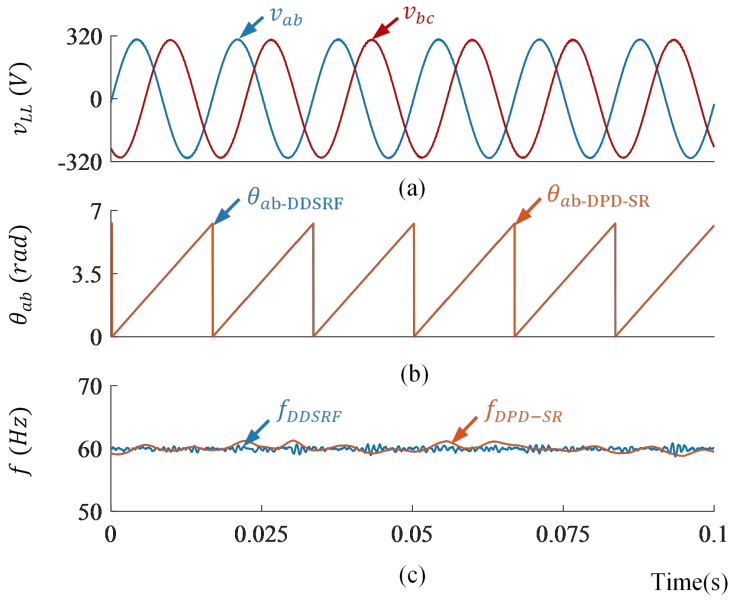

Figure 3.16: *Experiment result showing the (a) line-line voltage, (b) estimated phase-angle, and (c) frequency, by DPD-SR and DDSRF-PLL for symmetrical grid.*

and harmonics affected conditions. It is observed that both the developed DPD-SR technique and the advanced DDSRF-PLL method can accurately obtain the phase-angles under such conditions, see Fig. 3.16(b). However, compared to the developed DPD-SR technique,

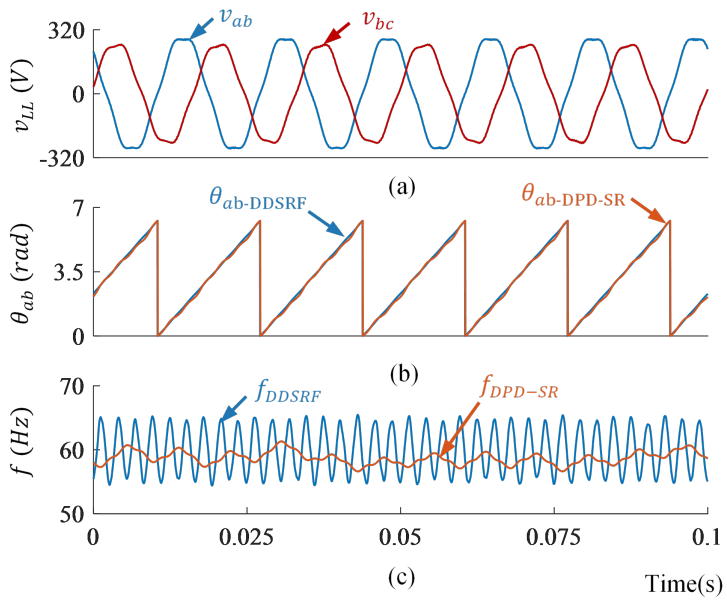

Figure 3.17: *Experiment result showing the (a) line-line voltage, (b) estimated phase-angle, and (c) frequency, by DPD-SR and DDSRF-PLL for* 5% *fifth harmonics affected asymmetrical grid.*

the frequency estimation of the DDSRF-PLL shows oscillatory due to the inclusion of the harmonics, see Fig. 3.16(b).

3.3.4 Performance Comparison of the DPD-SR with SRPLL and DDSRF-PLL

Figs. 3.18(a) and (b) show the side-by-side comparison of the Mean-Squared Error (MSE) of phase-angle estimation by SRF-PLL and DPD-SR, and DDSRF-PLL and DPD-SR respectively. Three scenarios, i.e., symmetrical, asymmetrical by making the amplitude of v_c reduced to 50%, and asymmetry with 5^{th} harmonic components, are investigated and their MSEs for phase-angel are plotted. Here, the error θ_{MSE} is calculated from $\theta_{MSE} = \frac{1}{n}(\theta_{meas.} - \theta_{act.})^2$, where $\theta_{meas.}$ and $\theta_{act.}$ are the measured and the actual phase-angles, respectively. It is see from Figs. 3.18 that, the performances of DDSRF-PLL and the developed DPD-SR method are far superior than the conventional SRF-PLL. Also, the developed DPD-SR performs almost equally as DDSRF-PLL, which has a very complex structure and difficult

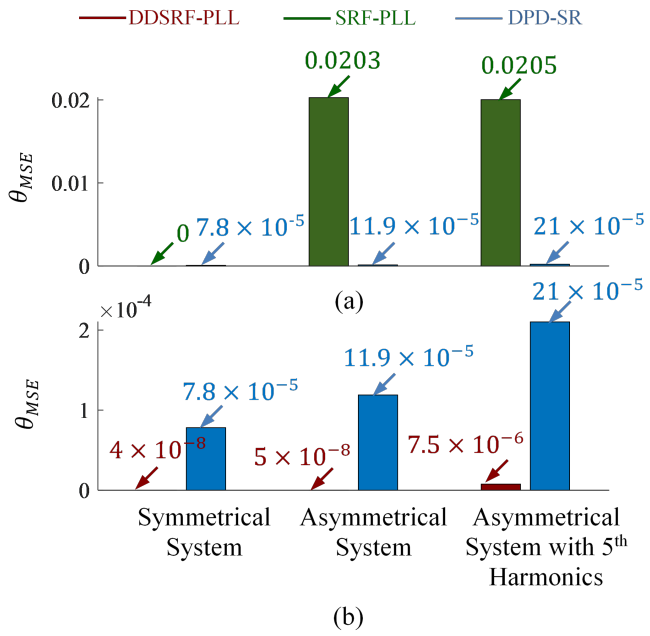

Figure 3.18: *Side-by-side comparison of θ_{MSE} for (a) SRF-PLL and DPD-SR, and (b) DDSRF-PLL and DPD-SR.*

to implement.

Also, the developed DPD-SR method is tested with the DDSRF-PLL under different conditions created by the grid emulator. The DDSRF-PLL has four built-in filters whose cut-off frequency gain parameter needs to be fine-tuned. The proportional gain parameter of the PI block of the DDSRF-PLL, $k_{DDSRF-PLL}$, is varied. Hence, three sets of values of $k_{DDSRF-PLL} = 0.3$, 0.707, and 1.4, are chosen for each test scenario. Fig. 3.19 shows the test results. The left column of Fig. 3.19 depicts the frequency tracking for a 2 Hz step change with a balanced and non-distorted grid. The middle column shows the same transient for voltage unbalance; whereas, the right column exhibits the results for unbalance and distorted grid conditions. In all cases, the dynamic performance of the DDSRF-PLL in terms of frequency tracking is highly sensitive to the tuning of $k_{DDSRF-PLL}$. Depending on the value of $k_{DDSRF-PLL}$, the DDSRF-PLL exhibits different overshoots and settling times. Conversely, the developed DPD-SR method offers an improved frequency tracking performance with respect to the DDSRF due to its lack of internal filters in the θ estimation path and simplicity. Furthermore, when the grid is unbalanced and distorted, the DDSRF presents an unsatisfac-

tory oscillatory frequency measurement, which can jeopardize the stability of any grid-tied converter.

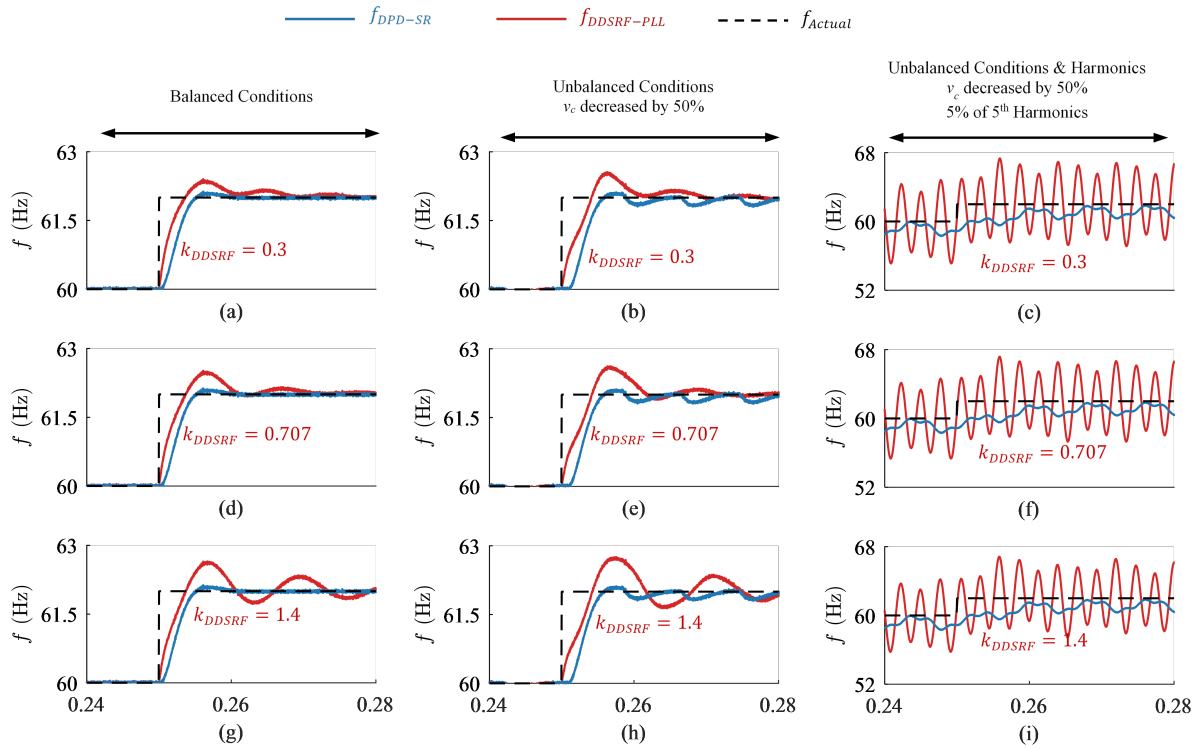

Figure 3.19: *Frequency response by the proposed DPD-SR and the DDSRF-PLL with different gain parameters during frequency jump from* 60 *Hz to* 62 *Hz under balanced condition, unbalanced condition, and unbalanced with harmonics affected condition. (a)* $k_{DDSRF-PLL} = 0.3$*, balanced, (b)* $k_{DDSRF-PLL} = 0.3$*,* v_c *drops to* 50%*, (c)* $k_{DDSRF-PLL} = 0.3$*,* v_c *drops to* 50%*,* 5% *of the* 5^th *harmonics, (d)* $k_{DDSRF-PLL} = 0.707$*, balanced, (e)* $k_{DDSRF-PLL} = 0.707$*,* v_c *drops to* 50%*, (f)* $k_{DDSRF-PLL} = 0.707$*,* v_c *drops to* 50%*,* 5% *of the* 5^th *harmonics, (g)* $k_{DDSRF-PLL} = 1.4$*, balanced, (h)* $k_{DDSRF-PLL} = 1.4$*,* v_c *drops to* 50%*, (i)* $k_{DDSRF-PLL} = 1.4$*,* v_c *drops to* 50%*,* 5% *of the* 5^th *harmonics.*

Based on the tests performed in this section, an overview of the comparison between the SRF-PLL, the DDSRF-PLL, and the developed DPD-SR technique is presented in Table 3.4. Fig. 3.20 shows a picture during the data acquisition of Fig.3.15 for experimental verification of the signal reformation-based direct phase-angle detection method.

Table 3.4: *Comparison between SRF-PLL, DDSRF-PLL, and DPD-SR.*

Factors	SRF-PLL	DDSRF-PLL	DPD-SR
Number of PI Loops	1	1	0
Number of SRF Blocks	1	2	0
Number of Decoupling Cells	0	2	0
Number of Filters	0	4	0
Signal Reformation Required	No	No	Yes
Mathematical Solution Required	No	No	Yes
Balanced Input Voltage	Accurate	Accurate	Accurate
Unbalanced Input Voltage	Inaccurate	Accurate	Accurate
Voltage Harmonics (5% THD)	Inaccurate	Limited	Limited

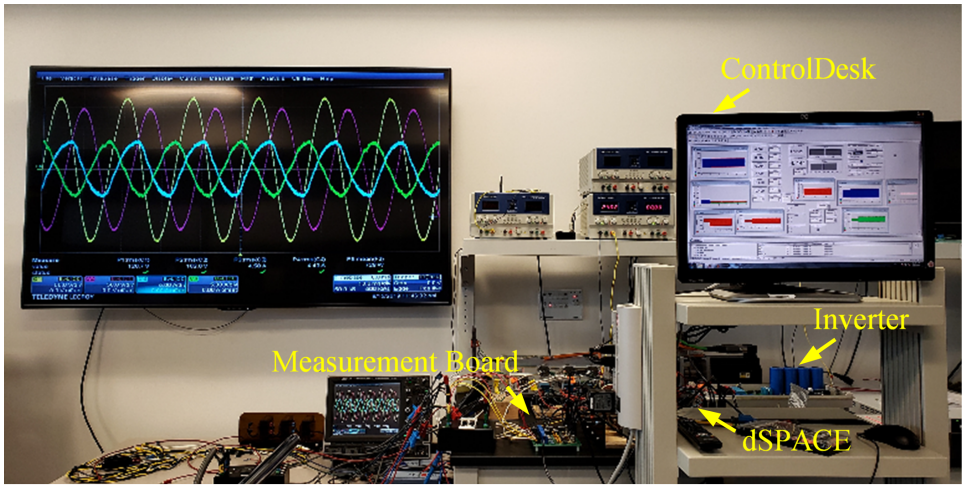

Figure 3.20: *Experimental verification of the DPD-SR method for phase-angle detection.*

3.4 Conclusion

In this chapter, a signal reformation-based direct phase-angle detection (DPD-SR) technique for inverters in asymmetrical grid has developed and verified through experiment results. The developed DPD-SR has been compared with the SRF-PLL and the DDSRF-PLL under asymmetrical and harmonics affected conditions. The findings of this chapter is summarized as follows.

- The developed method has been able to accurately estimate the phase-angle of the three-phase asymmetrical grid whereas the SRF-PLL cannot.
- Performance of the DPD-SR under asymmetrical conditions has been found as good as

the performance of the DDSRF-PLL, whereas, the structure of the DPD-SR has been made the simplest.

- The DPD-SR method has shown less sensor requirement, as only two line-line voltages have been sufficient.

- Although, the DPD-SR method have not been developed for frequency estimation, frequency can be obtained by using a filter with a rate-limiter block. In comparison with the performance of the DDSRF-PLL under 5% of the 5^{th} harmonics, the DPD-SR method has shown lower level of oscillations in estimating the frequency.

Chapter 4

Universal Controller for GFL and GFM Modes

In this chapter, a novel universal controller, that enables an inverter to operate in both GFL and GFM modes with the same control structure, is developed. The controller developed in this method is built upon the controller-sync method presented in Chapter 2. Phase-angle detection of the universal controller is performed using the DPD-SR technique developed in Chapter 3. With the developed universal controller, an incoming inverter is able to seamlessly sync with a grid or an islanded microgrid. The developed controller can autonomously and seamlessly switches its mode of operation to regulate the voltage and frequency in GFM mode and control the active and reactive power in GFL mode. Therefore, the the developed controller is named as the 'Universal Controller' in this dissertation.

Section 4.1 briefly describes the system in which the developed universal controller is studied. The synchronization operation, GFL operation, transition to GFM mode, and GFM operation of the controller is explained in details in Section 4.2. The stability of the controller in different modes is analyzed in Section 4.3. Section 4.4 demonstrates the performance of the controller through experimental results. Section 4.5 concludes and highlights the findings of this chapter.

4.1 System Configuration

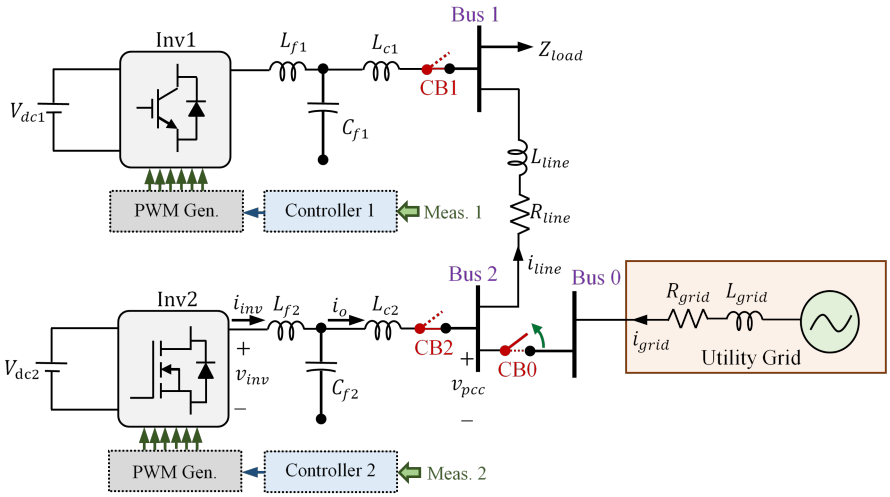

Figure 4.1: *Single-line block diagram of the system under study in Chapter 4*

.

In this section, the laboratory-scale system that is used for this work and the case-scenarios are briefly described. The system used in this chapter is exactly same as the system described in Fig. 2.1 in Chapter 2. Therefore, the system used in this chapter also consists of a microgrid with two grid-interactive inverters that can be connected to and disconnected from the utility grid. Also, each inverters has the same dc sources, LCL filters, circuit breakers, voltage and current sensors, control boards. The connected loads and the tie-line impedance are also same as in Chapter 2. In this chapter, the microgrid initially remains connected to the grid, see Fig. 4.1. Also, both $Inv1$ and $Inv2$ are programmed with the universal controller and can be considered as the incoming inverter to a grid or a microgrid. Furthermore, both inverters are capable of independently operating in GFL and GFM modes. Although the system presented in this chapter has only two inverters, the operation of the universal controller is not affected by the number of inverters.

Fig. 4.2 shows different microgrid conditions, under which the develop controller aims to provide smooth operation of each inverter. In grid-connected mode, both the inverters feed power to the local loads and the utility grid, see Fig. 4.2(a). The utility grid also contributes to power the local loads if the net generation of the inverters is less, see 4.2. The

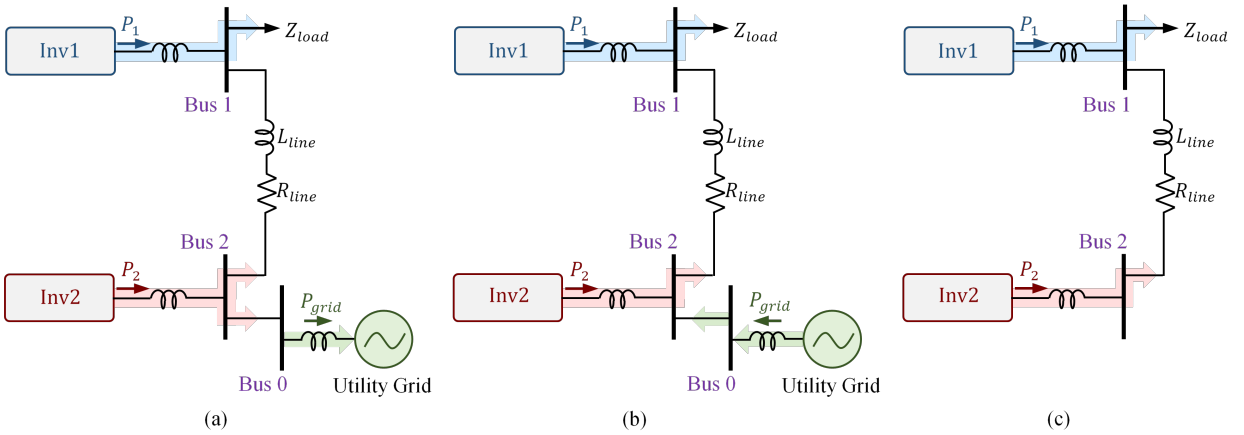

Figure 4.2: *Power flow in different modes of operation; (a) generation in microgrid is greater than the net load, (b) generation in microgrid is less than the net load, (c) generation in microgrid in islanded mode.*

microgrid can also operate in islanded mode where the grid is disconnected and the local loads are only fed by the inverters, see Fig. 4.2(c). Typically a 30% of the available active power is reserved in GFL operations to maintain sufficient reserve for ancillary services [13]. Therefore, in GFM mode, the inverter can feed an additional 30% of load. Furthermore, in an ideal microgrid, the peak load in the system in off-grid mode is expected to be less than the maximum power generation capacity of the inverters. Otherwise, load-shedding is performed in off-grid mode to reduce the total load below the total power capacity.

4.2 The Universal Controller for Inverters

In this section the detailed control philosophy of the developed universal controller is presented. Fig. 4.3 depicts the control block diagram of the developed controller. The developed controller consists of two sets of synchronized pair of parallel paths to build the frequency and the voltage references. The frequency and the voltage references are then provided to the PWM generator block. Notice that the control paths have the frequency-active power and voltage-reactive power droop to establish decentralized power-sharing between multiple grid-interactive inverters in GFM mode. The droop gain parameters, m_P and m_Q, are selected such that the power-sharing is in proportion to the capacity of the inverters. The

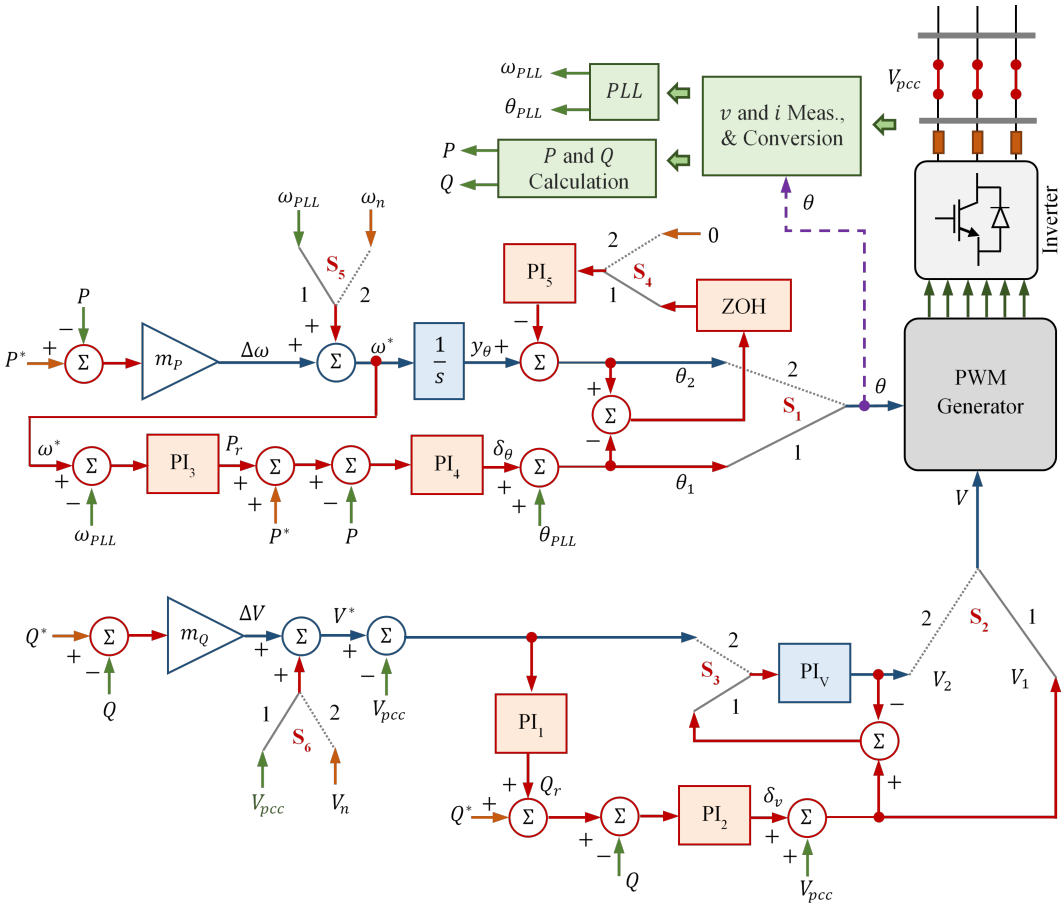

Figure 4.3: *Block diagram of the developed universal controller for GFL and GFM modes.*

developed controller has six state switches, S_{1-6}, to conduct synchronization and operation in GFL and GFM modes. Each switch can either be in Position-1, or in Position-2, based on the mode of operation. The inverter can synchronize with a grid or a microgrid in GFL mode with the switches at Position-1.The inverter can remain standby or inject a preset power with this configuration. On the other hand, the inverters can operate in GFM mode with the switches at Position 2. The state switches S_1 and S_2 send the appropriate frequency and voltage reference signals to the PWM block by engaging the output of only one pair of control paths at a certain time. The state switches S_3 and S_4 are used to synchronize the parallel pair of control paths. The state switches S_5 and S_6 are used to select between the measurement-based reference for GFL mode and the pre-set reference for GFM mode. The following subsections present the details of the operation of the universal controller for

synchronization, GFL, and GFM operations.

4.2.1 Synchronization Operation

Synchronization is needed when an inverter gets connected to a system. The developed universal controller can synchronizes an inverter with a power grid or a microgrid with its control paths at Position-1, as shown in Fig. 4.3. Irrespective of the inverters mode of operation, an incoming inverter always start with Position-1 before synchronization. At this position, the PWM block receives the phase-angle reference, $\theta_1 = \theta_{PLL}$, where θ_{PLL} is the phase-angle measurement by the PLL of the voltage at the PCC. Also, the controller sends the voltage amplitude reference, $V_1 = V_{pcc}$, where V_{pcc} is the measured voltage amplitude at the PCC. With the reference active and reactive power setpoints, P^* and Q^*, set to 0, the universal controller regulates the phase-angle adjustment, δ_θ, to zero using the proportional-integral controllers PI_4, and the voltage adjustment δ_V, to zero, using PI_2. Notice that the output of PI_3 and PI_4, P_r and Q_r, are adjusted to zero with the corresponding PI blocks during synchronization. This novel control approach, originally developed as the controller-sync method in Chapter 2, named the zero power control, allows the inverter to stay connected to the system without injecting any active and reactive power while synchronizing. Then, the inverter can either switch to GFM mode by changing the switch position to Position-2, or can contribute to power-sharing with the P^* and Q^* setpoints set to a certain value.

4.2.2 GFL Mode with Universal Controller

In GFL operation, the inverter injects active power based on the maximum available power and a given P^* setpoint. It can also provide reactive power if ancillary service is needed [13]. For example, in photovoltaic generation, the active power is typically curtailed from the maximum available power by 30% to provide flexibility for the inverter to inject reactive power if needed for the ancillary services, e.g., voltage regulation. All the switches remain at Position-1 in this mode when the inverter is synced with the grid and the active and reactive power setpoints, P^* and Q^*, are changed from 0 to the desired values. In this mode, the

active power, P is regulated to P^* by PI_4, while P_r is regulated to zero by PI_3 as $P = P^*$. Similarly, the reactive power, Q is regulated to Q^* by PI_2, while Q_r is regulated to zero by PI_1 as $Q = Q^*$. Therefore, P and Q injections are controlled by δ_θ and δ_V, respectively. In this mode, inverter is synced with the phase-angle and voltage measurements, θ_{PLL} and V_{pcc} such that the inverter remains in synchronization with the grid.

4.2.3 Seamless Transition to GFM Mode

The universal controller can perform transition to GFM mode by shifting the switch positions to Position-2. In order to transit seamlessly, the control paths at Position-2 are synced with control paths at Position-1 such that the reference signals obtained from the two sets of control paths are equal, i.e., $V_1 = V_2$ and $\theta_1 = \theta_2$, while the inverter is being operated in GFL mode. The controller gradually makes the difference between the phase angles, θ_1 and θ_2, zero by using the PI_5 controller. The zero-order hold in Fig 4.3 is used to avoid the fast variations in the angle. Similarly, PI_V reduces the difference between the voltage amplitude, V_1 and V_2 to zero. When the transition is required, e.g., the microgrid needs to be disconnected from the grid, all switches are placed to Position-2, and the inverter seamlessly transits from GFL to GFM mode. Notice that the inverters in a microgrid need to identify the event when the microgrid is disconnected from the grid, i.e., islanding detection [124, 125]. The proposed controller detects the islanding incident when the frequency exceeds the permissible limit for the inverters [25].

4.2.4 GFM Mode with Universal Controller

In GFM mode of operation of inverter, the universal controller provides the nominal frequency, ω_n and the nominal voltage, V_n to the reference by seamlessly switching S_5 and S_6 to Position-2 from Position-1, see Fig. 4.3. Also, the control paths at the Position-2 are provided to the PWM generator. Therefore, the PWM block will receive the phase-angle θ_2 directly from integrating $\omega^* = \omega_n + \Delta\omega$ and the voltage amplitude V_2 from regulating the PCC voltage, V_{PCC}, to follow $V^* = V_n + \Delta V$ using the proportional-integral block PI_V.

Notice that, unlike the GFL mode, the P^* and Q^* references at the GFM mode can be zero while injecting active and reactive power into the system. In the GFM mode, the frequency and the voltage at the PCC are allowed to deviate from their nominal values by using the $(P-f)$ and $(Q-V)$ droops. Allowing the system frequency and the voltage to deviate in a droop-based microgrid enables the inverters to share their active and reactive power without any communication. Therefore, power-sharing in proportion to the inverters capacity can be established. Notice that, synchronization is needed only for multi-inverter operation. For standalone mode of operation, the inverter does not need synchronization and can directly start with all the switches are Position-2.

4.3 Stability of Inverter with Universal Controller

In this section, the stability of the closed-loop universal inverter control scheme is analyzed. Notice that two separate state-space model exists for Position-1 and Position-2. First, a simplified model for an inverter with LCL filter, as depicted in Fig. 2.1, is derived. The linearized current flow equations of an inverter around an operating point can be expressed as,

$$\frac{d\delta i_q}{dt} = -\frac{R}{L}\delta i_q + \frac{1}{L}\,\delta v_q - \frac{1}{L}\delta v_{qpcc} - \omega\delta i_d, \tag{4.1}$$

and

$$\frac{d\delta i_d}{dt} = -\frac{R}{L}\delta i_d + \frac{1}{L}\,\delta v_d + \omega\delta i_q. \tag{4.2}$$

Here, the capacitor of the LCL filter is neglected and $L = L_f + L_c$ is assumed. The inductor's inherent resistance is denoted by R. Also, the line current flowing from the inverter i_{inv} can be considered nearly equal to the fundamental component of the line current, i_o, and hence, expressed as $i = i_i nv \simeq i_o$. The detailed derivation of (4.1) and (4.2) is available in Section 2.4.

The inverter output voltage, v_{inv} can be expressed as,

$$v_{inv}(t) = V cos\,(\theta)\,, \tag{4.3}$$

where, V and θ are the reference voltage amplitude and the phase-angle produced by the controller. The voltage v_{inv} can be separated as v_q and V_d using abc to dq transformation as follows.

$$v_q = V\ cos\left(\theta\right), \tag{4.4}$$

and

$$v_d = -V\ sin\left(\theta\right). \tag{4.5}$$

For Position-1, the linearized voltage of the inverter operating in GFL mode can be expressed as

$$\delta v_q = cos\left(\theta_{10}\right)\delta V_1 - V_{10} sin\left(\theta_{10}\right)\delta\theta_1, \tag{4.6}$$

and

$$\delta v_d = -sin\left(\theta_{10}\right)\delta V_1 - V_{10} cos\left(\theta_{10}\right)\delta\theta_1. \tag{4.7}$$

where, $\delta\theta_1$ can be obtained from the developed controller during GFL mode from Fig. 4.3 as follows,

$$\theta_1 = \theta_{PLL} + k_{P4}\left(P_r + P^* - P\right) + \int k_{I4}\left(P_r + P^* - P\right)dt, \tag{4.8}$$

where,

$$P_r = k_{P3}\left(\omega^* - \omega_{PLL}\right) + \int k_{I3}\left(\omega^* - \omega_{PLL}\right)dt, \tag{4.9}$$

and,

$$\omega^* = \omega_{PLL} - m_P(P - P^*). \tag{4.10}$$

Let y_3 and y_4 be the output of the integral terms of PI_3 and PI_4, i.e.,

$$y_3 = \int k_{I3}\left(\omega^* - \omega_{PLL}\right)dt, \tag{4.11}$$

and,

$$y_4 = \int k_{I4}\left(P_r + P^* - P\right)dt. \tag{4.12}$$

Substituting (4.9)-(4.12) in (4.8), the phase-angle reference can be expressed as,

$$\theta_1 = \theta_{PLL} + k_{P4}\left(k_{P3}m_P\left(P^* - P\right) + y_3 + P^* - P\right) + y_4, \tag{4.13}$$

which can be linearized around an operating as,

$$\delta\theta_1 = \delta y_4 + k_{P4}\delta y_3 - k_{P4}(m_P k_{P3} + 1)\delta P + \delta\theta_{PLL} + k_{P4}(m_P k_{P3} + 1)\delta P^*. \tag{4.14}$$

Also, $\dot{y}_3$ and $\dot{y}_4$ are the inputs to the integrator blocks of PI_3 and PI_4, respectively, and can be formulated as

$$\dot{y}_3 = k_{I3}m_P P^* - k_{I3}m_P P, \tag{4.15}$$

and,

$$\dot{y}_4 = k_{I4}(y_3 + (k_{P3}m_P + 1)P^* - (k_{P3}m_P + 1)P). \tag{4.16}$$

Linearzing (4.15) and (4.16) around the operating point yields,

$$\dot{\delta y}_3 = -k_{I3}m_P\delta P + k_{I3}m_P\delta P^*, \tag{4.17}$$

and,

$$\dot{\delta y}_4 = k_{I4}\delta y_3 - k_{I4}(k_{P3}m_P + 1)\delta P + k_{I4}(k_{P3}m_P + 1)\delta P^*. \tag{4.18}$$

Similarly, δV_1 can be obtained from the developed controller during GFL mode from Fig. 4.3 as,

$$V_1 = V_{pcc} + k_{P2}\left(Q_r + Q^* - Q\right) + \int k_{I2}\left(Q_r + Q^* - Q\right)dt, \tag{4.19}$$

where,

$$Q_r = k_{P1}\left(V^* - V_{pcc}\right) + \int k_{I1}\left(V^* - V_{pcc}\right)dt, \tag{4.20}$$

and,

$$V^* = V_{pcc} - m_Q(Q - Q^*). \tag{4.21}$$

Let y_1 and y_2 be the output of the integral terms of PI_1 and PI_2, i.e.,

$$y_1 = \int k_{I1} \left(V^* - V_{pcc}\right) dt, \tag{4.22}$$

and,

$$y_2 = \int k_{I2} \left(Q_r + Q^* - Q\right) dt. \tag{4.23}$$

Substituting (4.20)-(4.23) in (4.20), the voltage amplitude reference can be expressed as,

$$V_1 = V_{pcc} + k_{P2} \left(k_{P1} m_Q (Q^* - Q) + y_1 + Q^* - Q\right) + y_2, \tag{4.24}$$

which can be linearized around an operating as,

$$\delta V_1 = \delta y_2 + k_{P2} \delta y_1 - k_{P2}(m_Q k_{P1} + 1)\delta Q + \left(1 - k_{P2} k_{P1}\right) \delta V_{pcc} + k_{P2}(m_Q k_{P1} + 1)\delta Q^*. \tag{4.25}$$

Also, $\dot{y}_1$ and $\dot{y}_2$ are the inputs to the integrator blocks of PI_1 and PI_2, respectively, and can be formulated as

$$\dot{y}_1 = k_{I1} m_Q Q^* - k_{I1} m_Q Q, \tag{4.26}$$

and,

$$\dot{y}_2 = k_{I2}(y_1 + (k_{P1} m_Q + 1)Q^* - (k_{P1} m_Q + 1)Q). \tag{4.27}$$

Linearzing (4.26) and (4.27) around the operating point yields,

$$\dot{\delta y}_1 = -k_{I1} m_Q \delta Q + k_{I1} m_Q \delta Q^*, \tag{4.28}$$

and,

$$\dot{\delta y}_2 = k_{I2} \delta y_1 - k_{I2} \left(k_{P1} m_Q + 1\right) \delta Q + k_{I2} \left(k_{P1} m_Q + 1\right) \delta Q^*. \tag{4.29}$$

Substituting (4.14) and (4.25) into (4.6) and (4.7) gives,

$$\begin{aligned}\delta v_q = cos\left(\theta_{10}\right)\delta y_2 + k_{P2}\delta y_1 - k_{P2}(m_Q k_{P1}+1)\delta Q + \left(1-k_{P2}k_{P1}\right)\delta V_{pcc} \\ +k_{P2}(m_Q k_{P1}+1)\delta Q^*) - V_{10}sin\left(\theta_{10}\right)\delta y_4 + k_{P4}\delta y_3 - k_{P4}(m_P k_{P3}+1)\delta P \\ +\delta\theta_{PLL} + k_{P4}(m_P k_{P3}+1)\delta P^*),\end{aligned} \tag{4.30}$$

and

$$\begin{aligned}\delta v_d = -sin\left(\theta_{10}\right)\left(\delta y_2 + k_{P2}\delta y_1 - k_{P2}(m_Q k_{P1}+1)\delta Q + \left(1-k_{P2}k_{P1}\right)\delta V_{pcc}\right. \\ \left.+k_{P2}(m_Q k_{P1}+1)\delta Q^*\right) - V_{10}cos\left(\theta_{10}\right)\left(\delta y_4 + k_{P4}\delta y_3 - k_{P4}(m_P k_{P3}+1)\delta P\right. \\ \left.+\delta\theta_{PLL} + k_{P4}(m_P k_{P3}+1)\delta P^*\right).\end{aligned} \tag{4.31}$$

Now, substituting δP form (2.23) and δQ form (2.24) in (4.17), (4.18), and (4.28)−(4.31), and combining with (4.1) and (4.2) yields the state-space representation of the closed-loop inverter operating in the GFL mode as follows

$$\frac{d}{dt}\begin{bmatrix}\delta i_q\\ \delta i_d\\ \delta y_1\\ \delta y_2\\ \delta y_3\\ \delta y_4\end{bmatrix} = \begin{bmatrix}a_{11} & a_{12} & a_{13} & a_{14} & a_{15} & a_{16}\\ a_{21} & a_{22} & a_{23} & a_{24} & a_{25} & a_{26}\\ a_{31} & a_{32} & a_{33} & a_{34} & a_{35} & a_{36}\\ a_{41} & a_{42} & a_{43} & a_{44} & a_{45} & a_{46}\\ a_{51} & a_{52} & a_{53} & a_{54} & a_{55} & a_{56}\\ a_{61} & a_{62} & a_{63} & a_{64} & a_{65} & a_{66}\end{bmatrix}\begin{bmatrix}\delta i_q\\ \delta i_d\\ \delta y_1\\ \delta y_2\\ \delta y_3\\ \delta y_4\end{bmatrix} + \begin{bmatrix}b_{v1} & b_{\theta 1} & b^U_{P1} & b^U_{Q1}\\ b_{v2} & b_{\theta 2} & b^U_{P2} & b^U_{Q2}\\ b^U_{v3} & b_{\theta 3} & b^U_{P3} & b^U_{Q3}\\ b^U_{v4} & b_{\theta 4} & b^U_{P4} & b^U_{Q4}\\ b_{v5} & b_{\theta 5} & b^U_{P5} & b^U_{Q5}\\ b_{v6} & b_{\theta 6} & b^U_{P6} & b^U_{Q6}\end{bmatrix}\begin{bmatrix}\delta v_{qpcc}\\ \delta\theta_{PLL}\\ \delta P^*\\ \delta Q^*\end{bmatrix} \tag{4.32}$$

Here, $\delta V_{pcc} = \delta v_{qpcc}$ and $\delta v_{dpcc} = 0$. Notice that the state matrix in (4.32) is exactly same as the state-matrix in (2.39). On the other hand, the control-matrix is different. The new and the modified elements in the control matrix are denoted by the superscript 'U' and are provided in Appendix A.2.

For Position-2, the linearized voltage of the inverter operating in GFM mode can be

expressed as,

$$\delta v_q = cos\left(\theta_{20}\right)\delta V_2 - V_{20} sin\left(\theta_{20}\right)\delta\theta_2, \tag{4.33}$$

and

$$\delta v_d = -sin\left(\theta_{20}\right)\delta V_2 - V_{20} cos\left(\theta_{20}\right)\delta\theta_2. \tag{4.34}$$

From Fig. 4.3, the phase-angle reference in GFM mode can be expressed as,

$$\theta_2 = y_\theta, \tag{4.35}$$

and the voltage amplitude reference can be expressed as,

$$V_2 = k_{PV}\left(V_n - m_Q(Q - Q^*) - V_{pcc}\right) + y_V, \tag{4.36}$$

where, y_V is the output of the integrator block, PI_V

$$y_V = \int k_{IV}\left(V_n - m_Q(Q - Q^*) - V_{pcc}\right) dt, \tag{4.37}$$

Linearizing (4.35) and (4.36) around the operating point yields,

$$\delta\theta_2 = \delta y_\theta, \tag{4.38}$$

and

$$\delta V_2 = -k_{PV} m_Q \delta Q + k_{PV} m_Q \delta Q^* + \delta y_V - k_{PV}\delta V_{pcc}. \tag{4.39}$$

Substituting (4.35) and (4.36) in (4.33) and (4.34) generates,

$$\delta v_q = cos\left(\theta_{20}\right)\left(k_{PV} m_Q \delta Q + k_{PV} m_Q \delta Q^* + \delta y_V - k_{PV}\delta V_{pcc}\right) - V_{20} sin\left(\theta_{20}\right)\delta y_\theta, \tag{4.40}$$

and

$$\delta v_d = -sin\left(\theta_{20}\right)\left(k_{PV} m_Q \delta Q + k_{PV} m_Q \delta Q^* + \delta y_V - k_{PV}\delta V_{pcc}\right) - V_{20} cos\left(\theta_{20}\right)\delta y_\theta. \tag{4.41}$$

Also, the inputs to the integrator block of PI_V, $\dot{y}_V$, and the inputs to the integrator block for phase-angle control, $\dot{y}_\theta$, can be written as

$$\dot{y}_\theta = \omega_n - m_P(P - P^*), \tag{4.42}$$

and

$$\dot{y}_V = k_{IV}\left(V_n - V_{pcc}\right) - k_{IV}m_Q(Q - Q^*). \tag{4.43}$$

Linearizing (4.42) and (4.43) gives,

$$\dot{\delta y}_\theta = -m_P\delta P + m_P\delta P^*, \tag{4.44}$$

and

$$\dot{\delta y}_V = -k_{IV}m_Q\delta Q + k_{IV}m_Q\delta Q^* - \ k_{IV}\delta V_{pcc}. \tag{4.45}$$

Now, substituting δP form (2.23) and δQ form (2.24) in (4.40), (4.41), (4.44), and (4.45), and combining with (4.1) and (4.2) yields the state-space representation of the closed-loop inverter operating in the GFM mode as follows

$$\frac{d}{dt}\begin{bmatrix}\delta i_q\\ \delta i_d\\ \delta y_\theta\\ \delta y_V\end{bmatrix} = \begin{bmatrix}\alpha_{11} & \alpha_{12} & \alpha_{13} & \alpha_{14}\\ \alpha_{21} & \alpha_{22} & \alpha_{23} & \alpha_{24}\\ \alpha_{31} & \alpha_{32} & \alpha_{33} & \alpha_{34}\\ \alpha_{41} & \alpha_{42} & \alpha_{43} & \alpha_{44}\end{bmatrix}\begin{bmatrix}\delta i_q\\ \delta i_d\\ \delta y_\theta\\ \delta y_V\end{bmatrix} + \begin{bmatrix}\beta_{v1} & \beta^U_{P1} & \beta^U_{Q1}\\ \beta_{v2} & \beta^U_{P2} & \beta^U_{Q2}\\ \beta_{v3} & \beta^U_{P3} & \beta^U_{Q3}\\ \beta_{v4} & \beta^U_{P4} & \beta^U_{Q4}\end{bmatrix}\begin{bmatrix}\delta v_{qpcc}\\ \delta P^*\\ \delta Q^*\end{bmatrix}. \tag{4.46}$$

Here, $\delta V_{pcc} = \delta v_{qpcc}$ and $\delta v_{dpcc} = 0$. Similar to (4.32), the state-matrix is same as the state-matrix of (2.48) and the matrix elements are presented in Appendix A.1. On the other hand, the control-matrix is different and the matrix elements are presented in Appendix A.2.

Figs. 4.4(a) and 4.4(b) show the root locus of the eigenvalues of the proposed closed-loop controller for GFL and GFM modes of operation, respectively. For both scenarios, the active power injection of the inverter is increased from 0 to 20 kW. The red crosses indicate the eigenvalues at the 0 power injection. In Fig. 4.4(a), λ^1_{1-6} denote the six eigenvalues for the

inverter in GFL mode. In Fig. 4.4(b), λ^2_{1-4} denote the four eigenvalues for the inverter in GFM mode. Notice that the system is stable for both scenarios, as all the eigenvalues are on the left-half plane. However, as the power increases, the eigenvalues of the inverter in GFM move more quickly to the right side compared to its eigenvalues in GFL mode. This suggests that the inverter that might be stable in GFL mode can become unstable at the same power level in GFM mode. Therefore, a careful selection of the controller gains based on the load in the microgrid and the capacity of the inverter is needed so that the inverters do not become unstable when transitioning from GFL to GFM mode.

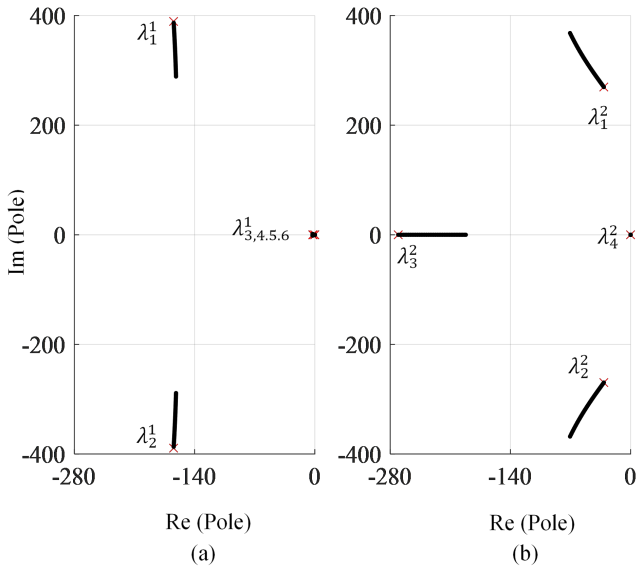

Figure 4.4: *Eigenvalues of the inverter with closed-loop control from active power injection from 0 to 20 kW; (a) when the inverter is operating in the grid-following mode, (b) when the inverter is operating in the grid-forming mode.*

4.4 Experiment Results

In this section, the performance of the universal controller is presented for the grid-connected and islanded operation of a microgrid in two different loading scenarios. The experimental setup of a laboratory-scale three-phase microgrid testbed is the same as in the experimental setup in Chapter 2, see Fig. 2.6. The testbed consists of three 5 *kVA* SiC inverters and one

10 kVA Si inverter powered fed by four programmable dc sources.

Table 4.1: *System Parameters for Universal Inverter in Chapter 4.*

Parameter	Value
Nominal line-line voltage, V_n	208 V
DC bus voltage, V_{dc}	350 V
Nominal frequency, ω_n	$2\pi(60)$ rad/s
PWM switching frequency, f_{PWM}	5 kHz
Inverter side inductance, L_f	1 mH
PCC side inductance, L_c	0.5 mH
Filter capacitance, C_f (in Δ)	5 μF
Filter damping resistance, R_{cf} (in Δ)	1.65 Ω
Tie-line inductance, L_{line}	5 mH
Tie-line resistance, R_{line}	1 Ω
Grid inductance, L_{grid}	0.4 mH
Grid resistance, R_{grid}	0.2 Ω
Droop parameters	$m_P = 0.005$, $m_Q = 0.001$

Table 4.2: *Controller Parameters for Universal Inverters in Chapter 4.*

Controller	k_P	k_I
PI_V	0.0005	0.25
X_{vir}	5.5	–
PI_1	0.05	5
PI_2	0.0001	0.005
PI_3	0.5	10
PI_4	0	0.0001
PI_5	0.1	1

The microgrid is also connected to a 30 kVA grid-emulator through a circuit breaker for grid-connected operations. Each inverter setup is equipped with LCL filters, voltage and current measurement sensors, and circuit breakers. Two three-phase 5 kW variable loads are connected at two different nodes of the microgrid. The PWM signals are provided using four dSPACE 1202 MicroLabBox controllers, where the closed-loop controls are implemented. All data are acquired by the ControlDesk of dSPACE and then plotted by MATLAB. For the experimental results presented in this chapter, only a part of the microgrid setup resembling

the schematic diagram in Fig. 2.1 is used. The following two case scenarios are tested during the experiments. In both cases, the two universal inverters have been operating in GFL mode, and then the microgrid is suddenly disconnected from the grid. The system and control parameters are given in Tables 4.1 and 4.2, respectively.

4.4.1 Power Generation is Greater than the Load

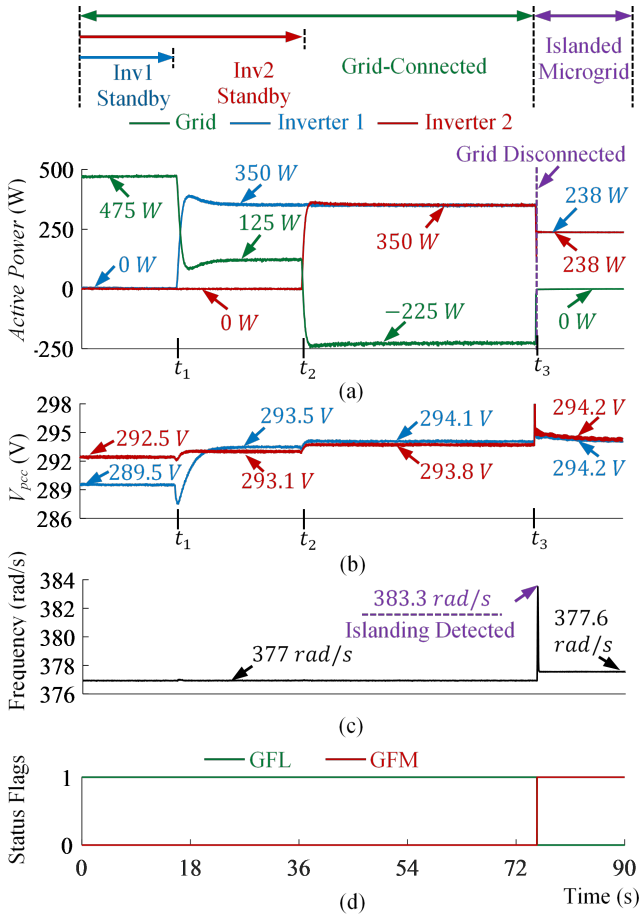

Figure 4.5: *Performance of the universal inverter in grid-connected and islanded mode, before and after an islanding event, when the active power generation is greater than the local load, (a) active power injected by grid, Inv*1*, and Inv*2*, (b) line-to-line voltage amplitudes at the PCCs of Inv*1 *and Inv*2*, (c) system frequency, and (d) controller status or operational mode.*

In this test, the net power supplied by the two inverters is more than the power consumed by the local loads, see Fig. 4.2(a). Both inverters are operated in GFL mode at the given

active and reactive power setpoints. The excess power is fed to the grid. At first, the 475 W load is powered by only the grid-emulator. Fig. 4.5 shows the experiment results. Notice, in Fig 4.5, the active power injected by the two inverters is controlled to 0 by the developed controller, even though the circuit breakers are connected. Then, at $t_1 = 15.84\ s$, $Inv1$ starts injecting 350 W of active power in grid-following mode. $Inv2$ starts injecting 350 W at $t_2 = 36.4\ s$. At this stage, the 225 W of excess power is fed to the grid. Finally, the grid is disconnected at $t_3 = 75.5\ s$. The amplitude of the PCC voltages and the system frequency are shown in Figs. 4.5(b) and 4.5(d), respectively. Notice that the system frequency remains 377 rad/s while the grid exists. As soon as the grid is disconnected, the system frequency starts to change from the nominal value, and the controller detects the islanding at 383.3 rad/s. Then, the controller immediately switches to GFM mode and continues the islanded microgrid operation. Fig. 4.5(a) also shows the decentralized power-sharing between

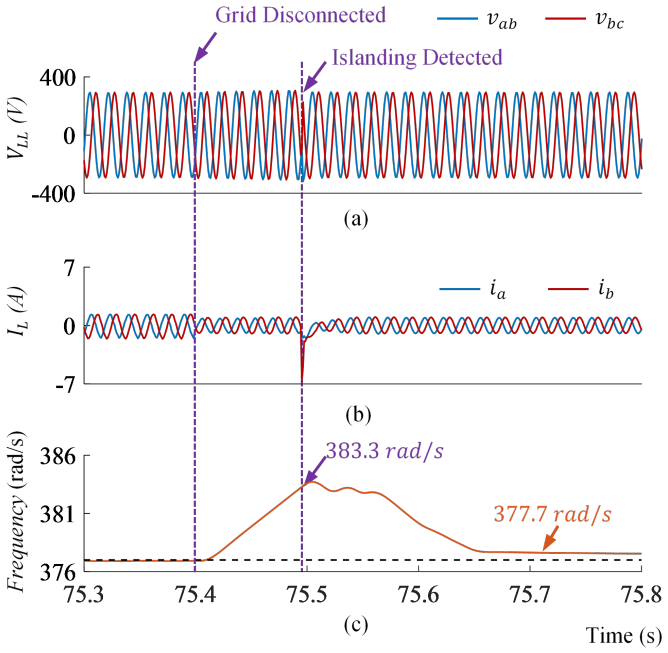

Figure 4.6: *Expanded view of (a) line-line voltage and (b) current of $Inv1$, and (c) the system frequency, before and after an islanding event, when the power generation of the inverters with the universal control is greater than the load.*

the two inverters, where each inverter shares 238 W of load. The system's frequency also changed from the nominal value during GFM mode of operation. Figs. 4.5(c) and 4.5(d)

show that as soon as the inverters detect the frequency passing the threshold value, they change the mode from GFL to GFM. Here, in Fig. 4.5(d), the status of the controllers is denoted as GFL and GFM. Fig. 4.6 shows an expanded plot of the line-line voltages, line-current, and frequency of $Inv1$ when the mode changes from GFL to GFM. Notice that the voltage and the current waveforms are not distorted after the mode changes. Also, the islanding detection based on frequency measurement is clearly seen in Fig. 4.6(c).

4.4.2 Power Generation is Less than the Load

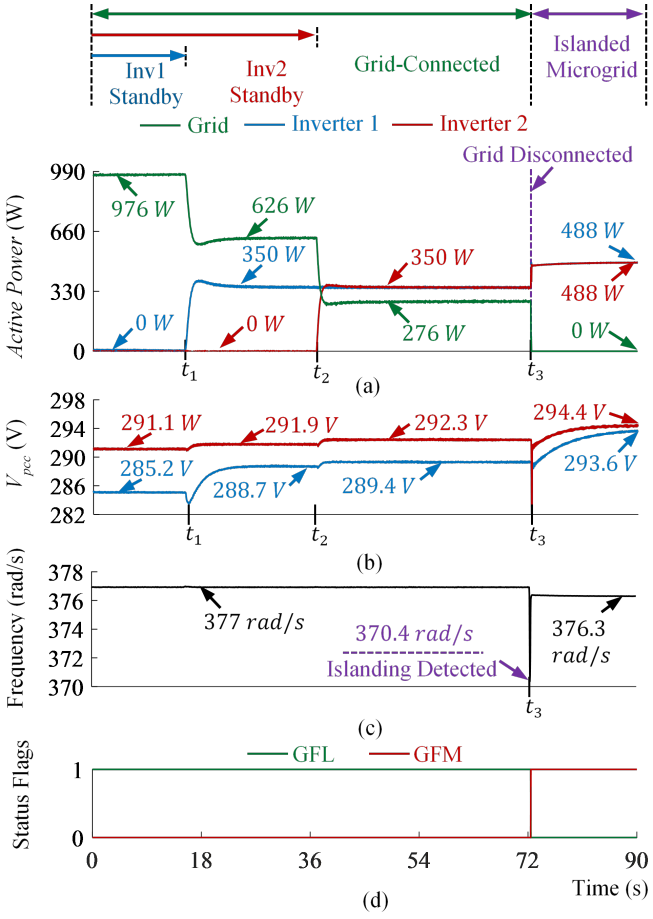

Figure 4.7: *Performance of the universal inverter in grid-connected and islanded mode, before and after an islanding event, when the active power generation is less than the local load, (a) active power injected by grid, Inv*1*, and Inv*2*, (b) line-to-line voltage amplitudes at the PCCs of Inv*1 *and Inv*2*, (c) system frequency, and (d) controller status or operational mode.*

In this test, the load connected to the microgrid is greater than the net power generated by the two inverters. Therefore, the grid must feed part of the total load. Similar to the previous case, the active and the reactive power setpoints are set to 350 W for both the inverters in GFL mode. However, the load is now 976 W, and the remaining power, i.e., 276 W, is being supplied by the grid. Fig. 4.7(a) shows the active power injected by the grid and the two inverters. Here, $Inv1$ and $Inv2$ started injecting power at $t_1 = 15.24\ s$ and at $t_2 = 36.3\ s$, respectively, and the grid is disconnected at $t_3 = 72.4\ s$. Fig. 4.7(b) shows the voltages at the PCCs of the two inverters. Notice that the frequency is deviating from the nominal value after the grid is disconnected. In this scenario, the islanding detection has been made by measuring the frequency passing the 370.4 rad/s level. The inverters immediately shifted to GFM mode, with both inverters sharing an equal load of 488 W. The droop parameters of the controller establish the load sharing ratio to provide equal power. The system's frequency also changed from the nominal value during GFM mode of operation. Fig. 4.7(c) and 4.7(d) shows both inverters detect the islanding condition quickly at the same time. Notice that the inverters are injecting more power than the defined setpoints in GFM mode. This ensures the continuous operation of the microgrid after islanding. However, there can be situations where the inverters' net capacity is insufficient to feed all the loads after the grid is disconnected. Partial load-shedding might be required under this circumstance. Fig. 4.8 shows an expanded plot of the line-line voltages, line-current, and frequency of $Inv1$ when the mode changes from GFL to GFM. In this scenario, the voltage and the current waveforms are not distorted after the mode changes. The islanding detection based on frequency measurement is also observed seen in Fig. 4.8(c). Fig. 4.9 shows a picture of the test setup during verification of the universal controller in two inverters

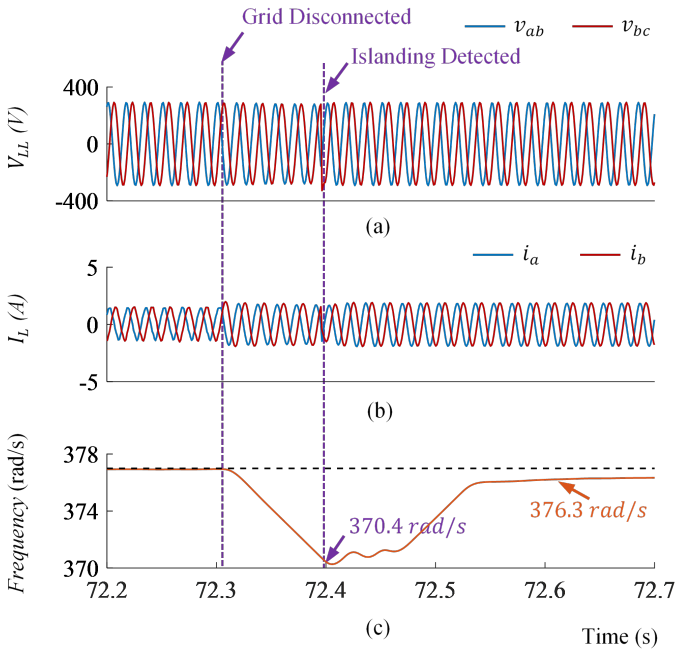

Figure 4.8: *Expanded view of (a) line-line voltage and (b) current of Inv*1*, and (c) the system frequency, before and after an islanding event, when the power generation of the inverters with the universal control is less than the load.*

Figure 4.9: *Experimental verification of the universal controller.*

4.5 Conclusion

In this chapter, a universal controller for grid-interactive inverters has been developed for operating in both GFL and GFM modes. The developed inverter has been able to seamlessly sync with a grid and microgrid. A detailed small signal stability analysis has been derived for the inverter controller operating in GFL and GFM modes. The performance of the developed controller has been verified in a microgrid testbed for grid-connected and islanded operations. The following conclusions can be highlighted–

- A universal inverter has developed that can operates in GFM and GFL mode and seamlessly sync with the rest of the ac sources in a grid/microgrid.
- The universal controller has been able to seamlessly transit two inverter in GFL mode to GFM mode during grid disconnection.
- State-space analysis has shows that an inverter in GFM mode can be unstable at a power level even though the inverter is stable in GFL mode.

Chapter 5

Frequency and Voltage Restoration for GFM Inverters

This chapter presents a novel frequency and voltage restoration control for GFM inverters in islanded mode of operation. In power grid, frequency is the system parameter which is accessible to all the power generation unit, like a global parameter. Therefore, the GFM inverters in a microgrid can utilize the frequency measurements for adjusting their power contributions. Similarly, voltage measurements at the PCC of the inverter can also be used to adjust the power contribution between the inverters. Here, voltage measurement at the PCCs of different GFM inverters can be different, but are regulated by the GFM inverters, and therefore, can be used for power-sharing. The droop control method presented in Chapter 2 used frequency-active power and voltage-reactive power droop for power-sharing. As seen in Chapter 2, the system frequency and the voltage at the PCC are allowed to vary in droop control mode. This might result in excessive deviation of the frequency and the voltage amplitude from their nominal values, particularly in a small microgrid where all inverters are in GFM mode, resulting in tripping the inverters. This can be prevented by regulating the frequency and the voltage by the GFM inverters. On the contrary, regulating the parameters would make the decentralized power-sharing capability ineffective. In this chapter, a solution to the frequency and voltage restoration challenge of the GFM inverters in islanded microgrid

while continuing power-sharing between the inverters in decentralized mode, is developed. The developed method enables the GFM inverters to restore the frequency to the nominal value and regulate their bus voltage amplitudes after any load change or plug-in of inverters.

This chapter is organized into five sections. A brief description on the system under study is presented in Section 5.1. Section 5.2 presents the developed controller and describes its operation. The details of the dynamic model of an inverter equipped with enabled restoration paths is derived, the state-space model is developed, and stability analysis under different load conditions and parameter variations are performed in Section 5.3. Section 5.4 demonstrates the performance of the developed controller through experimental results. The conclusion of this chapter is summarized in Section 5.5.

5.1 System Description

In this section, the small-scale microgrid system that is used for the performance verification of the developed controller, is briefly described. Here, the same system as in Chapter 2, where the two inverters, $Inv1$ and $Inv2$, operate in GFM mode. The inverters are connected to a tie-line through filters and circuits breakers. The tie-line connects $Bus-1$ to $Bus-2$ and is represented by a series of resistors and inductors. Two seperate DC sources feed the inverters. Each setup has voltage and current sensors to measure the inverter's output voltage and the line currents. The three-phase load is connected at $Bus-1$. The inverters are separately and independently controlled by two controllers that generate desired voltage amplitude and phase-angle references for the PWM generation units. The restoration controller presented in this chapter is built upon the universal controller developed in Chapter 4. Therefore, the developed controller is independent of communication, can seamlessly synchronize and contribute power-sharing, can operate in both GFL and GFM modes, and can restore the frequency and voltage of the system after any load change or plug-in events. Also, the developed controller is applicable for any number of inverters in a microgrid.

5.2 The Developed Controller for Restoration

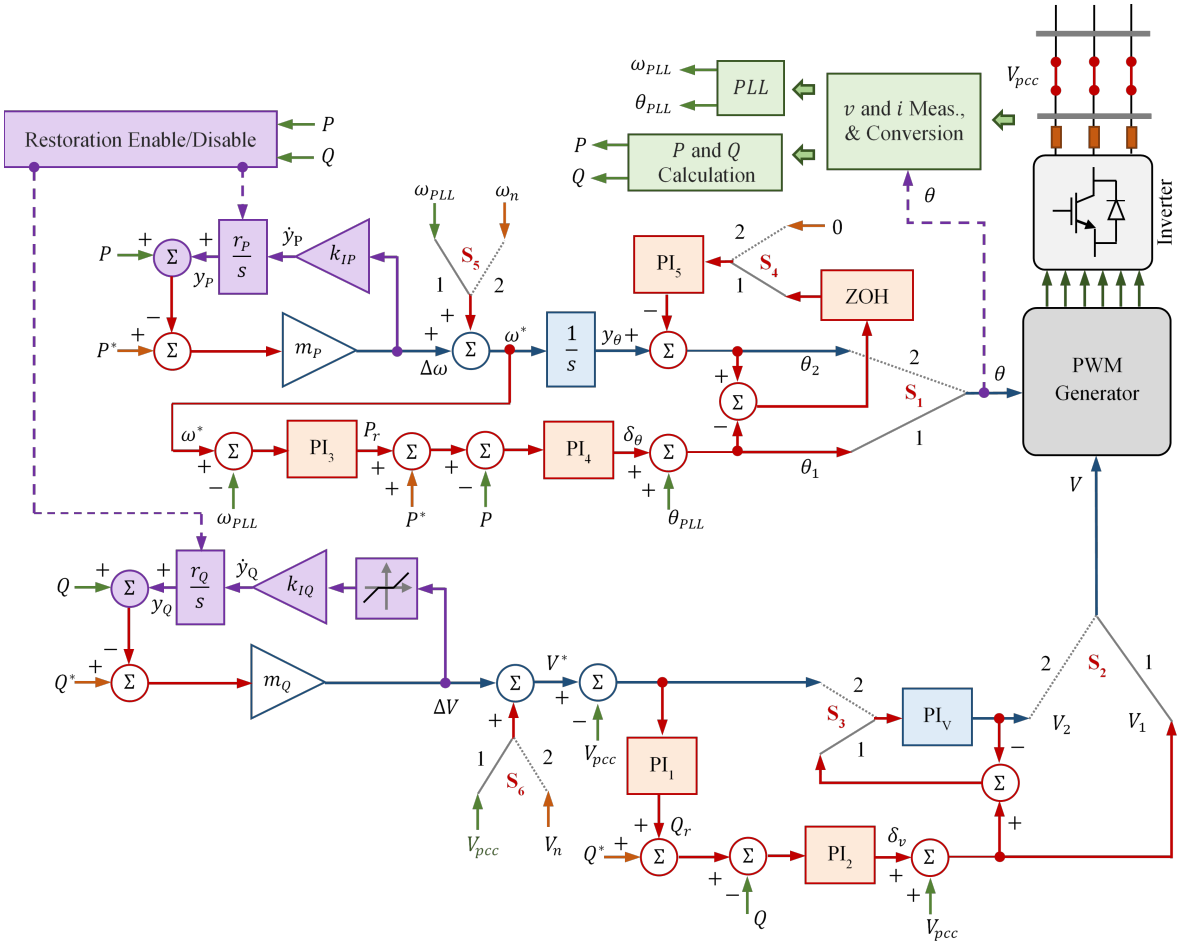

Figure 5.1: *Block diagram of the universal controller with restoration control in GFM mode.*

The controller for frequency and voltage restoration is developed upon the universal controller, presented in Chapter 4. Therefore, the controller is capable of perform seamless synchronization, operation in GFL and GFM mode, decentralized power-sharing, and frequency and voltage restoration in GFM mode. Fig. 5.1 depicts the block diagram of the developed controller. Notice that, two feedback paths, called restoration paths in this dissertation, are added to the universal controller in Fig. 4.3. In addition, a control block, called restoration enable/disable, is added to control the operation of the restoration paths. All state switches, S_{1-6}, are set to Position-2 in GFM mode of operation.

When the restoration is disabled in GFM mode, the required change in frequency, $\Delta\omega$,

is obtained by multiplying the difference between the reference active power, P^* and the measured active power, P, with the droop gain, m_P for decentralized power-sharing, i.e,

$$\Delta\omega = m_P \left(P^* - P\right). \tag{5.1}$$

Notice that, in GFM mode, P^* is typically set to zero. However, when the restoration path is enabled, $\Delta\omega$ is gradually reduced to zero by the loop operation of the restoration path, making the inverter's angular frequency, ω^*, equal to the nominal angular frequency, ω_n. The expression of $\Delta\omega$ at any time when the restoration is enabled, is expressed as,

$$\Delta\omega = m_P \left(P^* - P - y_P\right), \tag{5.2}$$

where,

$$\dot{y}_P = k_{IP}\Delta\omega \tag{5.3}$$

Similarly, the required change in voltage amplitude, ΔV, is obtained by multiplying the difference between the reference reactive power, Q^* and the measured reactive power, Q, with the droop gain, m_Q for decentralized power-sharing, i.e,

$$\Delta V = m_Q \left(Q^* - Q\right). \tag{5.4}$$

Here, Q^* is commonly set to zero. Also, when the restoration path is enabled, ΔV is gradually reduced to zero by the loop operation of the restoration path, making the inverter's output voltage amplitude, V^*, equal to the nominal voltage, V_n. Therefore, the expression of ΔV is expressed as,

$$\Delta V = m_Q \left(Q^* - Q - y_Q\right), \tag{5.5}$$

where,

$$\dot{y}_Q = k_{IQ}\Delta V \tag{5.6}$$

However, it is also necessary to allow the voltage to deviate from nominal value to allow

reactive power flow between the inverters. Therefore, a small tolerance band around the nominal voltage amplitude is set to the controller, see Fig. 5.1. The k_{IP} in (5.3) and the k_{IQ} in (5.6) are restoration gain parameters for the frequency and voltage restoration paths.

In frequency and voltage restoration, the main challenge is to complete the process without loosing the capability of decentralized power-sharing. Therefore, the restoration process is only enabled when a change in power injection due to any load change or plug-in of an inverter is detected and disabled when the restoration is complete. Fig. 4.3 shows the algorithm for enabling and disabling the restoration paths. The integral term in the restoration paths introduces a delay in the restoration process. Due to this delay, even though the restoration is enabled almost immediately after detecting a change in power, the frequency and voltage parameters are also able to deviate, allowing the power-sharing process perform faster than the restoration process. The delay-time can be adjusted with the proper selection of the values of k_{IP} and k_{IQ}. By combining (5.2) and (5.3), one can write

$$\dot{y}_P + (m_P k_{IP})\, y_P = m_P k_{IP}\,(P^* - P)\,. \tag{5.7}$$

Assuming, $P^* = 0$, for a unit step change in active power, P, the change in the frequency response can be obtained from (5.2) as,

$$\Delta\omega(t) = -\Delta\omega\left(0^+\right) e^{-(m_P k_{IP})t}, \tag{5.8}$$

where $\Delta\omega\,(0^+) = m_p\,\{P\,(0^+) - P\,(0^-)\}$. Here, t is the time counting from the detection of change in active power injection. By using the rule of 5τ, the settling time of (5.8) is $5/\,(m_P k_{IP})$. Therefore, to fully complete the restoration process, the droop parameter, m_P, and the restoration gain parameter, K_{IP}, must be chosen such that, the restoration path remain enabled for at least $5/\,(m_P k_{IP})$ time. Similarly, by combining (5.5) and (5.6), the following differential equation can be developed.

$$\dot{y}_Q + (m_Q k_{IQ})\, y_Q = m_Q k_{IQ}\,(Q^* - Q)\,, \tag{5.9}$$

Therefore, for a unit step change in reactive power, Q, the change in the voltage response at $Q^* = 0$ becomes,

$$\Delta V(t) = -\Delta V\left(0^+\right) e^{-\left(m_Q k_{IQ}\right)t}, \tag{5.10}$$

where $\Delta V\left(0^+\right) = m_Q\left\{Q\left(0^+\right) - Q\left(0^-\right)\right\}$. Here, t denotes the time counting from the detection of the change in the reactive power injection and the settling time of (5.10) is $5/\left(m_Q k_{IQ}\right)$. Since, the frequency and the voltage restoration time are the functions of $m_P k_{IP}$ and $m_Q k_{IQ}$, respectively, for the GFM inverters, having different values in different inverters can result in conflicts between the active and reactive power-sharing and frequency/voltage restorations. Therefore, it is necessary to choose same $m_P k_{IP}$ and $m_Q k_{IQ}$ values for all the inverters in a network, whereas, m_P and m_Q values for power-sharing in proportion to the inverters' capacities can be different. Figs. 5.2(a)-(d) shows simulated response of the frequency and the voltage restoration paths. In Fig. 5.2(a), the droop coefficient m_P is varied from 0 to 0.01 with an active power step of 1 kW. As expected, a higher values of the droop gain parameter can provide faster response, but with more frequency deviation. The frequency responses in Fig. 5.2(b) for different values of k_{iP} shows that the response is faster at higher values of restoration gain parameters. Similar response is observed in Figs. 5.2(c)-(d) for voltage restoration.

Fig. 5.3 shows the algorithm for the developed threshold-based restoration enable/disable control block of Fig. 5.1. The controller detects the change in active and reactive power when $\left|P\left(0^-\right) - P\left(0^+\right)\right| > \varepsilon_P$ and $\left|Q\left(0^-\right) - Q\left(0^+\right)\right| > \varepsilon_Q$, where ε_P and ε_Q are the predefined thresholds for the change in active and reactive power, respectively. When the controller detects the change in the active power, the frequency restoration path is made enabled by setting the gain parameter of the integral block, r_P, to 1 and restoration gain parameters, k_{IP}, to a preset value from zeros. Similarly, when the controller detects the change the in reactive power, the frequency restoration path is made enabled by setting the gain parameter of the integral block, r_Q, to 1 and restoration gain parameters, k_{IQ}, to a preset value from zeros. The restoration paths are disabled when the frequency and the voltage are restored to the desired values. For frequency restoration, the control path is kept enabled till

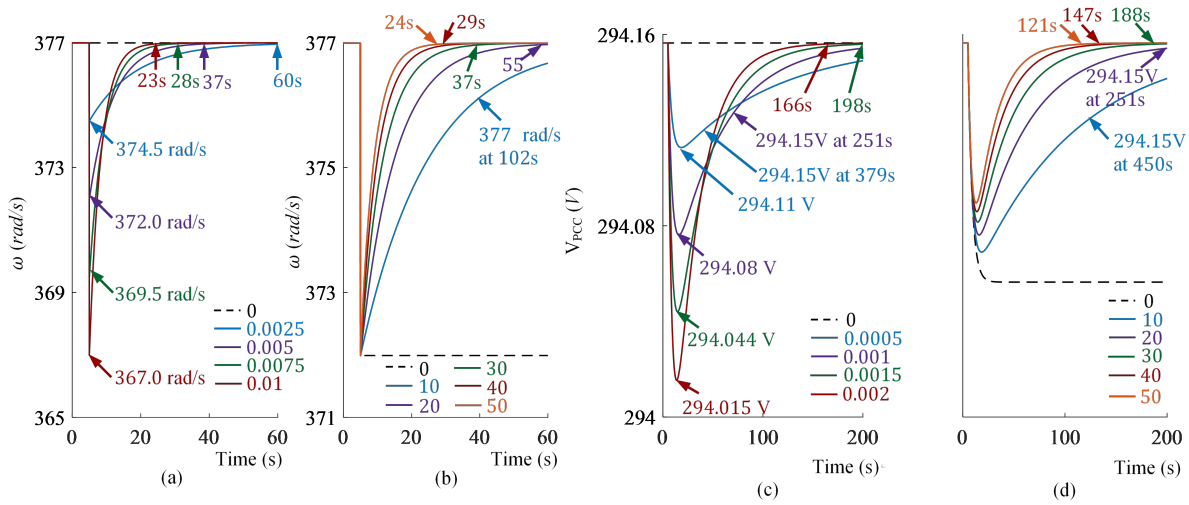

Figure 5.2: *Simulation results showing the response of the frequency control path for (a)* $m_P = 0,\ 0.0025,\ 0.005,\ 0.0075,\ 0.01$, *and (b)* $k_{IP} = 0,\ 10,\ 20,\ 30,\ 40,\ 50$, *and of the voltage control path for (c)* $m_Q = 0,\ 0.0005,\ 0.001,\ 0.0015,\ 0.002$, *and (d)* $k_{IQ} = 0,\ 10,\ 20,\ 30,\ 40,\ 50$.

$|\omega_n - \omega| < \varepsilon_\omega$. On the other hand, for voltage restoration, the inverter's voltage amplitude is restored around its nominal value with in a predefined voltage band, ΔV_{band}, instead of regulating at a fixed number, i.e., V_n. Therefore, the voltage restoration path is disabled when $|V_n \pm \Delta V_{band} - V| < \varepsilon_V$. Here, ε_ω and ε_V are the preset threshold values, which must be set by a well defined standard. The threshold for detecting the active power change, ε_P, can be obtained from the droop parameter, m_p, and ε_ω. The restoration remains disabled, if the frequency changes within $2\varepsilon_\omega$. Therefore, the minimum change of active power allowed without enabling the frequency restoration is $2\varepsilon_\omega/m_P$. Similarly, the minimum change of reactive power allowed without enabling the voltage restoration is $2\varepsilon_V/m_Q$. Hence, the following two conditions can be developed.

$$\varepsilon_P \geq \frac{2\varepsilon_\omega}{m_P}, \tag{5.11}$$

and

$$\varepsilon_Q \geq \frac{2\varepsilon_V}{m_Q}. \tag{5.12}$$

The restoration paths are disabled by resetting r_P and k_{IP}, and r_Q and k_{IQ} to zeros.

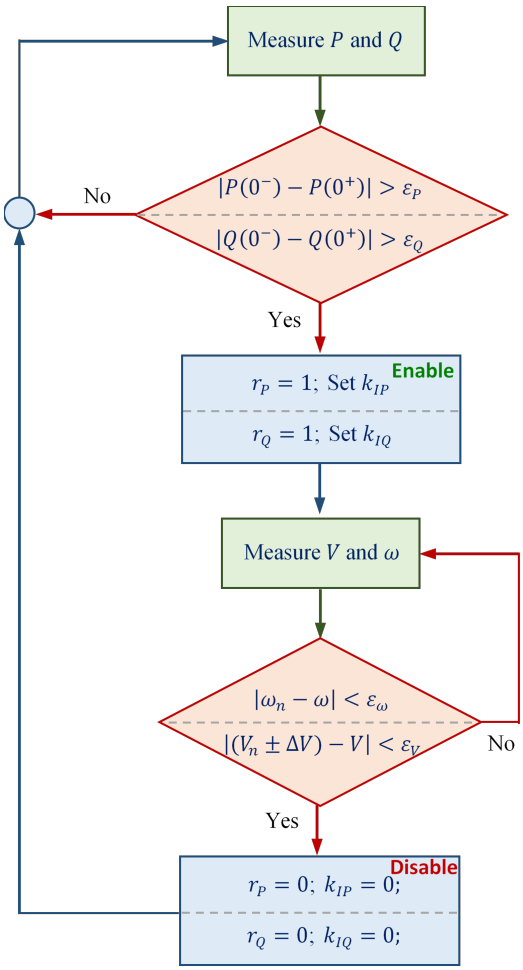

Figure 5.3: *Algorithm for enabling and disabling the restoration paths for the controller in Fig. 5.1.*

Notice that, both the frequency and the voltage restoration control paths can be separately enabled and disabled without affecting the operation of the other path.

5.3 State-Space Modeling and Stability Analysis

The stability of the developed controller for frequency and voltage restoration under different load and controller parameter variation is analyzed in this section. The stability analysis is performed through a state-space model of a three-phase inverter with the controller in Fig. 5.1. Restoration is only required for the GFM mode of operation. Therefore, the state-space model presented in this chapter is developed only when all the switches are in

Position-2 and the restoration paths are enabled.

First, the three-phase inverter with the LCL filter is modeled. To simplify the model, $L = L_f + L_c$ can be assumed, and the capacitor of the LCL filter can be neglected. Therefore, i_{inv}, the line current from the inverter is considered almost equal to i_o, the fundamental component of the output line current, i.e., $i = i_{inv} \simeq i_o$. The linearized current flow equations around an operating point can be expressed as,

$$\frac{d\delta i_q}{dt} = -\frac{R}{L}\delta i_q + \frac{1}{L}\,\delta v_q - \frac{1}{L}\delta v_{qpcc} - \omega\delta i_d, \tag{5.13}$$

and

$$\frac{d\delta i_d}{dt} = -\frac{R}{L}\delta i_d + \frac{1}{L}\,\delta v_d + \omega\delta i_q. \tag{5.14}$$

Here, R denotes the inductor's inherent resistance. A detailed derivation process of (5.13) and (5.14) is available in Chapter 2. The output voltage of the inverter, v_{inv} is represented as,

$$v_{inv}(t) = V cos\,(\theta)\,, \tag{5.15}$$

The V and θ in (5.15) are the reference voltage amplitude and the phase-angle input to the PWM generator. Separating the voltage, v_{inv}, into v_q on q-axis, and into v_d on d-axis through abc to dq transformation yields,

$$v_q = V\ cos\,(\theta)\,, \tag{5.16}$$

and

$$v_d = -V\ sin\,(\theta)\,. \tag{5.17}$$

From Fig. 5.1, the phase-angle reference for GFM mode, $\theta = \theta_2$, can be expressed as,

$$\theta = y_\theta. \tag{5.18}$$

where,

$$\dot{y_\theta} = \omega_n + \left(\frac{1}{k_{IP}}\right) \dot{y_P}. \tag{5.19}$$

Linearizing (5.19) around the operating point yields,

$$\delta\dot{y_\theta} = \left(\frac{1}{k_{IP}}\right) \delta\dot{y_P}. \tag{5.20}$$

Integrating both sides of (5.20) results in

$$\delta y_\theta = \left(\frac{1}{k_{IP}}\right) \delta y_P. \tag{5.21}$$

Similarly, from the voltage restoration control path, the following relationship is formed.

$$\dot{y_V} = k_{IV} \left(\frac{1}{k_{IQ}} \dot{y_Q} + V_n - V_{pcc}\right), \tag{5.22}$$

where y_V is the output of the integrator block of PI_V. Linearizing (5.22)around the operating point gives,

$$\delta\dot{y_V} = k_{IV} \left(\frac{1}{k_{IQ}} \delta\dot{y_Q} - \delta V_{pcc}\right). \tag{5.23}$$

Integrating 5.23 results in

$$\delta y_V = \left(\frac{k_{IV}}{k_{IQ}}\right) \delta y_Q - k_{IV} T_s \delta V_{pcc} - k_{IV} \Delta V_{pcc0}, \tag{5.24}$$

where, T_s is the one sample time for integration, generated from the linearized term of integral function and ΔV_{pcc0} is the change in the PCC voltage during one sample at the operating point.

The voltage amplitude input to the PWM generator is expressed as,

$$V = y_V + k_{PV} \left(\Delta V + V_n - V_{pcc}\right), \tag{5.25}$$

which is linearized as,

$$\delta V = \delta y_V + k_{PV}\left(-m_Q\left(\delta Q + \delta y_Q\right) - \delta V_{pcc}\right). \tag{5.26}$$

Substituting (5.24) in (5.26) generates,

$$\delta V = \left(\frac{k_{IV}}{k_{IQ}}\right)\delta y_Q - k_{IV}T_s\delta V_{pcc} - k_{IV}\Delta V_{pcc0} - m_Q k_{PV}\left(\delta Q + \delta y_Q\right) - k_{PV}\delta V_{pcc}. \tag{5.27}$$

Here, k_{PV} and k_{IV} are the proportional and integral gain parameter of PI_V.
Linearizing (5.16) and (5.17) and substituting the values of $\delta\theta = \delta y_\theta$ from (5.21) and δV from (5.27) results in,

$$\begin{aligned}\delta v_q = &-V_0 sin\left(\theta_0\right)\left(\frac{1}{k_{IP}}\right)\delta y_P + cos\left(\theta_0\right)\left(\frac{k_{IV}}{k_{IQ}}\right)\delta y_Q - k_{IV}T_s cos\left(\theta_0\right)\delta V_{pcc}\\ &-k_{IV}cos\left(\theta_0\right)\Delta V_{pcc0} - m_Q k_{PV}cos\left(\theta_0\right)\left(\delta Q + \delta y_Q\right) - k_{PV}cos\left(\theta_0\right)\delta V_{pcc},\end{aligned} \tag{5.28}$$

and

$$\begin{aligned}\delta v_d = &-V_0 cos\left(\theta_0\right)\left(\frac{1}{k_{IP}}\right)\delta y_P - sin\left(\theta_0\right)\left(\frac{k_{IV}}{k_{IQ}}\right)\delta y_Q + sin\left(\theta_0\right)k_{IV}T_s\delta V_{pcc}\\ &+k_{IV}sin\left(\theta_0\right)\Delta V_{pcc0} + m_Q k_{PV}sin\left(\theta_0\right)\left(\delta Q + \delta y_Q\right) + k_{PV}sin\left(\theta_0\right)\delta V_{pcc}.\end{aligned} \tag{5.29}$$

Here, θ_0 is the angle at the operating point. Linearizing (5.7) and (5.8) gives

$$\delta\dot{y_P} = -\left(m_P k_{IP}\right)\delta P - \left(m_P k_{IP}\right)\delta y_P, \tag{5.30}$$

and

$$\delta\dot{y_Q} = -\left(m_Q k_{IQ}\right)\delta Q - \left(m_Q k_{IQ}\right)\delta y_Q. \tag{5.31}$$

Finally, the linearized active and reactive power terms, δP and δQ can be obtained from,

$$\delta P = \left(3/2\right)V_{qpcc0}\delta i_q + \left(3/2\right)I_{q0}\delta v_{qpcc}, \tag{5.32}$$

and

$$\delta Q = (3/2)\, V_{qpcc0}\delta i_d + (3/2)\, I_{d0}\delta v_{qpcc}. \tag{5.33}$$

As observed in (5.21), a linear relationship can be formed between $\delta\dot{y_\theta}$ and $\delta\dot{y_P}$. Similarly, a linear relationship exists between $\delta\dot{y_V}$ and $\delta\dot{y_Q}$, see (5.23). The state variables, $\dot{\theta}$ and $\dot{y}_V$, are linearly dependent on the state variables, $\dot{y}_P$ and $\dot{y}_Q$, respectively, and hence, can be removed from the state-space equations. The linearized voltage, δV_{pcc} can be expressed as δv_{qpcc} and $\delta v_{dpcc} = 0$, , referring from the PCC voltage, where δv_{qpcc} and δv_{dpcc} are the q and d axis components of the voltage.

The state-space model is developed from combining (5.13), (5.14) and (5.27)−(5.33), and can be expressed as,

$$\frac{d}{dt}\begin{bmatrix}\delta i_q\\ \delta i_d\\ \delta y_P\\ \delta y_Q\end{bmatrix} = \begin{bmatrix}a_{11}^R & a_{12}^R & a_{13}^R & a_{14}^R\\ a_{21}^R & a_{22}^R & a_{23}^R & a_{24}^R\\ a_{31}^R & a_{32}^R & a_{33}^R & a_{34}^R\\ a_{41}^R & a_{42}^R & a_{43}^R & a_{44}^R\end{bmatrix}\begin{bmatrix}\delta i_q\\ \delta i_d\\ \delta y_P\\ \delta y_Q\end{bmatrix} + \begin{bmatrix}b_1^R\\ b_2^R\\ b_3^R\\ b_4^R\end{bmatrix}\delta v_{qpcc}. \tag{5.34}$$

The matrix elements of (5.34) are available in Appendix A.3.

Fig. 5.4(a)-(f) shows the root locus for different parameter variation of the developed controller, represented by (5.34). Notice that, the system has four eigenvalues, λ_{1-4}. The initial points for all eigenvalues are marked with the red crosses on Fig. 5.4. In Fig. 5.4(a), the eigenvalues are plotted for active power injection from 0 to 20 kW when the restoration paths are enabled. All eigenvalues are on the left-half plane for the given power range, which indicates that the system is stable under such active power loading. Figs. 5.4(b)-(f) shows the root locus of the eigenvalues for a fixed, i.e., 20 kW in the simulation presented in this dissertation, active power injection, while different controller parameters are varied. The restoration gain parameters, k_{IP} and k_{IQ} are varied from 10 to 1000 each and the eigenvalues are shown in Figs. 5.4(b)-(c). It is observed that, k_{IP} and k_{IQ} does not have any significant impact on the system's stability when the restoration is performed. The impact of changing the gain parameters of PI_V are shown in Figs. 5.4(d)-(e), where k_{PV} is varied from 0 to 1

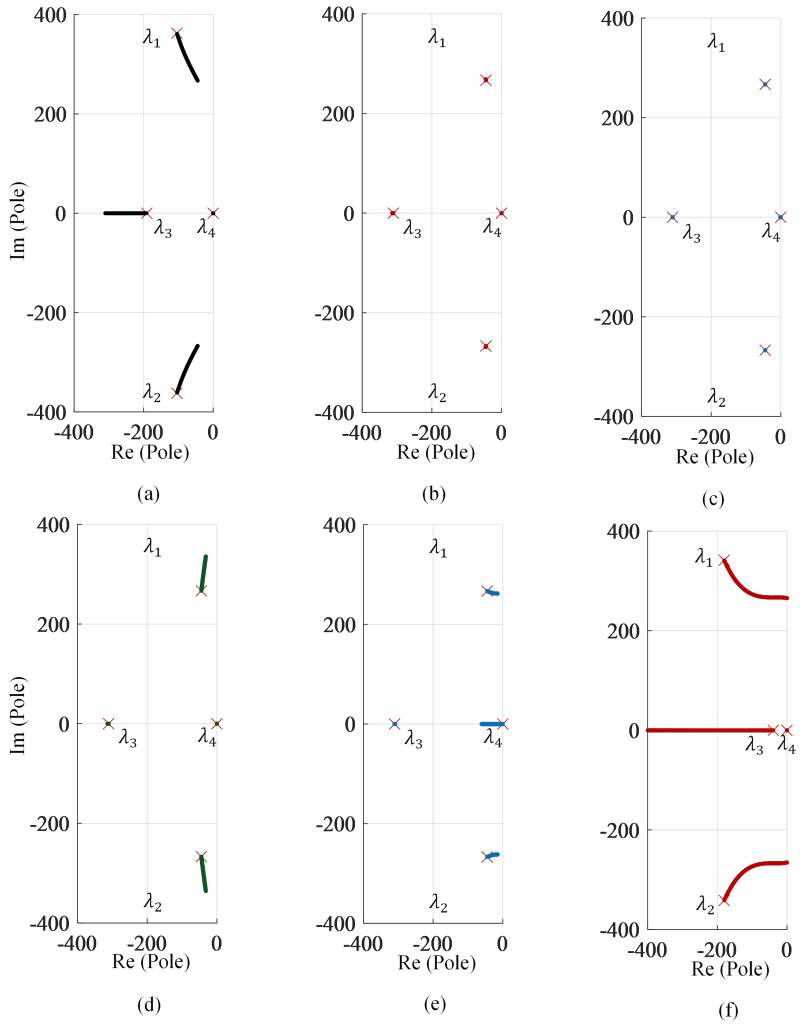

Figure 5.4: *Root locus of the GFM inverter with the developed controller for frequency and voltage restoration; (a) Active power varied from* 0 *to* 20 *kW with* $k_{IP} = 250$, $k_{IQ} = 200$, $k_{PV} = 0.0005$, $k_{IV} = 0.25$, $m_P = 0.005$ *and* $m_Q = 0.001$. *(b)* k_{IP} *varied from* 10 *to* 1000 *at* $P = 20$ *kW, (c)* k_{IQ} *varied from* 10 *to* 1000 *at* $P = 20$ *kW, (d)* k_{PV} *varied from* 0 *to* 1 *at* $P = 20$ *kW, (e)* k_{IV} *varied from* 0 *to* 100 *at* $P = 20$ *kW, (f)* m_P *varied from* 0.001 *to* 0.01 *at* $P = 20$ *kW*.

and k_{IV} is varied from 0 to 100. Finally, the active power-frequency droop parameter, m_P, is varied from 0.001 to 0.01. It can be depicted from Figs. 5.4(d) and 5.4(e) that, a carelessly chosen k_{PV} or k_{IV} value can lead to instability. The droop gain parameter, m_P, has a very significant impact on the system's stability, see Fig. 5.4(f). If the reactive power flow is low, the impact of m_Q remain insignificant, and therefore, the analysis is not presented. Nevertheless, similar eigenvalue characteristics should be expected in systems where high

reactive power flow exists. Table 5.1 presents the system and the control parameters used for the simulation and hardware experiments in this chapter.

Table 5.1: *Parameter Values for Simulation and Experiment.*

Parameters	Values
Nominal line-line voltage, V_n	208 V
DC bus voltage, V_{dc}	350 V
Nominal frequency, ω_n	$2\pi(60)$ rad/s
PWM switching frequency	5 kHz
Inverter side inductor	1.0 mH
PCC side inductor	0.5 mH
Filter capacitor (in Δ)	5 μF
Filter damping resistor (in Δ)	1.65 Ω
Frequency-active power droop, m_P	0.005
Voltage-reactive power droop, m_Q	0.001
Frequency restoration gain, k_{IP}	250
Voltage restoration gain, k_{IQ}	200
PI_V integrator gain, k_{IV}	0.25
PI_V proportional gain, k_{PV}	0.0005
Tie-line resistance, R_{line}	1 Ω
Tie-line inductance, L_{line}	5 mH

5.4 Experiment Results

In this section, the restoration controller is verified for single and two inverter scenarios. A part of the three-phase microgrid setup, as shown in Fig. 2.6 in Chapter 2, is used for verifying the developed controller for restoration. The test setup consists of two inverters as $Inv1$ and $Inv2$, a tieline between the inverters, a resistive load and circuit breakers to connect and disconnect the inverters. The circuit and controller parameters, used for the testing, are presented in Table 5.1. In the following, several test scenarios are investigated with the restoration paths at different gain values. The restoration paths in Fig. 5.1 can be enabled/disabled by using a timer also [126], whereas, in the developed method the enable/disable control is threshold-based, see Fig. 5.3. The timer-based method is considered as the benchmark to demonstrate the superiority of the developed threshold-base method.

5.4.1 Frequency and Voltage Restoration for a Single Inverter

In this subsection the performance of the developed frequency and voltage restoration control path under load variation is investigated for a single inverter operation. Both timer-based method and threshold-based methods are used to control the restoration paths to show the superior performance of the threshold-based restoration controller.

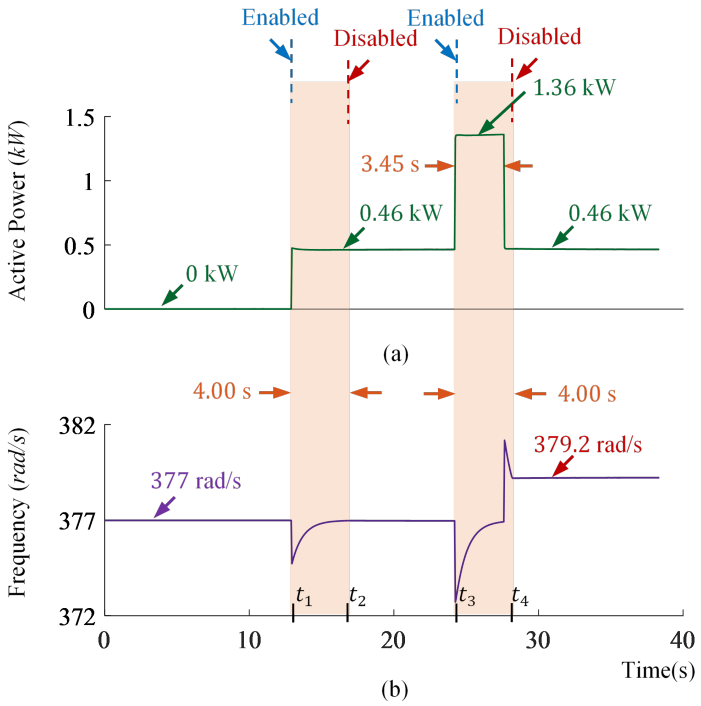

Figure 5.5: *Experiment results showing the performance of the timer-based restoration controller for frequency restoration during load change events; (a) active power injection, (b) frequency of the inverter output voltage.*

Fig. 5.5 shows the performance of the timer-based frequency restoration method when the resistive load connected to the system is varied. The active power injected by the inverter is shown in Fig. 5.5(a). Fig. 5.5(b) shows the frequency of the inverter's output voltage. The inverter is initially operated at 0 kW with droop control activated.. Therefore, the initial frequency is at 377 rad/s. Then a resistive load of 0.46 kW is added at at $t_1 = 12.9\ s$, resulting in the drop in the frequency due to the droop control. Notice in Fig. 5.5, that the active power change is immediately detected by the controller and the restoration path is enabled, gradually restoring the frequency from 374.7 rad/s to 377 rad/s. In this test, the

restoration path is enabled for 4 s with a pre-set timer as is disabled at $t_2 = 16.9$ s, i.e., the restoration controller is disabled after 4 s of operation. In the second event, a resistive load of 1.36 kW is first switched on at $t_3 = 24.2$ s and then switch of after 3.45 s. However, the restoration is active only for 4 s after detecting the load change at t_3 and disabled the restoration at $t_4 = 28.2$ s. As observed in Fig. 5.5(b), restoration controller is able to respond to the load change at t_3 and starts restoring the frequency. However it fails to detect when the load is switched off and the frequency changed again due to droop. Therefore, when the restoration control is disabled at t_4, the restoration remains incomplete, resulting in an incorrect system frequency, i.e., 379.2 rad/s in this test. The test shows that, despite showing good restoration performance, the timer-based control can be unreliable for rapid switching of loads.

The previous test is repeated to demonstrate the performance of the threshold-based method for frequency restoration under same load change events. Fig. 5.6 shows the active power injection and the frequency of the output voltage of the inverter under test. Fig. 5.6(a) shows that the resistive load is changed to 0.46 kW at $t_5 = 12.3$ s, then to 1.36 kW at $t_7 = 24.7$ s, and then again to 0.46 kW at 27.95 s. The restoration control paths are enabled at the detection of load changes, i.e., at t_5 and t_7. Then, the restoration control is disabled when the frequency reaches near 377 rad/s. Notice in Fig. 5.6(b) that, the control paths are enabled for different time-spans in threshold-based method, i.e., restoration operation for the first load change scenario at t_5 is disabled at $t_6 = 15.3$ s after 3 s and the restoration operation for the second load change scenario at t_7 is disabled at $t_8 = 32.7$ s after 8 s. The threshold-based method ensure that the restoration control is enabled until the restoration is achieved. Therefore, the developed method is able to restore the frequency to 377 rad/s regardless of the narrow pulse loads and under the same load-change scenario where the timer-based method fails.

The performance of the timer-based method for voltage amplitude restoration is shown in Fig. 5.7. This test is performed with $m_Q = 0.1$ and $k_{IQ} - 20$ in order to show the voltage variation with the limited reactive load available in the laboratory. The remaining parameters are same as in Table 5.1. To allow the voltage amplitude to freely vary within

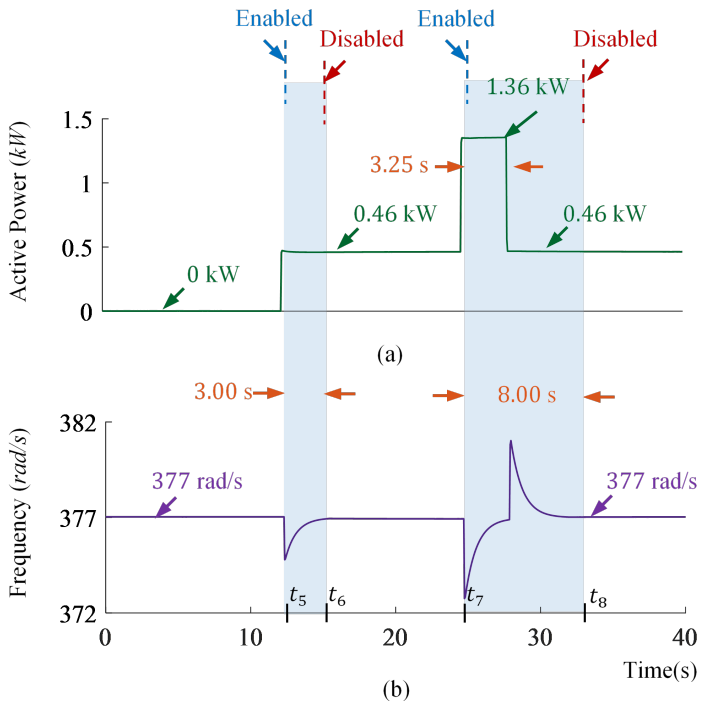

Figure 5.6: *Experiment results showing the performance of the threshold-based restoration controller for frequency restoration during load change events; (a) active power injection, (b) frequency of the inverter output voltage.*

the acceptable range to accommodate the reactive power-flow, a tolerance for the voltage between 293.5 V and 294.5 V is considered in this dissertation. Therefore, voltage restoration to an exact nominal value, i.e. $\sqrt{2}\,(208) = 294.15\ V$, is purposefully prevented. In this test, the reactive load is set to 0 Var at $t = 0\ s$. Then the reactive load is increased to 24.5 Var at $t_1 = 30\ s$, see Fig. 5.7(a), which reduced the voltage. The restoration controller detects the load change and enabled the voltage restoration path for a pre-set time of 20 s and the voltage amplitude is restored to 293.5 V, which is the lower boundary of the predetermined band for acceptable voltage. Then at $t_3 = 60\ s$, the reactive load is increased to 195.5 Var only for 10 s and set to 24.5 Var after that. Fig. 5.7(a) shows that, the this incident happens when the restoration process that is started at t_3 is still active. Therefore, the voltage restoration remain incomplete for the reactive load change at t_3 and the voltage swells to 299.5 V, which is not an acceptable voltage.

Fig. 5.8 shows the performance of the threshold-based restoration control under the

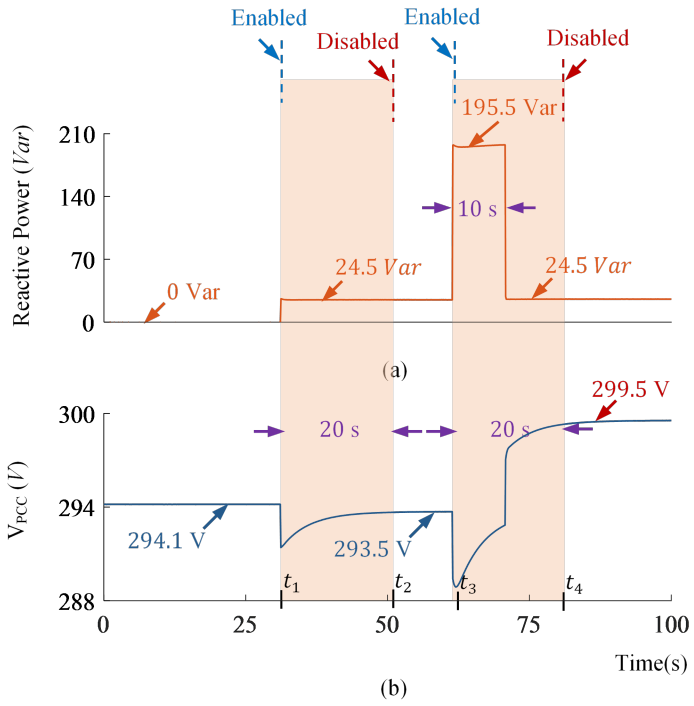

Figure 5.7: *Experiment results showing the performance of the timer-based restoration controller for voltage restoration during load change events; (a) reactive power injection, (b) inverter output voltage.*

similar reactive load change scenario as in Fig. 5.7. In this test case, the reactive load is first set to 24.5 Var at $t_5 = 30$ s from 0 V, and then a pulse load of 195.5 Var at 10 s duration is set at $t_7 = 60$ s, see Fig. 5.8(a). Fig. 5.8(b) shows that voltage amplitude is successfully restored to 293.5 V and 294.5 V after 15 s and 35 s, respectively with the threshold-based controller. This test shows that the threshold-based controller can properly restore the voltage amplitude in all load change situation, whereas the timer-based method may fail.

5.4.2 Frequency Restoration in Microgrid of Two GFM Inverters

In this subsection, the developed GFM inverter controller with frequency restoration control is experimentally verified with the timer-based control and the threshold-based control under plug-in of new inverter and load change scenarios in a laboratory-scale microgrid, including a three-phase variable resistive load that is fed by two droop-controlled inverters. Figs. 5.9

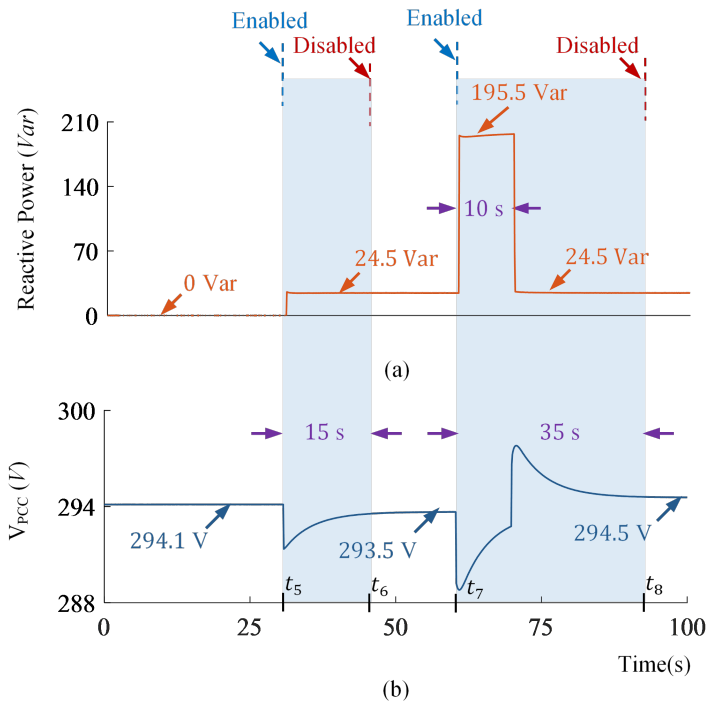

Figure 5.8: *Experiment results showing the performance of the threshold-based restoration controller for voltage restoration during load change events; (a) reactive power injection, (b) inverter output voltage.*

and 5.10 demonstrates the performance of the timer-based and threshold-based controller. For both test scenarios, the first inverter, $Inv1$ feeds a load of 0.46 kW in stand-alone, and then the second inverter, $Inv2$ is connected to the system in GFM mode. Then, two load change events are introduced. Notice that, the plug-in and the load-change events are similar to the test performed in Chapter 2 for synchronization and power-sharing. One important difference in this chapter is, here $Inv1$ is operating at 377 rad/s and without the restoration controller developed in this chapter, $Inv2$ cannot contribute to power-sharing after synchronization and the frequency is always restored to nominal value whenever the load change occurs.

Fig. 5.9(a) shows the synchronization and power-sharing between $Inv1$ and $Inv2$, that are in GFM modes and equipped with the timer-based restoration controller. Fig. 5.9(b) shows the system frequency. Here, $Inv1$ is initially operating in standalone mode with 0.46 kW resistive load. $Inv2$ is connected to the system without contribute to power-sharing. Then,

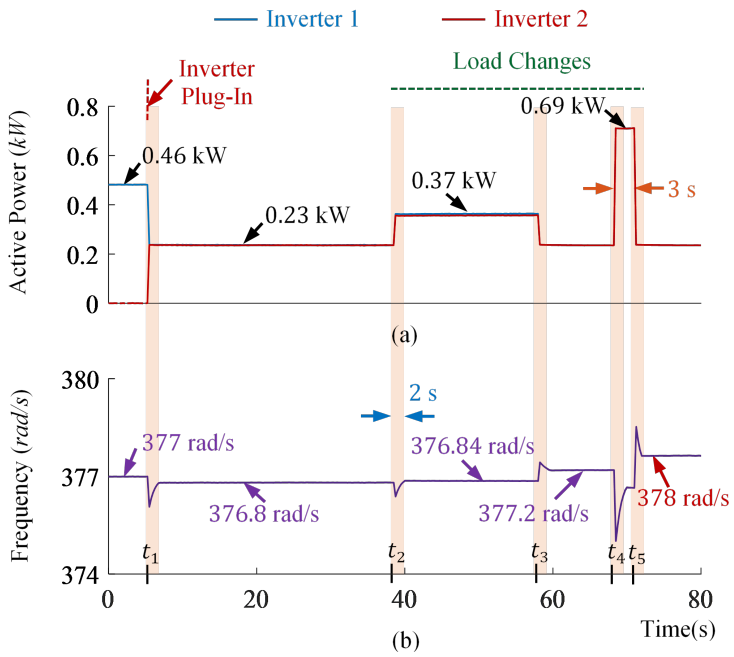

Figure 5.9: *Performance verification of the frequency restoration with timer-based control at plug-in and load change events in microgrid with GFM inverters; (a) active power injected by the inverters, and (b) system frequency.*

at $t_1 = 5.5\ s$, $Inv2$ is connected to form the microgrid and equally share the load, where each inverter injects 0.23 kW. Notice that, the frequency is drops immediately at t_1 and the restoration is enabled. Then, after a pre-set time of 2 s, the restoration is disabled. The orange highlights on Fig. 5.9 indicates the time when the restoration paths are enabled. The total load is increased to 0.74 kW at $t_2 = 40\ s$ and then reduced to 0.46 kW at $t_3 = 60\ s$. Then, a narrow pulse load of 1.38 kW is added at $t_4 = 70\ s$ that lasted for only 3 s. As observed in Fig. 5.9(b), the 2 s time for restoration is not sufficient to restore the frequency, and therefore, the frequency is incorrectly settling at values slightly different from 377 rad/s. Particularly, for the pulse load, the error is more as due to the two consecutive high load change in insufficient time, the frequency settles at 378 rad/s.

The performance of the developed threshold-based restoration Controller is shown in Fig. 5.10 under the same scenario as tested for the timer-based method. In this scenario, two inverters are synchronized and connected at t_6 in the same manner and then the load is changed to 0.74 kW at $t_7 = 28\ s$, to 0.46 kW again at $t_8 = 28\ s$, to 1.38 kW at $t_70\ s$,

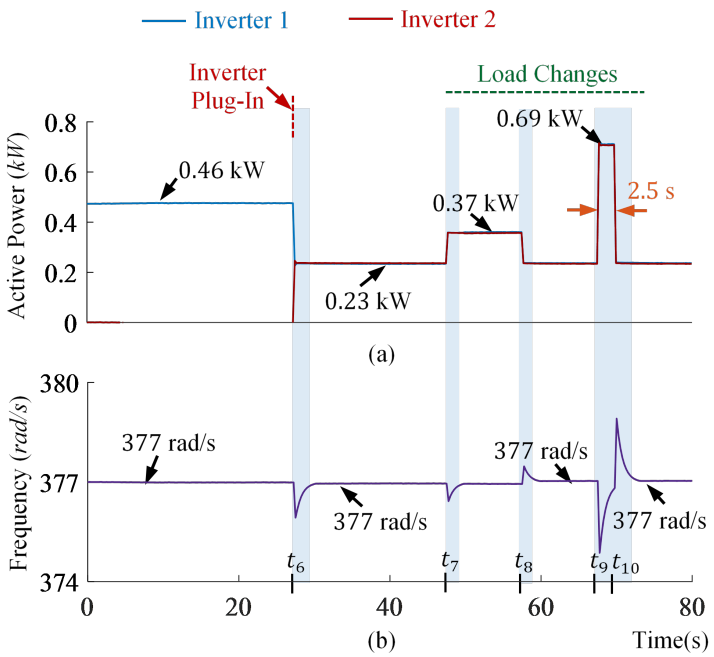

Figure 5.10: *Performance verification of the frequency restoration with threshold-based control at plug-in and load change events in microgrid with GFM inverters; (a) active power injected by the inverters, and (b) system frequency.*

and to 0.46 kW again at $t_10 = 72.5$ s, see Fig. 5.10(a). Fig. 5.7(b) shows the frequency of the system, where it is observed that the threshold-based method can restore the frequency to 377 rad/s after the plug-in and loading events. Particularly, unlike the timer-based method, the threshold-based method is able to successfully restore the frequency after the pulse loading event, This test proves that the developed threshold-based restoration control provides superior performance that the timer-based method.

5.4.3 Restoration Gain Parameters and Power-Sharing

As stated in Section 5.2, power-sharing between two GFM inverter can be impacted by the restoration gain parameters, k_{IP}, if the values are inaccurately selected, and the power-sharing and the restoration process are not coordinated. Section 5.2 also mathematically shows that, the term, $m_P k_{IP}$, must have to be equal in all connected inverters to ensure same timing for the completion of operation. In this subsection, the impacts of k_{IP} value on the power-sharing between two inverters are investigated for two set of scenarios.

In the first test, k_{IP} of $Inv1$ is set to 250, while the k_{IP} of $Inv2$ is set to 250, 300, 350, 400, 450, and 500, separately. For each pair of values, the load is changed from 0.74 kW to 0.46 kW, while both inverters are contributing to the load. Fig. 5.11(a)-(c) shows the power-sharing scenarios for the inverters for three of the six tested mentioned scenarios. Notice that, the error is increasing as the restoration time decreases due to increase in the k_{IP} value of $Inv2$.

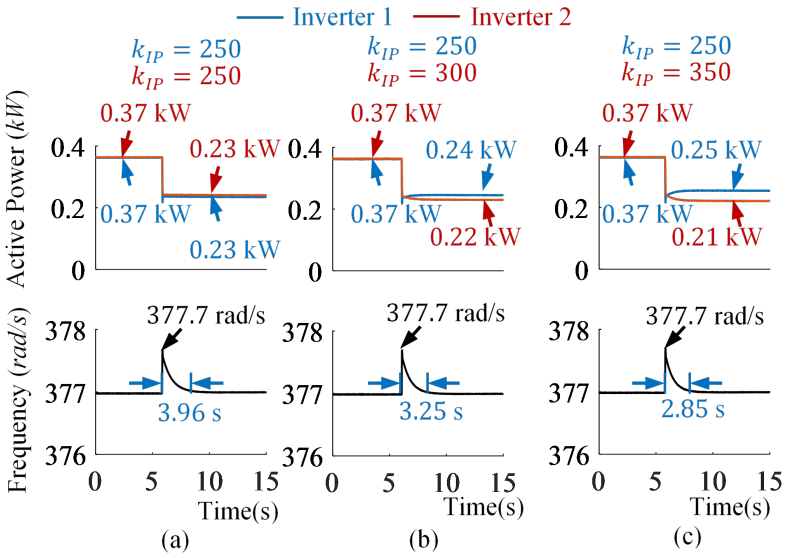

Figure 5.11: *Impact on restoration time and power-sharing between two inverters for $Inv2$'s k_{IP} values of (a)* 250*, (b)* 300*, and (c)* 350*, while $Inv1$'s k_{IP} is* 250*.*

Fig. 5.12 plots the restoration time and the percentage of error in power-sharing between the two inverters as the ratio between the k_{IP} of $Inv2$ to $Inv1$ increases. Fig. 5.12(a) shows the restoration time is the maximum when the two inverters have the same k_{IP} values and as the ratio between the k_{IP} of $Inv2$ to $Inv1$ increases, the restoration time decreases. Fig. 5.8(b), on the other hand, shows the error in power-sharing increases as the ratio between the k_{IP} of $Inv2$ to $Inv1$ increases.

In the second test, two different restoration gain parameters, k_{IP}, values are used for the two inverters, i.e., $k_{IP} = 250$ for $Inv1$, and $k_{IP} = 500$ for $Inv2$. Then the droop gain parameters, m_P are chosen such that the terms $m_P k_{IP}$ are equal for the two inverters, i.e., $m_P = 0.0005$ for $Inv1$, and $m_P = 0.00025$ for $Inv2$. The active power-sharing at the load

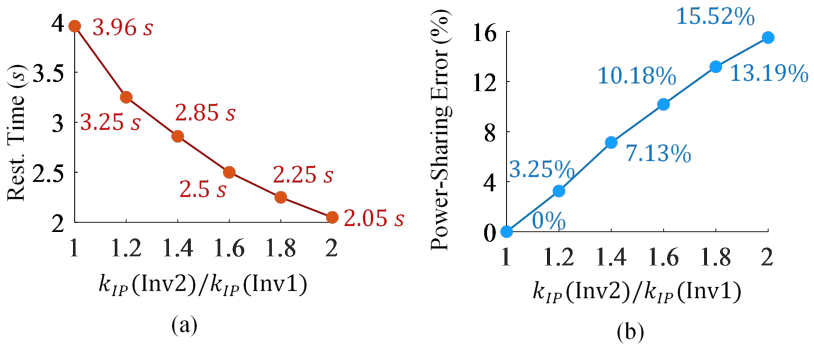

Figure 5.12: *Experimental results showing the restoration time and the error between power-sharing when k_{IP} $(Inv1)$ is* 250 *and k_{IP} $(Inv2)$ varies as* 250, 300, 350, 400, 450, *and* 500, *and when m_P of the two inverters are* 0.0005*; (a) measured restoration time, and (b) percentage error for desired power-sharing.*

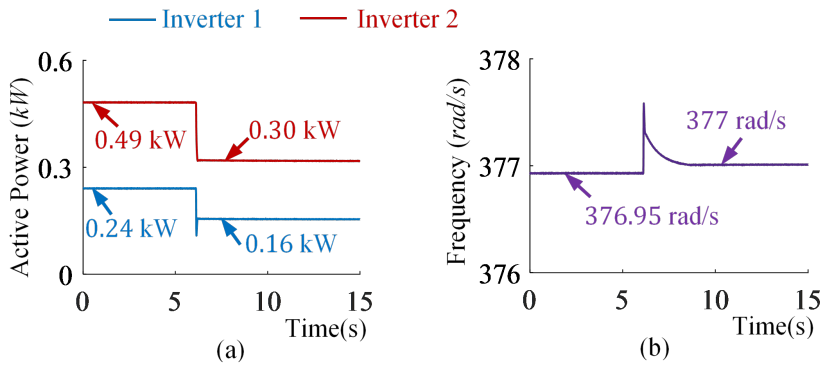

Figure 5.13: *Demonstration of* 2 : 1 *power-sharing between two inverters by selecting $m_P k_{IP}$ values for* 2 : 1 *droop coefficient; (a) active power injected by the inverters, and (b) system frequency.*

of 0.74 kW and 0.46 kW are shown in Fig. 5.13(a), while the system frequency is shown in Fig. 5.13(b). Notice that the power-sharing ratio between the two GFM inverters is 2 : 1 as dictated by the droop gain parameters. Therefore, that fact that $m_P k_{IP}$ term for all the inverters need to be equal is proven through these two experiments.

5.4.4 Selection of ε_P for Restoration Algorithm

In this test scenario, the impact of the threshold value of ε_P on the frequency restoration operation is demonstrated through two experiments with two different ε_P values in a single inverter with frequency restoration controller. For both cases, the load is first set to 0.25 kW

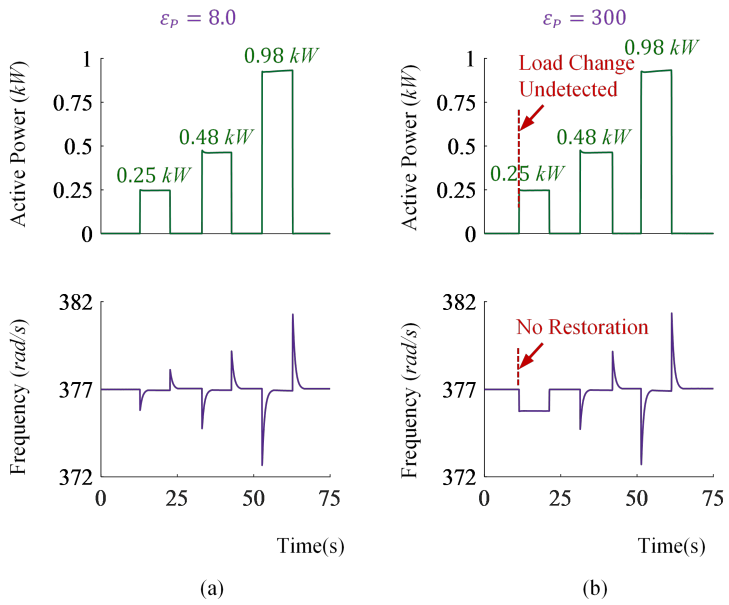

Figure 5.14: *Performance of the frequency restoration controller in an inverter at (a)* $\varepsilon_P = 8.0$*, and (b)* $\varepsilon_P = 300$ *under different load change scenarios.*

from 0 kW for 10 seconds and then reduced to 0 kW, then set to 0.48 kW for 10 seconds and then reduced to 0 kW, and finally set to 0.98 kW for 10 seconds and then reduced to 0 kW. Fig. 5.14(a) shows active power variation and the system frequency for $\varepsilon_P = 8.0$. As observed in Fig. 5.14(a)-bottom, the frequency restoration controller is enabled for each load variation. Fig. 5.14(b) shows active power variation and the system frequency for $\varepsilon_P = 300$. Here, the frequency reduced from the nominal value due to 0.25 kW of load change, but the restoration operation has not been enabled by the algorithm in Fig. 5.1 as the threshold value is bigger than the change in the active power injection, thus remaining undetected. Therefore, it is necessary to keep the threshold value ε_P as low as possible and lower bounded by the relationship in (5.11). Similar conclusion can be drawn for ε_Q, which must be as low as possible and lower bounded by the relationship in (5.12).

Fig. 5.15 shows a picture of the test setup during verification of the threshold-based frequency restoration controller.

Figure 5.15: *Experimental verification of the threshold-based frequency restoration controller.*

5.5 Conclusion

In this chapter, a threshold-based frequency and voltage restoration method have been developed for GFM inverters with droop-control. The restorations have been accomplished by two feedback paths controlled by the developed control algorithm. The efficacy of the developed controller for restoration has been verified for plug-in and load change events through hardware experiments. Stability of the developed controller under different loading and parameter variation conditions has been studied through developing the closed-loop state-space model with a GFM inverter. Finally, the developed method with threshold-based control has been compared with a timer-based control. The following points can be highlighted as summary.

- The frequency and the voltage restoration paths controlled by the threshold-based method have shown accurate performances in restoration, whereas the timer-based method has failed.

- The restoration paths has been enabled only after detecting a load change. The dynamics of power-sharing between the inverters have been ensured faster than the restoration control to maintain proper power-sharing and frequency and voltage restoration.

- The frequency and the voltage control paths have been independently operated and the threshold-based method has not restricted by the number of inverters in a microgrid.

- It has found from the stability analysis on the state-space model that, adding the feedback controller for the restoration has not negatively impact the stability of the inverter.

- Frequency and voltage restoration has been found useful when the parameter deviation due to a load change has been significant, particularly in an islanded microgrids fed by only few inverters

Chapter 6

Conclusion and Suggestions for Future Work

This chapter summarizes this dissertation's content and highlights this work's contribution. This chapter is divided into two sections. The summary of the dissertation and the contributions are presented in Section 6.1. Some suggestions for possible future work are discussed in Section 6.2.

6.1 Summary and Contributions

In this dissertation, new controls have been developed to resolve the technical challenges for restoration and universal operation of the GFM inverters in a system with multiple inverters. The basic GFL and GFM controls and the role of a GFM inverter in future power grid have been discussed in Chapter 1. As has been discussed, the GFM inverters can be operated independently. However, operating multiple GFM inverters can cause instability due to improper synchronization and decentralized power-sharing, particularly when an inverter needs to operate universally in GFM and GFM modes with seamless switching capabilities. Also, the voltage and frequency deviation caused by decentralized power-sharing may trip the GFM inverters. Furthermore, the state-of-the-art phase-angle detection methods do not have

reliable solutions for operating an inverter in the asymmetrical microgrid. The shortcomings of the existing state-of-the-art techniques regarding the above-mentioned issues and the necessity for new methods to improve the universal operation capability and restoration features for the GFM inverters, along with seamless synchronization, power-sharing, and phase-angle detection under asymmetrical conditions, have been emphasized in Chapter 1.

Two inverter synchronization and power-sharing methods, named the output-sync method and the controller-sync method, have been analyzed and verified in Chapter 2. With the output-sync method, the GFM inverter has been able to synchronize the inverter output voltages, i.e., match the amplitude, phase-angle, and frequency with the microgrid and then connect to the system. The output-sync method has been implemented with both droop and virtual inertia control for power-sharing between multiple inverters in GFM mode. On the contrary, the controller-sync method can run two control paths in parallel while keeping the paths synchronized with each other and can seamlessly switch the controller to GFM mode. It has been shown that the controller-sync method has a remarkable capability to connect to the system without even injecting any power and requires only one set of sensors for synchronization. Also, the controller-sync method can establish power-sharing with other inverters using droop or virtual-inertia control without entering the GFM control mode. A state-space analysis has been presented, ensuring the stability of the controller-sync method before and after the controller switch. Both methods have been verified for synchronization and power-sharing scenarios through hardware experiments in a two-inverter microgrid testbed.

In Chapter 3, a novel signal reformation-based direct phase-angle detection (DPD-SR) method has been developed for phase-angle estimation in asymmetrical grid conditions. The developed method has shown accurate performance in phase-angle estimation under simultaneous voltage and phase-angle asymmetry. The signal reformation method has been developed to generate three-phase symmetrical signals from two asymmetrical signal measurements. The direct phase-angle detection method has been developed to estimate the phase-angle directly using trigonometric function. Remarkably, only two line-line voltage measurements have been used compared to the three measurements required in state-of-

the-art approaches. The developed method has not used any closed loop PI, filters, or decoupling cell to purify the positive and negative sequence components for obtaining the phase-angle of an asymmetrical system. Furthermore, the developed DPD-SR has shown superior performance with its simple and straightforward structure in comparison to the SRF and DDSRF-PLL. The performance of the developed method has been verified in a hardware test bed with an inverter and a grid emulator under asymmetrical conditions. The developed DPD-SR method is used in all the controllers presented in this dissertation.

A universal controller to operate an inverter in both GFL and GFM mode has been developed in Chapter 4. The universal controller has been developed by modifying the controller-sync method in Chapter 4 for improved operational capability. With the universal controller, the inverter has been made able to operate in grid-connected, i.e., GFL, mode when the microgrid is present. As has been shown in Chapter 4, the universal controller has enabled the inverters to seamlessly switch to GFM mode after an islanding detection while maintaining power-sharing in proportion to the inverter's capacity. Furthermore, the universal control has allowed the inverter to synchronize with a grid in GFL mode and with an islanded microgrid in GFM mode. A detailed small-signal analysis has been presented to show the stability of the inverters at each mode of operation. The efficacy of the controller has been tested using a two-inverter microgrid setup in both grid-connected and islanded modes.

A voltage and frequency restoration method has been developed in Chapter 5. The restoration has been achieved by adding feedback control paths to the universal inverter controller developed in Chapter 4. A novel control method has been developed to enable the restoration paths by measuring the voltage and frequency parameters only when a load change or plug-in of an inverter is detected. The control paths are disabled once the restoration is performed. As has been shown, the restoration path can be controlled and can either be made timer/counter-based or threshold-based. However, the timer-based method may produce inaccurate restoration, which has been completely eliminated by the threshold-based method. A state-space model has been developed to show the stability of the inverter at different load and control parameter variations. It has been shown with analysis that

the restoration control paths have to be slower than the power-sharing controls to ensure both power-sharing and restoration capabilities in decentralized mode. The developed control method has been verified for voltage and frequency restoration through a two-inverter microgrid.

In conclusion, a novel universal controller for inverters in GFL and GFM mode, with synchronization, decentralized power-sharing, and voltage and frequency restoration capability, has been developed. In addition, the phase-angle detection capability of the inverter under asymmetrical conditions has been enhanced by developing a new signal reformation-based direct phase-angle detection method. All controllers have been verified in hardware setup, equipped with inverters, loads, and grid-emulator. The developed methods are well suited to be implemented for practical applications for inverters in grid-connected and islanded operations.

6.2 Suggestion for Future Work

The efficacy of the inverter controller developed in the dissertation is thoroughly validated through simulation and hardware experiments in a microgrid with multiple inverters under different scenarios. Nevertheless, the developed controller opens the door for more research. Following suggestions are recommended for the future work.

- The output-sync and the controller-sync method presented in this chapter can be used as bases for power-electronics converter synchronization in AC-DC, DC-DC, and DC-DC applications, where seamless and independent control is expected at high switching frequency [50, 127, 128]. Particularly for high-speed application, adaptive tuning controller can also be developed to provide fast synchronization.

- The DPD-SR method presented in Chapter 3 can be used in applications where the frequency can vary within a wide range [129, 130], i.e., in electric vehicles [131] and more electric aircrafts [132]. The classical PLLs are not suitable for these applications as the PLLs are tuned for the operating frequency and have bandwidth due to the

closed-loop structure.

- The universal controller in Chapter 4 can also be extended for inertia-based systems. Particularly, in a microgrid with large inductive machine loads, maintaining the stability of the system is difficult [133]. The state-space model analysis presented for the universal controller can be developed for such systems for detailed stability analysis [134].

- The developed universal controller can also be extended for current source inverters, typically used for direct-drive wind turbines [135, 136].

- The threshold-based restoration control in Chapter 5 can also be applied in some other control applications for power electronic converters. For example, the stability controller using smart-load [137] in microgrids can be developed using similar feedback paths with the threshold-based regulation control.

- The impact of closing and opening delays of the circuit breakers on the stability of the universal inverters can be investigated to develop controllers for protection [138–140].

- Inrush current compensation for the inclusion of dynamic and inductive loads in the microgrid can be investigated and developed [141].

Bibliography

[1] B. Mirafzal and A. Adib, "On grid-interactive smart inverters: Features and advancements," *IEEE Access*, vol. 8, pp. 160 526–160 536, Sept. 2020.

[2] J. Benzaquen, M. Miranbeigi, P. Kandula, and D. Divan, "Collaborative autonomous grid-connected inverters: Flexible grid-forming inverter control for the future grid," *IEEE Electrific. Mag.*, vol. 10, no. 1, pp. 22–29, Mar. 2022.

[3] S. Xu, Y. Xue, and L. Chang, "Review of power system support functions for inverter-based distributed energy resources- standards, control algorithms, and trends," *IEEE Open J. Power Electron.*, vol. 2, pp. 88–105, Feb. 2021.

[4] R. An, Z. Liu, J. Liu, and B. Liu, "A comprehensive solution to decentralized coordinative control of distributed generations in islanded microgrid based on dual-frequency-droop," *IEEE Trans. Power Electron.*, vol. 37, no. 3, pp. 3583–3598, Mar. 2022.

[5] F. Sadeque and F. Fateh, "Voltage control by transmitter-side measurements for on-board wireless EV battery charger," in *Proc. 2021 IEEE Kansas Power and Energy Conference (KPEC)*, Apr. 2021, pp. 1–6.

[6] M. S. Pilehvar, D. Sharma, and B. Mirafzal, "Forming interphase microgrids in distribution systems using cooperative inverters," *CPSS Trans. Power Electron. Appl.*, vol. 7, no. 2, pp. 186–195, 2022.

[7] S. F. Zarei, H. Mokhtari, M. A. Ghasemi, S. Peyghami, P. Davari, and F. Blaabjerg, "Control of grid-following inverters under unbalanced grid conditions," *IEEE Trans. Energy Convers.*, vol. 35, no. 1, pp. 184–192, Mar. 2020.

[8] A. Singh and B. Mirafzal, "An efficient grid-connected three-phase single-stage boost

current source inverter," *IEEE Power Energy Technol. Syst. J.*, vol. 6, no. 3, pp. 142–151, 2019.

[9] R. H. Lasseter, Z. Chen, and D. Pattabiraman, "Grid-forming inverters: A critical asset for the power grid," *IEEE J. Emerg. Sel. Topics Power Electron.*, vol. 8, no. 2, pp. 925–935, Jun. 2020.

[10] A. Singh, A. K. Kaviani, and B. Mirafzal, "On dynamic models and stability analysis of three-phase phasor PWM-based CSI for stand-alone applications," *IEEE Trans. Ind. Electron.*, vol. 62, no. 5, pp. 2698–2707, May 2015.

[11] B. Mirafzal, M. Saghaleini, and A. K. Kaviani, "An SVPWM-based switching pattern for stand-alone and grid-connected three-phase single-stage boost inverters," *IEEE Trans. Power Electron.*, vol. 26, no. 4, pp. 1102–1111, 2011.

[12] X. Chen, Y. Hou, S.-C. Tan, C.-K. Lee, and S. Y. R. Hui, "Mitigating voltage and frequency fluctuation in microgrids using electric springs," *IEEE Trans. Smart Grid*, vol. 6, no. 2, pp. 508–515, Mar. 2015.

[13] A. Adib, J. Lamb, and B. Mirafzal, "Ancillary services via VSIs in microgrids with maximum DC-bus voltage utilization," *IEEE Trans. Ind. Appl.*, vol. 55, no. 1, pp. 648–645, Jan.-Feb. 2019.

[14] J. Lamb, B. Mirafzal, and F. Blaabjerg, "PWM common mode reference generation for maximizing the linear modulation region of CHB converters in islanded microgrids," *IEEE Trans. Ind. Electron.*, vol. 65, no. 7, pp. 5250–5259, Jul. 2018.

[15] J. Lamb and B. Mirafzal, "An adaptive SPWM technique for cascaded multilevel converters with time-variant DC sources," *IEEE Trans. Ind. Appl.*, vol. 52, no. 5, pp. 4146–4155, 2016.

[16] A. Borrell, M. Velasco, J. Miret, A. Camacho, P. Marti, and M. Castilla, "Collaborative voltage unbalance elimination in grid-connected AC microgrids with grid-feeding inverters," *IEEE Trans. Power Electron*, vol. 36, no. 6, pp. 7189–7201, Jun. 2021.

[17] A. Adib, F. Fateh, M. B. Shadmand, and B. Mirafzal, "A reduced-order technique for stability investigation of voltage source inverters," in *2018 IEEE Energy Conversion Congress and Exposition (ECCE)*, 2018, pp. 5351–5356.

[18] A. Adib, F. Fateh, and B. Mirafzal, "Weak grid impacts on the design of voltage source inverters —virtual inductance," in *2018 IEEE 19th Workshop on Control and Modeling for Power Electronics (COMPEL)*, 2018, pp. 1–6.

[19] B. Mirafzal, *Power Electronics in Energy Conversion Systems*, 1st ed. New York, USA: McGraw Hill, 2022.

[20] R. Rosso, X. Wang, M. Liserre, X. Lu, and S. Engelken, "Grid-forming converters: control approaches, grid-synchronization, and future trends—a review," *IEEE Open J. Ind. Appl.*, vol. 2, pp. 93–109, Apr. 2021.

[21] J. L. Rodríguez-Amenedo, S. A. Gómez, J. C. Martínez, and J. Alonso-Martinez, "Black-start capability of DFIG wind turbines through a grid-forming control based on the rotor flux orientation," *IEEE Access*, vol. 9, pp. 142 910–142 924, Oct. 2021.

[22] B. Pawar, E. I. Batzelis, S. Chakrabarti, and B. C. Pal, "Grid-forming control for solar PV systems with power reserves," *IEEE Trans. Sustain. Energy*, vol. 12, no. 4, pp. 1947–1959, Oct. 2021.

[23] S. Yazdani, M. Ferdowsi, M. Davari, and P. Shamsi, "Advanced current-limiting and power-sharing control in a pv-based grid-forming inverter under unbalanced grid conditions," *IEEE J. Emerg. Sel. Topics Power Electron.*, vol. 8, no. 2, pp. 1084–1096, Jun. 2020.

[24] S. Jena, N. P. Padhy, and J. M. Guerrero, "Cyber-resilient cooperative control of dc microgrid clusters," *IEEE Syst. J.*, vol. 16, no. 2, pp. 1996–2007, Jun. 2022.

[25] *IEEE standard for interconnection and interoperability of distributed energy resources with associated electric power systems interfaces*, IEEE Standard 1547-2018, 2018.

[26] G. Lou, W. Gu, L. Wang, B. Xu, M. Wu, and W. Sheng, "Adecentralised secondary voltage and frequency control scheme for islanded microgrid based on adaptive state estimator," *IET Gener., Transmiss. Distrib.*, vol. 11, no. 15, p. 3683–3693, Oct. 2017.

[27] F. Blaabjerg, R. Teodorescu, M. Liserre, and A. V. Timbus, "Overview of control and grid synchronization for distributed power generation systems," *IEEE Trans. Ind. Electron.*, vol. 53, no. 5, pp. 1398–1409, Oct. 2006.

[28] R. Chilipi, N. A. Sayari, K. A. Hosani, and A. R. Beig, "Control scheme for grid-tied distributed generation inverter under unbalanced and distorted utility conditions with power quality ancillary services," *IET Renew. Power Gener.*, vol. 10, no. 2, pp. 140–149, Feb. 2016.

[29] D. S. Ochs, B. Mirafzal, and P. Sotoodeh, "A method of seamless transitions between grid-tied and stand-alone modes of operation for utility-interactive three-phase inverters," *IEEE Trans. Ind. Appl.*, vol. 50, no. 3, pp. 1934–1941, May-Jun. 2014.

[30] S. Golestan, J. M. Guerrero, and J. C. Vasquez, "A robust and fast synchronization technique for adverse grid conditions," *IEEE Trans. Ind. Electron.*, vol. 64, no. 4, pp. 3188–3194, Apr. 2017.

[31] A. Adib, B. Mirafzal, X. Wang, and F. Blaabjerg, "On stability of voltage source inverters in weak grids," *IEEE Access*, vol. 6, pp. 4427–4439, Jan. 2018.

[32] T. Stetz, F. Marten, and M. Braun, "Improved low voltage grid-integration of photovoltaic systems in germany," *IEEE Trans. Sustain. Energy*, vol. 4, no. 2, pp. 534–542, 2013.

[33] J. Lamb and B. Mirafzal, "Grid-interactive cascaded H-bridge multilevel converter PQ plane operating region analysis," *IEEE Trans. Ind. Appl.*, vol. 53, no. 6, pp. 5744–5752, Nov.-Dec. 2017.

[34] R. Kabiri, D. G. Holmes, and B. P. McGrath, "Control of active and reactive power

ripple to mitigate unbalanced grid voltages," *IEEE Trans. Ind. Appl.*, vol. 52, no. 2, pp. 1660–1668, Mar.-Apr. 2016.

[35] F. Nejabatkhah, Y. W. Li, and B. Wu, "Control strategies of three-phase distributed generation inverters for grid unbalanced voltage compensation," *IEEE Trans. Power Electron., vol.*, vol. 31, no. 7, pp. 5228–5241, Jul. 2016.

[36] Y. A.-R. I. Mohamed and E. F. El-Saadany, "A control method of grid-connected PWM voltage source inverters to mitigate fast voltage disturbances," *IEEE Trans. Power Syst.*, vol. 24, no. 1, pp. 489–491, Feb. 2009.

[37] M. S. Pilehvar and B. Mirafzal, "PV-fed smart inverters for mitigation of voltage and frequency fluctuations in islanded microgrids," in *Proc. 2020 International Conference on Smart Grids and Energy Systems (SGES)*, Nov. 2020, pp. 807–812.

[38] A. Adib, F. Fateh, and B. Mirafzal, "Smart inverter stability enhancement in weak grids using adaptive virtual-inductance," *IEEE Trans. Ind. Appl.*, vol. 57, no. 1, pp. 814–823, Jan.-Feb, 2021.

[39] F. Sadeque and F. Fateh, "On control schemes for grid-forming inverters." in *Proc. 2022 IEEE Kansas Power and Energy Conference (KPEC)*, Apr. 2022, pp. 1–6.

[40] H. Han, X. Hou, J. Yang, J. Wu, M. Su, and J. M. Guerrero, "Review of power sharing control strategies for islanding operation of AC microgrids," *IEEE Trans. Smart Grid*, vol. 7, no. 1, pp. 200–215, Jan. 2016.

[41] J. Rocabert, A. Luna, F. Blaabjerg, and P. Rodríguez, "Control of power converters in AC microgrids," *IEEE Trans. Power Electron.*, vol. 27, no. 11, pp. 4734–4749, Nov. 2012.

[42] D. B. Rathnayake, M. Akrami, C. Phurailatpam, S. P. Me, S. Hadavi, G. Jayasinghe, S. Zabihi, and B. Bahrani, "Grid forming inverter modeling, control, and applications," *IEEE Access*, vol. 9, pp. 114 781–114 807, 2021.

[43] D. G. Holmes and T. A. Lipo, *Pulse Width Modulation for Power Converters: Principles and Practice*. Hoboken, NJ, USA: Wiley, 2003.

[44] Y. Khayat, M. Naderi, Q. Shafiee, Y. Batmani, M. Fathi, J. M. Guerrero, and H. Bevrani, "Decentralized optimal frequency control in autonomous microgrids," *IEEE Trans. Power Sys.*, vol. 34, no. 3, pp. 2345–2353, May 2019.

[45] Y. Qi, H. Deng, J. Fang, and Y. Tang, "Synchronization stability analysis of grid-forming inverter: A black box methodology," *IEEE Trans. Ind. Electron.*, pp. 1–1, Dec. 2021.

[46] S. Sahoo, Y. Yang, and F. Blaabjerg, "Resilient synchronization strategy for AC microgrids under cyber attacks," *IEEE Trans. Power Electron.*, vol. 36, no. 1, pp. 73–77, Jan. 2021.

[47] Y. Li, Y. Gu, and T. Green, "Revisiting grid-forming and grid-following inverters: A duality theory," *IEEE Trans. Power Syst.*, pp. 1–1, Feb. 2022.

[48] M. Litwin, D. Zieliński, and K. Gopakumar, "Remote micro-grid synchronization without measurements at the point of common coupling," *IEEE Access*, vol. 8, pp. 212 753–212 764, Nov. 2020.

[49] I. Patrao, R. González-Medina, S. Marzal, G. Garcerá, and E. Figueres, "Synchronization of power inverters in islanded microgrids using an FM-modulated signal," *IEEE Trans. Smart Grid*, vol. 8, no. 1, pp. 503–510, Jan. 2017.

[50] M. S. Reza, F. Sadeque, M. M. Hossain, A. M. Y. M. Ghias, and V. G. Agelidis, "Three-phase PLL for grid-connected power converters under both amplitude and phase unbalanced conditions," *IEEE Trans. Ind. Electron.*, vol. 66, no. 11, pp. 8881–8891, Jan. 2019.

[51] Q.-C. Zhong, P.-L. Nguyen, Z. Ma, and W. Sheng, "Self-synchronized synchronverters: Inverters without a dedicated synchronization unit," *IEEE Trans. Power Electron.*, vol. 29, no. 2, pp. 617–630, Feb. 2014.

[52] T.-V. Tran, T.-W. Chun, H.-H. Lee, H.-G. Kim, and E.-C. Nho, "PLL-based seamless transfer control between grid-connected and islanding modes in grid-connected inverters," *IEEE Trans. Power Electron.*, vol. 29, no. 10, pp. 5218–5228, Oct. 2014.

[53] M. N. Arafat, A. Elrayyah, and Y. Sozer, "An effective smooth transition control strategy using droop-based synchronization for parallel inverters," *IEEE Trans. Ind. Appl.*, vol. 51, no. 3, pp. 2443–2454, May/Jun. 2015.

[54] Y. A.-R. I. Mohamed and A. A. Radwan, "Hierarchical control system for robust microgrid operation and seamless mode transfer in active distribution systems," *IEEE Trans. Smart Grid*, vol. 2, no. 2, pp. 352–362, Jun. 2011.

[55] M. Kwon, S. Park, C.-y. Oh, J. Lee, and S. Choi, "Unified control scheme of grid-connected inverters for autonomous and smooth transfer to stand-alone mode," *IEEE Trans. Power Electron.*, vol. 37, no. 1, pp. 416–425, Jan. 2022.

[56] J. M. Guerrero, J. C. Vasquez, J. Matas, M. Castilla, and L. Garcia de Vicuna, "Control strategy for flexible microgrid based on parallel line-interactive UPS systems," *IEEE Trans. Ind. Electron.*, vol. 56, no. 3, pp. 726–736, Mar. 2009.

[57] Z. Guo, D. Sha, and X. Liao, "Voltage magnitude and frequency control of three-phase voltage source inverter for seamless transfer," *IET Power Electron.*, vol. 7, no. 1, pp. 200–208, Jan. 2014.

[58] Z. Liu, J. Liu, and Y. Zhao, "A unified control strategy for three-phase inverter in distributed generation," *IEEE Trans. Power Electron.*, vol. 29, no. 3, pp. 1176–1191, Mar. 2014.

[59] S. Sajadian and R. Ahmadi, "Model predictive control of dual-mode operations Z-source inverter: Islanded and grid-connected," *IEEE Trans. Power Electron.*, vol. 33, no. 5, pp. 4488–4497, May 2018.

[60] J. Wang, N. C. P. Chang, X. Feng, and A. Monti, "Design of a generalized control algorithm for parallel inverters for smooth microgrid transition operation," *IEEE Trans. Ind. Electron.*, vol. 62, no. 8, pp. 4900–4914, Aug. 2015.

[61] F. Sadeque, D. Sharma, and B. Mirafzal, "Multiple grid-forming inverters in black-start: The challenges," in *Proc. 2021 IEEE 22nd Workshop on Control and Modelling of Power Electronics (COMPEL)*, 2021, pp. 1–6.

[62] M. M. A. Abdelaziz and H. E. Farag, "An enhanced supervisory control for islanded microgrid systems," *IEEE Trans. Smart Grid*, vol. 7, no. 4, pp. 1941–1943, Jul. 2016.

[63] S. K. Mazumder et al., "A review of current research trends in power-electronic innovations in cyber–physical systems," *IEEE J. Emerg. Sel. Topics Power Electron.*, vol. 9, no. 5, pp. 5146–5163, Oct. 2021.

[64] A. Bidram, B. Poudel, L. Damodaran, R. Fierro, and J. M. Guerrero, "Resilient and cybersecure distributed control of inverter-based islanded microgrids," *IEEE Trans. Ind. Informat.*, vol. 16, no. 6, pp. 3881–3894, Jun. 2020.

[65] T. Hossen, F. Sadeque, M. Gursoy, and B. Mirafzal, "Self-secure inverters against malicious setpoints," in *Proc. 2020 IEEE Electric Power and Energy Conference (EPEC)*, Nov. 2020, pp. 1–6.

[66] F. Sadeque and B. Mirafzal, "Cooperative inverters to overcome PLL malfunctions," in *Proc. 2021 IEEE 12th International Symposium on Power Electronics for Distributed Generation Systems (PEDG)*, Jun.-Jul. 2021, pp. 1–6.

[67] K. De Brabandere, B. Bolsens, J. Van den Keybus, A. Woyte, J. Driesen, and R. Belmans, "A voltage and frequency droop control method for parallel inverters," *IEEE Trans. Power Electron.*, vol. 22, no. 4, pp. 1107–1115, Jul. 2007.

[68] Q.-C. Zhong and G. Weiss, "Synchronverters: Inverters that mimic synchronous generators," *IEEE Trans. Ind. Electron.*, vol. 58, no. 4, pp. 1259–1267, Apr. 2011.

[69] B. B. Johnson, S. V. Dhople, A. O. Hamadeh, and P. T. Krein, "Synchronization of parallel single-phase inverters with virtual oscillator control," *IEEE Trans. Power Electron.*, vol. 29, no. 11, pp. 6124–6138, Nov. 2014.

[70] F. Sadeque, D. Sharma, and B. Mirafzal, "Power-sharing between grid-forming and grid-following inverters," in *Proc. 2021 IEEE 22nd Workshop on Control and Modelling of Power Electronics (COMPEL)*, Nov. 2021, pp. 1–5.

[71] X. Huang, K. Wang, J. Qiu, L. Hang, G. Li, and X. Wang, "Decentralized control of multi-parallel grid-forming DGs in islanded microgrids for enhanced transient performance," *IEEE Access*, vol. 7, pp. 17 958–17 968, Jan. 2019.

[72] M. Narimani and G. Moschopoulos, "Improved method for paralleling reduced switch VSI modules: Harmonic content and circulating current," *IEEE Trans. Power Electron.*, vol. 29, no. 7, pp. 3308–3317, Jul. 2014.

[73] J. M. Guerrero, J. Matas, L. Garcia de Vicuna, M. Castilla, and J. Miret, "Decentralized control for parallel operation of distributed generation inverters using resistive output impedance," *IEEE Trans. Ind. Electron.*, vol. 54, no. 2, pp. 994–1004, Apr. 2007.

[74] J. Guerrero, L. G. de Vicuna, J. Matas, M. Castilla, and J. Miret, "Output impedance design of parallel-connected UPS inverters with wireless load-sharing control," *IEEE Trans. Ind. Electron.*, vol. 52, no. 4, pp. 1126–1135, Aug. 2005.

[75] A. Milczarek, M. Malinowski, and J. M. Guerrero, "Reactive power management in islanded microgrid—proportional power sharing in hierarchical droop control," *IEEE Trans. Smart Grid*, vol. 6, no. 4, pp. 1631–1638, Jul. 2015.

[76] A. Adib, F. Fateh, and B. Mirafzal, "Weak grid impacts on the design of voltage source inverters —virtual inductance," in *Proc. 2018 IEEE 19th Workshop on Control and Modeling for Power Electronics (COMPEL)*, Jun. 2018, pp. 1–6.

[77] A. Adib and B. Mirafzal, "Virtual inductance for stable operation of grid-interactive voltage source inverters," *IEEE Trans. Ind. Electron.*, vol. 66, no. 8, pp. 6002–6011, Aug. 2019.

[78] R. Majumder, B. Chaudhuri, A. Ghosh, R. Majumder, G. Ledwich, and F. Zare, "Improvement of stability and load sharing in an autonomous microgrid using supplementary droop control loop," *IEEE Trans. Power Syst.*, vol. 25, no. 2, pp. 796–808, May 2010.

[79] J. Erdocia, A. Urtasun, and L. Marroyo, "Power angle–frequency droop control to enhance transient stability of grid–forming inverters under voltage dips," *IEEE J. Emerg. Sel. Topics Power Electron.*, pp. 1–1, 2022.

[80] T. Shintai, Y. Miura, and T. Ise, "Oscillation damping of a distributed generator using a virtual synchronous generator," *IEEE Trans. Power Del.*, vol. 29, no. 2, pp. 668–676, Apr. 2014.

[81] S. D'Arco and J. A. Suul, "Equivalence of virtual synchronous machines and frequency-droops for converter-based microgrids," *IEEE Trans. Smart Grid*, vol. 5, no. 1, pp. 394–395, Jan. 2014.

[82] J. Liu, Y. Miura, and T. Ise, "Comparison of dynamic characteristics between virtual synchronous generator and droop control in inverter-based distributed generators," *IEEE Trans. Power Electron.*, vol. 31, no. 5, pp. 3600–3611, May 2016.

[83] X. Meng, J. Liu, and Z. Liu, "A generalized droop control for grid-supporting inverter based on comparison between traditional droop control and virtual synchronous generator control," *IEEE Trans. Power Electron.*, vol. 34, no. 6, pp. 5416–5438, Jun. 2019.

[84] F. Wang, L. Zhang, X. Feng, and H. Guo, "An adaptive control strategy for virtual synchronous generator," *IEEE Trans. Ind. Appl.*, vol. 54, no. 5, pp. 5124–5133, Sept./Oct. 2018.

[85] M. van Wesenbeeck, S. de Haan, P. Varela, and K. Visscher, "Grid tied converter with virtual kinetic storage," in *Proc. 2009 IEEE Bucharest PowerTech*, Jun. 2009, pp. 1–7.

[86] J. Alipoor, Y. Miura, and T. Ise, "Power system stabilization using virtual synchronous generator with alternating moment of inertia," *IEEE J. Emerg. Sel. Topics Power Electron.*, vol. 3, no. 2, pp. 451–458, Jun. 2015.

[87] M. A. Torres L., L. A. C. Lopes, L. A. Morán T., and J. R. Espinoza C., "Self-tuning virtual synchronous machine: A control strategy for energy storage systems to support dynamic frequency control," *IEEE Trans. Energy Convers.*, vol. 29, no. 4, pp. 833–840, Dec. 2014.

[88] D. Li, Q. Zhu, S. Lin, and X. Y. Bian, "A self-adaptive inertia and damping combination control of VSG to support frequency stability," *IEEE Trans. Energy Convers.*, vol. 32, no. 1, pp. 397–398, Mar. 2017.

[89] M. Sinha, F. Dörfler, B. B. Johnson, and S. V. Dhople, "Uncovering droop control laws embedded within the nonlinear dynamics of van der pol oscillators," *IEEE Trans. Control Netw. Syst.*, vol. 4, no. 2, pp. 347–358, Jun. 2017.

[90] M. Colombino, D. Groß, J.-S. Brouillon, and F. Dörfler, "Global phase and magnitude synchronization of coupled oscillators with application to the control of grid-forming power inverters," *IEEE Trans. Autom. Control*, vol. 64, no. 11, pp. 4496–4511, Nov. 2019.

[91] B. B. Johnson, M. Sinha, N. G. Ainsworth, F. Dörfler, and S. V. Dhople, "Synthesizing virtual oscillators to control islanded inverters," *IEEE Trans. Power Electron.*, vol. 31, no. 8, pp. 6002–6015, Aug. 2016.

[92] M. A. Awal, H. Yu, H. Tu, S. M. Lukic, and I. Husain, "Hierarchical control for virtual oscillator based grid-connected and islanded microgrids," *IEEE Trans. Power Electron.*, vol. 35, no. 1, pp. 988–1001, Jan. 2020.

[93] M. A. Awal and I. Husain, "Unified virtual oscillator control for grid-forming and grid-following converters," *IEEE J. Emerg. Sel. Topics Power Electron.*, vol. 9, no. 4, pp. 4573–4586, 2021.

[94] F. K. d. A. Lima, R. G. Araújo, F. L. Tofoli, and C. G. C. Branco, "A phase-locked loop algorithm for single-phase systems with inherent disturbance rejection," *IEEE Trans. Ind. Electron.*, vol. 66, no. 12, pp. 9260–9267, Dec. 2019.

[95] H. A. Hamed and M. S. El Moursi, "A new type-2 PLL based on unit delay phase angle error compensation during the frequency ramp," *IEEE Trans. Power Syst.*, vol. 34, no. 4, pp. 3289–3293, Jul. 2019.

[96] M. Chen, L. Peng, B. Wang, and J. Kan, "PLL based on extended trigonometric function delayed signal cancellation under various adverse grid conditions," *IET Power Electronics*, vol. 11, no. 10, pp. 1689–1697, Aug. 2018.

[97] M. E. Meral, "Improved phase-locked loop for robust and fast-tracking of three phases under asymmetrical electric grid conditions," *IET Gener. Transmiss. Distrib.*, vol. 6, no. 2, pp. 152–160, Feb. 2012.

[98] C. Subramanian and R. Kanagaraj, "Rapid tracking of grid variables using prefiltered synchronous reference frame PLL," *IEEE Trans. Instrum. Meas.*, vol. 64, no. 7, pp. 1826–1836, Jul. 2015.

[99] P. Kanjiya, V. Khadkikar, and M. S. E. Moursi, "Obtaining performance of type-3 phase-locked loop without compromising the benefits of type-2 control system," *IEEE Trans. Power Electron.*, vol. 33, no. 2, pp. 1788–1796, Feb. 2018.

[100] B. Liu, F. Zhuo, Y. Zhu, H. Yi, and F. Wang, "A three-phase PLL algorithm based on signal reforming under distorted grid conditions," *IEEE Trans. Power Electron.*, vol. 30, no. 9, pp. 5272–5283, Sept. 2015.

[101] L. B. G. Campanhol, S. A. O. da Silva, A. A. de Oliveira, and V. D. Bacon, "Power flow and stability analyses of a multifunctional distributed generation system integrating

a photovoltaic system with unified power quality conditioner," *IEEE Trans. Power Electron.*, vol. 34, no. 7, pp. 6241–6256, Jul. 2019.

[102] M. Karimi-Ghartemani, M. Mojiri, A. Safaee, J. A. Walseth, S. A. Khajehoddin, P. Jain, and A. Bakhshai, "A new phase-locked loop system for three-phase applications," *IEEE Tran. Power Electron.*, vol. 28, no. 3, pp. 1208–1218, Mar. 2013.

[103] S. Golestan, E. Ebrahimzadeh, J. M. Guerrero, J. C. Vasquez, and F. Blaabjerg, "An adaptive least-error squares filter-based phase-locked loop for synchronization and signal decomposition purposes," *IEEE Trans. Ind. Electron.*, vol. 64, no. 1, pp. 336–346, Jan. 2017.

[104] K.-J. Lee, J.-P. Lee, D. Shin, D.-W. Yoo, and H.-J. Kim, "A novel grid synchronization PLL method based on adaptive low-pass notch filter for grid-connected PCS," *IEEE Trans. Ind. Electron.*, vol. 61, no. 1, pp. 292–301, Jan. 2014.

[105] Q. Huang and K. Rajashekara, "An improved delayed signal cancellation PLL for fast grid synchronization under distorted and unbalanced grid condition," *IEEE Trans. Ind. Appl.*, vol. 53, no. 5, pp. 4985–4997, Sept.-Oct. 2017.

[106] F. Wu and X. Li, "Multiple DSC filter-based three-phase EPLL for nonideal grid synchronization," *IEEE J. Emerg. Sel. Topics Power Electron.*, vol. 5, no. 3, pp. 1396–1403, Sept. 2017.

[107] M. Xie, H. Wen, C. Zhu, and Y. Yang, "DC offset rejection improvement in single-phase SOGI-PLL algorithms: Methods review and experimental evaluation," *IEEE Access*, vol. 5, pp. 12 810–12 819, Jun. 2017.

[108] P. Rodriguez, J. Pou, J. Bergas, J. I. Candela, R. P. Burgos, and D. Boroyevich, "Decoupled double synchronous reference frame PLL for power converters control," *IEEE Trans. Power Electron.*, vol. 22, no. 2, pp. 584–592, Mar. 2007.

[109] L. Hadjidemetriou, E. Kyriakides, and F. Blaabjerg, "A new hybrid PLL for interconnecting renewable energy systems to the grid," *IEEE Trans. Ind. Appl.*, vol. 49, no. 6, pp. 2709–2719, Nov.-Dec. 2013.

[110] J. Benzaquen, F. Fateh, M. B. Shadmand, and B. Mirafzal, "Performance comparison of active rectifier control schemes in more electric aircraft applications," *IEEE Trans. Trans. Electrific.*, vol. 5, no. 4, pp. 1470–1479, Dec. 2019.

[111] H. Mahmood, D. Michaelson, and J. Jiang, "Reactive power sharing in islanded microgrids using adaptive voltage droop control," *IEEE Trans. Smart Grid*, vol. 6, no. 6, pp. 3052–3060, Nov. 2015.

[112] G. Lou et al., "Decentralised secondary voltage and frequency control scheme for islanded microgrid based on adaptive state estimator," *IET Gen. Transmiss. Distrib.*, vol. 11, no. 15, pp. 3683–3693, Oct. 2017.

[113] B. Liu, T. Wu, Z. Liu, and J. Liu, "A small-AC-signal injection-based decentralized secondary frequency control for droop-controlled islanded microgrids," *IEEE Tran. Power Electron.*, vol. 35, no. 11, pp. 11 634–11 651, Nov. 2020.

[114] W. Gu, G. Lou, W. Tan, and X. Yuan, "A nonlinear state estimator-based decentralized secondary voltage control scheme for autonomous microgrids," *IEEE Trans. Power Syst.*, vol. 32, no. 6, pp. 4794–4804, Nov. 2017.

[115] J. M. Rey, P. Martí, M. Velasco, J. Miret, and M. Castilla, "Secondary switched control with no communications for islanded microgrids," *IEEE Trans. Ind. Electron.*, vol. 64, no. 11, pp. 8534–8545, Nov. 2017.

[116] Y. Han, H. Li, L. Xu, X. Zhao, and J. M. Guerrero, "Analysis of washout filter-based power sharing strategy—an equivalent secondary controller for islanded microgrid without LBC lines," *IEEE Trans. Smart Grid*, vol. 9, no. 5, pp. 4061–4076, Sept. 2018.

[117] M. Yazdanian and A. Mehrizi-Sani, "Washout filter-based power sharing," *IEEE Trans. Smart Grid*, vol. 7, no. 2, pp. 967–968, Mar. 2016.

[118] D. Sharma, F. Sadeque, and B. Mirafzal, "Synchronization of inverters in grid forming mode," *IEEE Access*, vol. 10, pp. 41 341–41 351, Apr. 2022.

[119] C. J. O'Rourke, M. M. Qasim, M. R. Overlin, and J. L. Kirtley, "A geometric interpretation of reference frames and transformations: dq0, Clarke, and Park," *IEEE Trans. Energy Convers.*, vol. 34, no. 4, pp. 2070–2083, Dec. 2019.

[120] R. Park, "Two reaction theory of synchronous machines," *AIEE Trans.*, vol. 48, pp. 716–730, 1929.

[121] F. Sadeque, J. Benzaquen, A. Adib, and B. Mirafzal, "Direct phase-angle detection for three-phase inverters in asymmetrical power grids," *IEEE J. Emerg. Sel. Topics Power Electron.*, vol. 9, no. 1, pp. 520–528, Mar. 2021.

[122] V. M. Moreno, M. Liserre, A. Pigazo, and A. Dell'Aquila, "A comparative analysis of real-time algorithms for power signal decomposition in multiple synchronous reference frames," *IEEE Trans. Power Electron.*, vol. 22, no. 4, pp. 1280–1289, Jul. 2007.

[123] P. Rodríguez, A. Luna, R. S. Muñoz-Aguilar, I. Etxeberria-Otadui, R. Teodorescu, and F. Blaabjerg, "A stationary reference frame grid synchronization system for three-phase grid-connected power converters under adverse grid conditions," *IEEE Trans. Power Electron.*, vol. 27, no. 1, pp. 99–112, Jan. 2012.

[124] L. Lopes and H. Sun, "Performance assessment of active frequency drifting islanding detection methods," *IEEE Trans. Energy Convers.*, vol. 21, no. 1, pp. 171–180, Mar. 2006.

[125] A. Pouryekta, V. K. Ramachandaramurthy, N. Mithulananthan, and A. Arulampalam, "Islanding detection and enhancement of microgrid performance," *IEEE Syst. J.*, vol. 12, no. 4, pp. 3131–3141, Dec. 2018.

[126] F. Sadeque and B. Mirafzal, "Frequency restoration of grid-forming inverters in pulse load and plug-in events," *IEEE J. Emerg. Sel. Topics Power Electron.*, pp. 1–8, Jun. 2022.

[127] A. Adib, K. K. Afridi, M. Amirabadi, F. Fateh, M. Ferdowsi, B. Lehman, L. H. Lewis, B. Mirafzal, M. Saeedifard, M. B. Shadmand, and P. Shamsi, "E-mobility — advancements and challenges," *IEEE Access*, vol. 7, pp. 165 226–165 240, 2019.

[128] J. Benzaquen, M. B. Shadmand, and B. Mirafzal, "Ultrafast rectifier for variable-frequency applications," *IEEE Access*, vol. 7, pp. 9903–9911, 2019.

[129] J. Benzaquen, F. Fateh, and B. Mirafzal, "On the dynamic performance of variable-frequency AC–DC converters," *IEEE Trans. Transport. Electrific.*, vol. 6, no. 2, pp. 530–539, 2020.

[130] J. Benzaquen and B. Mirafzal, "An active rectifier fed by a variable-speed generator," in *2020 IEEE Applied Power Electronics Conference and Exposition (APEC)*, 2020, pp. 1691–1696.

[131] J. Benzaquen, J. He, and B. Mirafzal, "Toward more electric powertrains in aircraft: Technical challenges and advancements," *CES Trans. Electric. Mach. Syst.*, vol. 5, no. 3, pp. 177–193, 2021.

[132] J. Benzaquen and B. Mirafzal, "Seamless dynamics for wild-frequency active rectifiers in more electric aircraft," *IEEE Trans. Ind. Electron.*, vol. 67, no. 9, pp. 7135–7145, 2020.

[133] A. Adib, F. Fateh, and B. Mirafzal, "A stabilizer for inverters operating in grid-feeding, grid-supporting and grid-forming modes," in *2019 IEEE Energy Conversion Congress and Exposition (ECCE)*, 2019, pp. 2239–2244.

[134] F. Fuchs, "Some diagnosis methods for voltage source inverters in variable speed drives with induction machines - a survey," in *Proc. IECON'03. 29th Annual Conference of the IEEE Industrial Electronics Society*, vol. 2, 2003, pp. 1378–1385 Vol.2.

[135] A. Singh and B. Mirafzal, "A generator-converter topology with zero DC-link impedance for direct drive wind turbines," *IEEE Trans. Energy Convers.*, vol. 32, no. 4, pp. 1620–1623, 2017.

[136] A. Singh, J. Benzaquen, and B. Mirafzal, "Current source generator–converter topology for direct-drive wind turbines," *IEEE Trans. Ind. Appl.*, vol. 54, no. 2, pp. 1663–1670, 2018.

[137] M. S. Pilehvar, M. B. Shadmand, and B. Mirafzal, "Analysis of smart loads in nanogrids," *IEEE Access*, vol. 7, pp. 548–562, Dec. 2019.

[138] B. Mirafzal, "Survey of fault-tolerance techniques for three-phase voltage source inverters," *IEEE Trans. Ind. Electron.*, vol. 61, no. 10, pp. 5192–5202, 2014.

[139] B. Lu and S. K. Sharma, "A literature review of IGBT fault diagnostic and protection methods for power inverters," *IEEE Trans. Ind. Appl.*, vol. 45, no. 5, pp. 1770–1777, 2009.

[140] F. Richardeau, P. Baudesson, and T. Meynard, "Failures-tolerance and remedial strategies of a PWM multicell inverter," *IEEE Trans. Power Electron.*, vol. 17, no. 6, pp. 905–912, 2002.

[141] D. Kastha and B. Bose, "Investigation of fault modes of voltage-fed inverter system for induction motor drive," *IEEE Trans. Ind. Appl.*, vol. 30, no. 4, pp. 1028–1038, 1994.

Appendix A

Matrix Elements for The State-Space Equations

A.1 Matrix Elements for The Controller-Sync Method

In this appendix, the matrix elements in the state-space model in (2.36) and (2.51) from Section 2.4 are provided. The matrix elements of (2.36) are

$$a_{11} = -\left(R/L\right) + \left(1/L\right)\left(V_{10} sin\left(\theta_{10}\right)\right)\left(m_P k_{P4} k_{P3} + k_{P4}\right)\left(3/2\right) V_{qpcc0}, \tag{A.1}$$

$$a_{12} = -\omega - \left(1/L\right)\left(cos\left(\theta_{10}\right)\right)\left(m_Q k_{P2} k_{P1} + k_{P2}\right)\left(3/2\right) V_{qpcc0}, \tag{A.2}$$

$$a_{13} = \left(1/L\right) k_{P2}\left(cos\left(\theta_{10}\right)\right), \tag{A.3}$$

$$a_{14} = \left(1/L\right)\left(cos\left(\theta_{10}\right)\right), \tag{A.4}$$

$$a_{15} = -\left(1/L\right) k_{P4}\left(V_{10} sin\left(\theta_{10}\right)\right), \tag{A.5}$$

$$a_{16} = -\left(1/L\right)\left(V_{10} sin\left(\theta_{10}\right)\right), \tag{A.6}$$

$$a_{21} = \omega + \left(1/L\right)\left(V_{10} cos\left(\theta_{10}\right)\right)\left(m_P k_{P4} k_{P3} + k_{P4}\right)\left(3/2\right) V_{qpcc0}, \tag{A.7}$$

$$a_{22} = -\left(R/L\right) + \left(1/L\right)\left(sin\left(\theta_{10}\right)\right)\left(m_Q k_{P2} k_{P1} + k_{P2}\right)\left(3/2\right) V_{qpcc0}, \tag{A.8}$$

$$a_{23} = -\left(1/L\right) k_{P2}\left(sin\left(\theta_{10}\right)\right), \tag{A.9}$$

$$a_{24} = -\left(1/L\right)\left(sin\left(\theta_{10}\right)\right), \tag{A.10}$$

$$a_{25} = -\left(1/L\right) k_{P4}\left(V_{10} cos\left(\theta_{10}\right)\right), \tag{A.11}$$

$$a_{26} = -\left(1/L\right)\left(V_{10} cos\left(\theta_{10}\right)\right), \tag{A.12}$$

$$a_{32} = -\left(3/2\right) k_{I1} m_Q V_{qpcc0}, \tag{A.13}$$

$$a_{31} = a_{33} = a_{34} = a_{35} = a_{36} = 0, \tag{A.14}$$

$$a_{42} = -\left(3/2\right)\left(k_{I2} k_{P1} m_Q + k_{I2}\right) V_{qpcc0}, \tag{A.15}$$

$$a_{43} = k_{I2}, \tag{A.16}$$

$$a_{41} = a_{44} = a_{45} = a_{46} = 0, \tag{A.17}$$

$$a_{51} = -\left(3/2\right) k_{I3} m_P V_{qpcc0}, \tag{A.18}$$

$$a_{52} = a_{53} = a_{54} = a_{55} = a_{56} = 0, \tag{A.19}$$

$$a_{61} = -\left(3/2\right)\left(k_{I4} k_{P3} m_P + k_{I4}\right) V_{qpcc0}, \tag{A.20}$$

$$a_{65} = k_{I4}, \tag{A.21}$$

$$a_{62} = a_{63} = a_{64} = a_{66} = 0, \tag{A.22}$$

and,

$$\begin{aligned} b_{v1} = &-\left(1/L\right) - \left(1/L\right)\left(cos\left(\theta_{10}\right)\right)\left(m_Q k_{P2} k_{P1} + k_{P2}\right)\left(3/2\right) I_{d0} \\ &+ \left(1/L\right)\left(V_{10} sin\left(\theta_{10}\right)\right)\left(m_P k_{P4} k_{P3} + k_{P4}\right)\left(3/2\right) I_{q0} \\ &+ \left(1/L\right)\left(cos\left(\theta_{10}\right)\right)\left(1 - k_{P2} k_{P1}\right), \end{aligned} \tag{A.23}$$

$$b_{v2} = (1/L)\,(sin\,(\theta_{10}))\,(m_Q k_{P2} k_{P1} + k_{P2})\,(3/2)\,I_{d0}$$
$$+ (1/L)\,(V_{10} cos\,(\theta_{10}))\,(m_P k_{P4} k_{P3} + k_{P4})\,(3/2)\,I_{q0} \tag{A.24}$$
$$- (1/L)\,(sin\,(\theta_{10}))\,(1 - k_{P2} k_{P1})\,,$$

$$b_{v3} = -\,(3/2)\,k_{I1} m_Q I_{d0} - k_{I1}, \tag{A.25}$$

$$b_{v4} = -\,(3/2)\,(k_{I2} k_{P1} m_Q + k_{I2})\,I_{d0} - k_{I2} k_{P1}, \tag{A.26}$$

$$b_{v5} = -\,(3/2)\,k_{I3} m_P I_{q0}, \tag{A.27}$$

$$b_{v6} = -\,(3/2)\,(k_{I4} k_{P3} m_P + k_{I4})\,I_{q0}, \tag{A.28}$$

$$b_{\theta 1} = -\,(1/L)\,(V_{10} sin\,(\theta_{10}))\,, \tag{A.29}$$

$$b_{\theta 2} = -\,(1/L)\,(V_{10} cos\,(\theta_{10}))\,, \tag{A.30}$$

$$b_{\theta 3} = b_{\theta 4} = b_{\theta 5} = b_{\theta 6} = 0, \tag{A.31}$$

$$b_{\omega 1} = (1/L)\,(V_{10} sin\,(\theta_{10}))\,k_{P4} k_{P3}, \tag{A.32}$$

$$b_{\omega 2} = (1/L)\,(V_{10} cos\,(\theta_{10}))\,k_{P4} k_{P3}, \tag{A.33}$$

$$b_{\omega 5} = -k_{I3} k_{P3}, \tag{A.34}$$

$$b_{\omega 3} = b_{\omega 4} = b_{\omega 6} = 0. \tag{A.35}$$

The matrix elements of (2.51) are

$$\alpha_{11} = -\,(R/L)\,, \tag{A.36}$$

$$\alpha_{12} = -\omega + (1/L)\,(cos\,(\theta_{20}))\,(-m_Q k_{PV})\,(3/2)\,V_{qpcc0}, \tag{A.37}$$

$$\alpha_{13} = -\,(1/L)\,(sin\,(\theta_{20}))\,V_{20}, \tag{A.38}$$

$$\alpha_{14} = (1/L)\,(cos\,(\theta_{20}))\,, \tag{A.39}$$

$$\alpha_{21} = \omega, \tag{A.40}$$

$$\alpha_{22} = -\left(R/L\right) + \left(1/L\right) m_Q k_{PV} \left(sin\left(\theta_{20}\right)\right) \left(3/2\right) V_{qpcc0}, \tag{A.41}$$

$$\alpha_{23} = -\left(1/L\right) \left(cos\left(\theta_{20}\right)\right) V_{20}, \tag{A.42}$$

$$\alpha_{24} = -\left(1/L\right) \left(sin\left(\theta_{20}\right)\right), \tag{A.43}$$

$$\alpha_{31} = -m_P \left(3/2\right) V_{qpcc0}, \tag{A.44}$$

$$\alpha_{32} = \alpha_{33} = \alpha_{34} = 0, \tag{A.45}$$

$$\alpha_{42} = -m_Q k_{IV} \left(3/2\right) V_{qpcc0}, \tag{A.46}$$

$$\alpha_{41} = \alpha_{43} = \alpha_{44} = 0, \tag{A.47}$$

and,

$$\beta_1 = -\left(1/L\right) - k_{PV}(1/L) \left(cos\left(\theta_{20}\right)\right) - m_Q k_{PV}(1/L) \left(cos\left(\theta_{20}\right)\right) \left(3/2\right) I_{d0}, \tag{A.48}$$

$$\beta_2 = k_{PV} \left(1/L\right) \left(sin\left(\theta_{20}\right)\right) + m_Q k_{PV}(1/L) \left(sin\left(\theta_{20}\right)\right) \left(3/2\right) I_{d0}, \tag{A.49}$$

$$\beta_3 = -m_P \left(3/2\right) I_{q0}, \tag{A.50}$$

$$\beta_4 = -m_Q k_{IV} \left(3/2\right) I_{d0} - k_{IV}. \tag{A.51}$$

A.2 Matrix Elements for Universal Controller

In this appendix, the matrix elements in the state-space model in (4.32) and (4.32) from Section 4.3 are provided. The state-matrix elements are already provided in Appendix A.1 as state-matrix is same as of (2.39). The modified control matrix elements of (4.32) are as follows

$$b_{v3}^U = -\left(3/2\right) k_{I1} m_Q I_{d0}, \tag{A.52}$$

$$b_{v4}^U = -\left(3/2\right) \left(k_{P1} m_Q + 1\right) k_{I2} I_{d0}, \tag{A.53}$$

$$b_{P1}^{U} = -\left(1/L\right) V_{20} sin\left(\theta_{10}\right)\left(m_P k_{P3}+1\right) k_{P4}, \tag{A.54}$$

$$b_{P2}^{U} = -\left(1/L\right) V_{20} cos\left(\theta_{10}\right)\left(m_P k_{P3}+1\right) k_{P4}, \tag{A.55}$$

$$b_{P3}^{U} = b_{P4}^{U} = 0, \tag{A.56}$$

$$b_{P5}^{U} = k_{I3} m_P, \tag{A.57}$$

$$b_{P6}^{U} = k_{I4}\left(m_P k_{P3}+1\right), \tag{A.58}$$

$$b_{Q1}^{U} = \left(1/L\right) cos\left(\theta_{20}\right)\left(m_Q k_{P1}+1\right) k_{P2}, \tag{A.59}$$

$$b_{Q2}^{U} = -\left(1/L\right) sin\left(\theta_{20}\right)\left(m_Q k_{P1}+1\right) k_{P2}, \tag{A.60}$$

$$b_{Q3}^{U} = k_{I1} m_Q. \tag{A.61}$$

$$b_{Q4}^{U} = k_{I2}\left(m_Q k_{P1}+1\right), \tag{A.62}$$

$$b_{Q5}^{U} = b_{Q6}^{U} = 0. \tag{A.63}$$

The control-matrix elements for (4.46) are as follows

$$\beta_{v1} = -\left(1/L\right) - k_{PV}(1/L)\left(cos\left(\theta_{20}\right)\right) - m_Q k_{PV}(1/L)\left(cos\left(\theta_{20}\right)\right)\left(3/2\right) I_{d0}, \tag{A.64}$$

$$\beta_{v2} = k_{PV}\left(1/L\right)\left(sin\left(\theta_{20}\right)\right) + m_Q k_{PV}(1/L)\left(sin\left(\theta_{20}\right)\right)\left(3/2\right) I_{d0}, \tag{A.65}$$

$$\beta_{v3} = -m_P\left(3/2\right) I_{q0}, \tag{A.66}$$

$$\beta_{v4} = -m_Q k_{IV}\left(3/2\right) I_{d0} - k_{IV}, \tag{A.67}$$

$$\beta_{P3}^{U} = m_P, \tag{A.68}$$

$$\beta_{P1}^{U} = \beta_{P2}^{U} = \beta_{P4}^{U} = 0, \tag{A.69}$$

$$\beta_{Q1}^{U} = \left(1/L\right)\ cos\left(\theta_{20}\right) k_{PV} m_Q, \tag{A.70}$$

$$\beta_{Q2}^{U} = -(1/L)\ sin\left(\theta_{20}\right) k_{PV} m_Q, \tag{A.71}$$

$$\beta_{Q3}^{U} = 0, \tag{A.72}$$

$$\beta_{Q4}^{4} = k_{IV} m_Q. \tag{A.73}$$

A.3 Matrix Elements for The Restoration Method

The matrix elements (5.34) developed in Section 5.3 are provided here. The state-matrix elements are,

$$a_{11}^{R} = -\left(R/L\right), \tag{A.74}$$

$$a_{12}^{R} = -\omega - \left(1/L\right)\left(cos\left(\theta_0\right)\right)\left(m_Q k_{PV}\right)\left(3/2\right) V_{qpcc0}, \tag{A.75}$$

$$a_{13}^{R} = -\left(1/L\right)\left(1/k_{IP}\right)\left(V_0 sin\left(\theta_0\right)\right), \tag{A.76}$$

$$a_{14}^{R} = -\left(1/L\right)\left(cos\left(\theta_0\right)\right)\left(m_Q k_{PV} - k_{IV}/k_{IQ}\right), \tag{A.77}$$

$$a_{21}^{R} = \omega, \tag{A.78}$$

$$a_{22}^{R} = -\left(R/L\right) + \left(1/L\right)\left(sin\left(\theta_0\right)\right)\left(m_Q k_{PV}\right)\left(3/2\right) V_{qpcc0}, \tag{A.79}$$

$$a_{23}^{R} = -\left(1/L\right)\left(1/k_{IP}\right)\left(V_0 cos\left(\theta_0\right)\right), \tag{A.80}$$

$$a_{24}^{R} = \left(1/L\right)\left(sin\left(\theta_0\right)\right)\left(m_Q k_{PV} - k_{IV}/k_{IQ}\right), \tag{A.81}$$

$$a_{31}^{R} = -m_P k_{IP}\left(3/2\right) V_{qpcc0}, \tag{A.82}$$

$$a_{33}^{R} = -m_P k_{IP}, \tag{A.83}$$

$$a_{42}^{R} = -m_Q k_{IQ}\left(3/2\right) V_{qpcc0}, \tag{A.84}$$

$$a_{44}^{R} = -m_Q k_{IQ}, \tag{A.85}$$

$$a_{32}^{R} = a_{34}^{R} = a_{41}^{R} = a_{43}^{R} = 0. \tag{A.86}$$

The control matrix elements of (5.34) are,

$$b_1^R = -\left(1/L\right) - \left(1/L\right)\left(cos\left(\theta_0\right)\right)\left(k_{PV} + m_Q k_{PV}\left(3/2\right) I_{d0} + k_{IV} T_s\right) - \left(1/L\right) k_{IV} cos\left(\theta_0\right), \tag{A.87}$$

$$b_2^R = -(1/L)\left(sin\left(\theta_0\right)\right)\left(k_{PV} + m_Q k_{PV}\left(3/2\right) I_{d0} + k_{IV} T_s\right) + \left(1/L\right) k_{IV} sin\left(\theta_0\right), \tag{A.88}$$

$$b_3^R = -m_P k_{IP}\left(3/2\right) I_{q0}, \tag{A.89}$$

$$b_4^R = -m_Q k_{IQ}\left(3/2\right) I_{d0}, \tag{A.90}$$

Appendix B

Microgrid Testbed Development

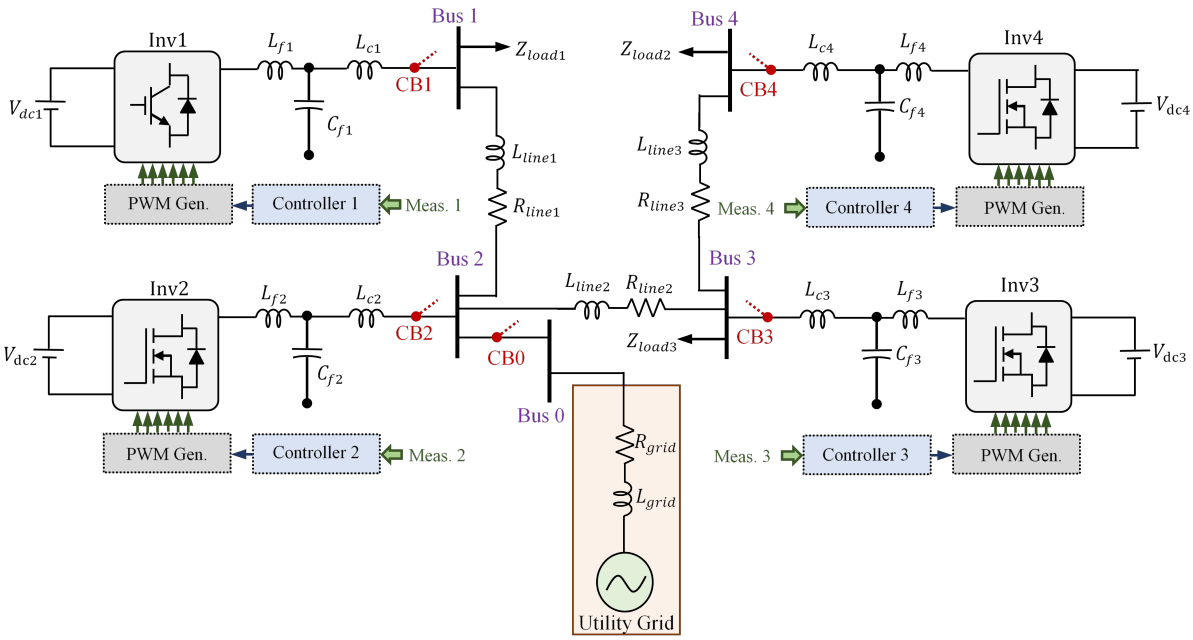

Figure B.1: *Schematic diagram of the developed microgrid testbed.*

This section briefly describes the hardware development process of the microgrid testbed used for testing the performance of the developed controllers presented in this dissertation. Fig. B.1 shows the schematic diagram of the developed micorgrid testbed. Notice that, the testbed forms a five bus system with four inverters and a grid, each connected to one of the buses. Here, each inverter has a DC supply, an LCL filter setup, a measurement board, a

circuit breaker, and a controller. Bus-1, 3, and 4 have loads connected. There are three tie lines connecting Bus-1 and 2, Bus-2 and 3, and Bus-3 and 4. The utility grid can be separated from the microgrid through a circuit breaker.

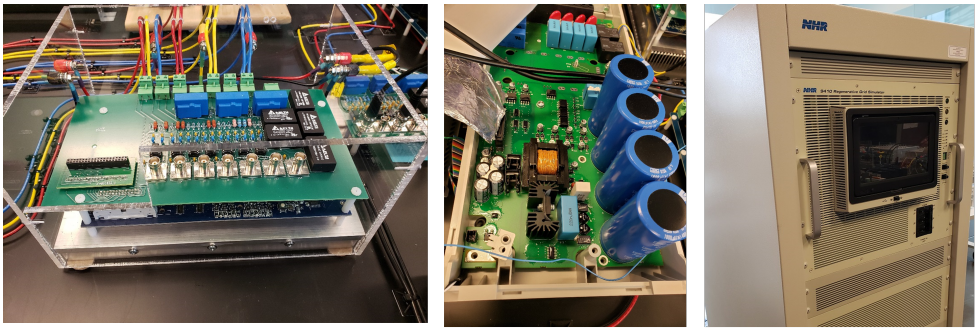

(a) (b) (c)

Figure B.2: *Inverters and grid-simulator used for the developed microgrid; (a)* 5 *kVA SiC inverter, (b)* 10 *kVA Si inverter, and (c)* 30 *kVA grid-simulator.*

Fig. B.2(a) shows the 5 *kVA* SiC inverter used for $Inv2$, $Inv3$, and $Inv4$. This inverter consists of a commercial *Wolfspeed CREE CGD15FB45P1* 1200 V six channel SiC gate driver board and a *Wolfspeed CCS020M12CM2* 1200 V, 20 A, SiC six pack module. A high efficiency heat-sink with is attached with the SiC module to provide sufficient cooling and form the base of the inverter. A laboratory developed measurement board with built-in interface for the controllers is assembled with the gate driver board, switches, and heat-sink. The inverter in Fig. B.2(b) is a commercially developed *Allen Bradley Powerflex 755* 10 *kVA* Si inverter. The inverter is air-cooled with built-in fan and heat-sink. This inverter is used for $Inv1$ in the testbed. Interface for the controller is commercially built-in on the gate driver board. A separate measurement board, as in Fig. B.2(a) is required for this setup.The grid is represented with a 30 *NHR 9410* grid-simulator, see Fig. B.2(c). This grid-simulator can be configured to provide three-phase line-line voltage signals, and can supply and absorb active and reactive power, and can be operated directly from the control panel or from a computer.

The inverters are controlled through separate *dSPACE MicrolabBox 1202* modules, see Fig. B.3(a). The control algorithms are developed in *MATLAB-Simulink* environment and

burned into the *dSPACE* controllers. Fig. B.3(b) shows a high-level schematic of inverter controller developed in *MATLAB-Simulink*. The control operation and processed data can be accessed through the *ControlDesk* software which can communicate with the dSPACE modules through Ethernet connection. Fig. B.3(c) shows a control panel of two of the inverters in the microgrid testbed. The *dSPACE* controllers are equipped with digital and

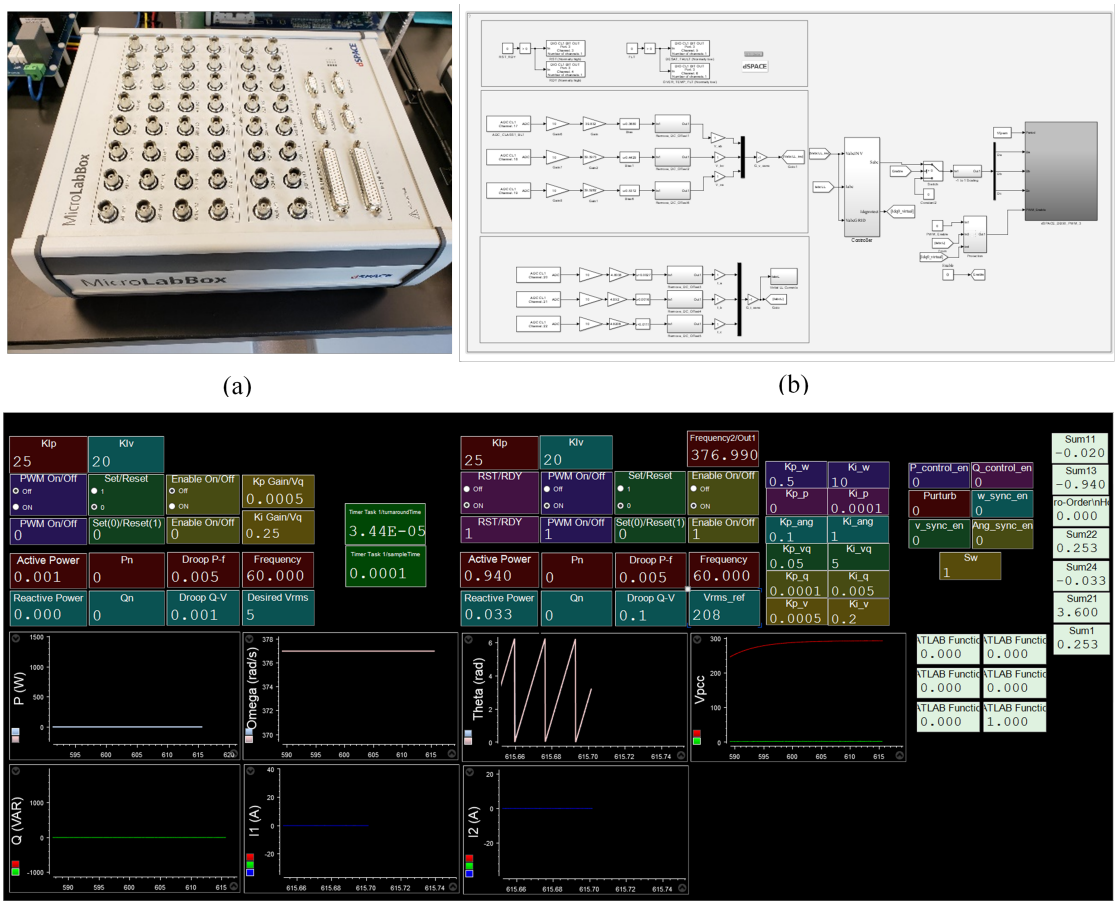

Figure B.3: *I/O of the inverter controller; (a) The dSPACE MicroLabBox for controller implementation, (b) high-level schematic of the controller in MATLAB-Simulink, and (c) control panel of the ControlDesk software.*

analog input/output channels. The measurement signals are converted to digital signals through the A/D input and digitally filtered inside the controller. The PWM signals are sent to the hardware through the digital output port of the controllers. Note that, the measurement board, the gate-driver board, and the controller in each setup must have a

common ground for measurement and control. Electromagnetic shields are provided to the ribbons carrying the PWM signals.

The measurement board, as shown in Fig. B.4, forms the interface between the circuit and the controller. The board in Fig. B.4(a) has three AC voltage sensors, one DC voltage sensors, and three AC current sensors with a maximum measurement capacity up to 340 V, 400 V, and 30 A. Here, the voltages are reduces by resistor based voltage divider followed by the operational amplifiers (OpAmps). The currents are directly passed through the sensors and converted to small current signals and then passed through the OpAmps. The purposes of the OpAmps are, to control output of the measurement board within the permissible limit of the *dSPACE* controller and to provide stable output. Since the output voltages are digitally filtered inside the controller, no external filter is needed in this board. As shown in Fig. B.4(b), the width of current paths through the current sensors must be sufficient to allow 30 A of current. The board also consists of interface to the controller where PWM and other control signals are sent. Therefore, a rectangular surface is used for ground to reduce the effect of external noises due to high switching of PWM signals. In addition, to nullify the EMI effect between two crossing traces through upper and lower layer of the board, all crossing traces are drawn perpendicular on each other.

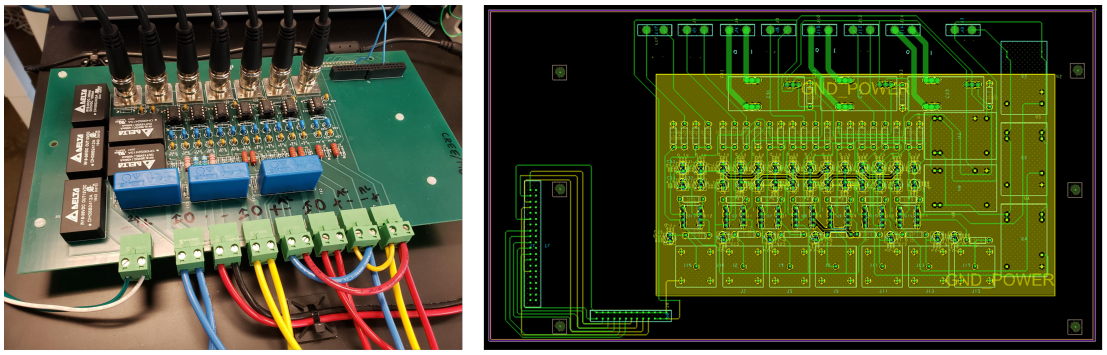

(a) (b)

Figure B.4: *Interface between circuit and the controller; (a) Voltage and current measurement board, and (b) schematic of the measurement board.*

The microgrid consists of three different types of load as shown in Fig. B.5. The load depicted in Fig. B.5(a) is resistive and can be selectively switched from 0.25 kW to 5 kW.

A 0.25 *hp* motor is used as a dynamic active and reactive load, see Fig. B.5(b), which can be continuously varied by using a variable DC supply. The load shown in Fig. B.5(c) is a 5 *kVA* three-phase AC/DC programmable load, which can be programmed to operate in constant current and constant power modes.

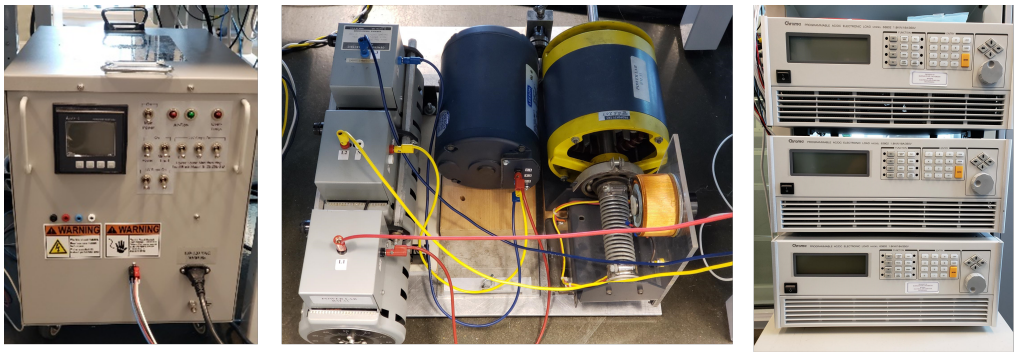

(a) (b) (c)

Figure B.5: *Different types of load in the microgrid testbed; (a) Selectively variable resistive load, (b) continuously variable dynamic load, and (c) programmable AC/DC load.*

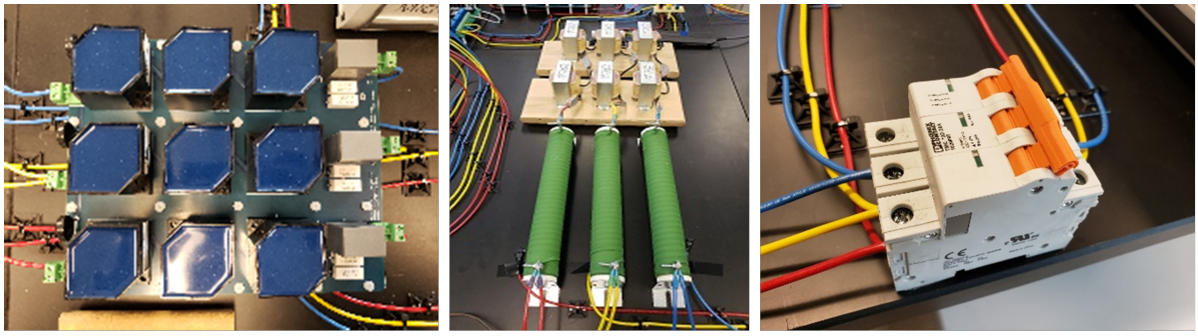

(a) (b) (c)

Figure B.6: *Circuit components of the developed microgrid; (a) LCL filters board, (b) tie-line components, (c) circuit breaker.*

Figs. B.6(a)-(c) show the LCL filter board, the tie-line resistors and inductors, and the circuit breaker, respectively. The LCL filter is used to filter out the fundamental components from the output voltages of the inverters. The filter board is tested for $5 - 20$ *kHz* and can sustain 20 *A* current. Metal Oxide Varistors (MOVs) are connected at each line-line voltage outputs of the inverter to protect the inverters from over voltage. The tie-lines are developed using high-current rated resistors and inductors in series. Finally, 20 *A* circuit breakers are

added to isolate all the inverters and the grid, see Fig. B.1.

Finally, four isolated DC power supplies are used to provide constant DC power to the inverters. In the developed microgrid setup. Three of the DS sources are from *Magna-Power* with $0-600\ V$, $0-6\ A$, and $0-6\ kW$ ratings used for $Inv1$, $Inv3$ and $Inv4$. A *Keysight* $600\ V$, $5.5\ A$, and $3.3\ kW$ DC power supply is used for $Inv2$. For safe operation, it is better to setup the voltage and current limit of each DC power supplies before any experiment. A *WaveRunner* 64Xi-A $600\ MHz$ oscilloscope is used to monitor the waveforms with *Teledyne Lecroy* ADP300 high-voltage differential probe for voltage measurements, and CP030 current prove for current measurements. The oscilloscope can also be used to obtain data at $10\ GB/s$ in four channels. Since all the inverters produces three-phase voltage signals in GFM mode, the phase-sequence of the output voltages must be matched before closing the circuit breakers. This is verified by observing two line-line voltages for each of two inverters in the oscilloscope during the development of the testbed. The phase-sequence, if different, can be easily adjusted from the controller, and therefore no change in the hardware setup is required.